eman ta zabal zazu

Universidad del País Vasco

Euskal Herriko Unibertsitatea

Magnetic-Impurity-Induced Bound States in β-Bi_2Pd

DOCTORAL THESIS by:

Javier Zaldívar Fernández

Thesis Supervisors:

José Ignacio Pacual Chico

Jose Enrique Ortega Conejero

December 17, 2019

Abstract

The antagonistic nature of superconducting and magnetic correlations gives rise to fascinating phenomena in the limit where these two orders can coexist. In the proximity of a magnetic atom, electrons in a superconductor are subject to a competition between Cooper pairing and coupling to the magnetic impurity. The delicate equilibrium between the two interactions induces low-energy excitations known as Yu-Shiba-Rusinov (YSR) states. These new states of matter have gained notoriety during the last decade due to the potential of chains of magnetic atoms on superconductors as candidate building blocks for the experimental realization of topological quantum computation. However, the evolution from single-atom YSR states into the topological state in chains of atoms is still poorly understood.

In this work, we employ Scanning Tunneling Microscopy (STM) and Scanning Tunneling Spectroscopy (STS) to study the properties of YSR states. Using superconducting tips, we investigate the spectroscopic signatures of YSR states from different transition metals in β-Bi_2Pd, a type-II superconductor with an unusual band structure. From the analysis of the energy and spatial distribution of the low-energy excitations, we evaluate the influence of the band structure and magnetic coupling on YSR states.

In the first part, we describe the properties of β-Bi_2Pd and study interband scattering using quasiparticle interference. V adatoms are then deposited on the surface and shown to induce long-ranged YSR excitations. From the combined knowledge of the inter-band scattering processes and the spatial distribution of these states, we identify the band through which V interacts with the superconductor and derive properties of that band. We later use Mn adatoms to construct arrangements of atoms in different configurations and investigate the presence of magnetic coupling and its effect on YSR states. In the last section, we characterize vibrational modes and low-energy excitations in Vanadium hydrides to show how additional mechanisms modify YSR states.

Resumen

El carácter antagónico de las correlaciones superconductoras y magnéticas da lugar a fenómenos fascinantes en el límite en que estos dos órdenes pueden coexistir. En el entorno de un átomo magnético, los electrones de un superconductor están sujetos a una competición entre la formación de pares de Cooper y el acople con la impureza magnética. El delicado equilibrio entre estas dos interacciones induce excitaciones de baja energía conocidas como estados de Yu-Shiba-Rusinov (YSR). Estos nuevos estados de la materia han ganado notoriedad durante la última debido al potencial de las cadenas de átomos en superconductores como candidatas para la realización experimental de la computación cuántica topológica. Sin embargo, la evolución desde los estados YSR en átomos aislados hasta los estados topológicos en las cadenas de átomos todavía no se entiende completamente.

En este trabajo, empleamos el Microscopio de Efecto Túnel (STM, por sus siglas en inglés) y la Espectroscopia de Efecto Túnel (STS) para estudiar las propiedades de los estados YSR. Utilizando puntas superconductoras, investigamos las características de los estados YSR de varios metales de transición en β-Bi_2Pd, un superconductor de tipo II con una estructura de bandas inusual. A través del análisis de la energía y la distribución espacial de las excitaciones de baja energía, evaluamos la influencia de la estructura de bandas y del acople magnético en los estados YSR.

En la primer parte, describimos las propiedades del β-Bi_2Pd y estudiamos el scattering entre bandas usando interferencia de quasipartículas. Después, evaporamos V en la superficie y mostramos que induce excitaciones YSR extendidas. Combinado el conocimiento de los los procesos de scattering entre bandas y la distribución espacial de estos estados, identificamos la banda a través de la cual el V interactúa con el superconductor y derivamos propiedades de esa banda. Después, usamos átomos de Mn para construir estructuras con átomos en distintas configuraciones e investigamos la presencia de acople magnético y su efecto en los estados YSR. En la última sección, caracterizamos los modos vibracionales y las excitaciones de baja energía de Hidruros de Vanadio para mostrar cómo otros mecanismos modifican los estados YSR.

Contents

Introduction

Since the discovery of the Meissner effect by Walther Meissner and Robert Ochsenfeld,[1] the intricate relation between superconducting correlations and magnetic fields has been subject to a continuous investigation. The phenomenological model of superconductivity by the London brothers already accounted for a reorganization of supercurrents in the surface of superconductors in response to external magnetic fields.[2]

The microscopic theory of superconductivity developed by John Bardeen, Leon Cooper, and John Robert Schrieffer in 1957[3] explained how magnetic fields interact with superconductors. In the superconducting state, electrons couple in pairs forming the so-called Cooper pairs. These pairs are composed of electrons with opposite spin, forming a new type of charged particle that can flow without dissipation. Cooper pairs screen a magnetic field, as observed by Meissner and Ochsenfeld. However, the magnetic field tries to align the spins of the electrons in the pair. When the field is large enough, the opposite spins of the electrons that form the Cooper pair align with the magnetic field, breaking the Cooper pair. At this point, magnetism wins over superconductivity, destroying the superconducting state.

In this thesis, we study the atomic-scale equivalent of this process. Instead of using magnetic fields, we employ isolated magnetic atoms. The magnetic field in these atoms tries to align the spin of Cooper pairs around them. However, the microscopic magnetic field perturbs only Cooper pairs within a few nanometers from the atoms. From the delicate equilibrium between the forces that drive the electrons to form Cooper pairs and the microscopic magnetic fields, a new type of quasiparticle emerges: the Yu-Shiba-Rusinov state.

Yu-Shiba-Rusinov (YSR) states were proposed theoretically a few years after the development of BCS theory. Yu Luh, who in 1965 found that "[an] excitation exists around a paramagnetic impurity with its energy level in the energy gap",[4] was the first person to derive the properties of these states. The work was published in a Chinese journal not translated at the time, what hid it from the international scientific community. Three years later, Hiroyuki Shiba generalized a work by Toshio Soda[5] for spin-1/2 magnetic atoms to impurities with any spin.[6] Shiba found great agreement with Soda's calculations and obtained the first analytical expression for the energy at which the bound state appears, still used today. Unaware of the work of Yu and Shiba, A. I. Rusinov derived some years

later an equivalent model.[7] In his work, he not only found the same expression for the energy of the bound states that Yu and Shiba had found years before; he calculated the spatial distribution of the states, showing that these excitations extended away from the impurity site. From the independent works of Yu, Shiba, and Rusinov, a microscopic model for the interaction between a magnetic impurity and a superconductor was established. In acknowledgment of their work, the states that result from this interaction are called Yu-Shiba-Rusinov states.

During the last decade, the advent of quantum computation has motivated many proposals for systems in which these new types of operations can be carried out.[10] Many of those proposals rely on the use of magnetic impurities in chains of superconductors.[11,12] The reason why these platforms are candidates for such systems lies in the peculiar properties of YSR states. As YSR states result from superconducting correlations, they have an intrinsic particle-antiparticle character (more specifically, electron-hole character). When combined with magnetic impurities, the mixture of particle and anti-particle character can reach a maximum, resulting in states with no equivalent in the Standard Model of particles: the Majorana fermions. These fermions have non-conventional properties that could revolutionize the world of quantum computation.[13]

Current research on magnetic impurities in superconductors focuses on understanding which are the conditions required for YSR states to behave as Majorana fermions. With that purpose in mind, recent works have explored the role of magnetic orbitals in the formation of YSR states,[14,15] the detection of magnetic coupling through YSR states,[16,17] or the construction of chains on elemental superconductors.[18,19] However, there is still a long path to walk before we can control all the variables up to the point in which we can construct the proposed topological quantum computer.

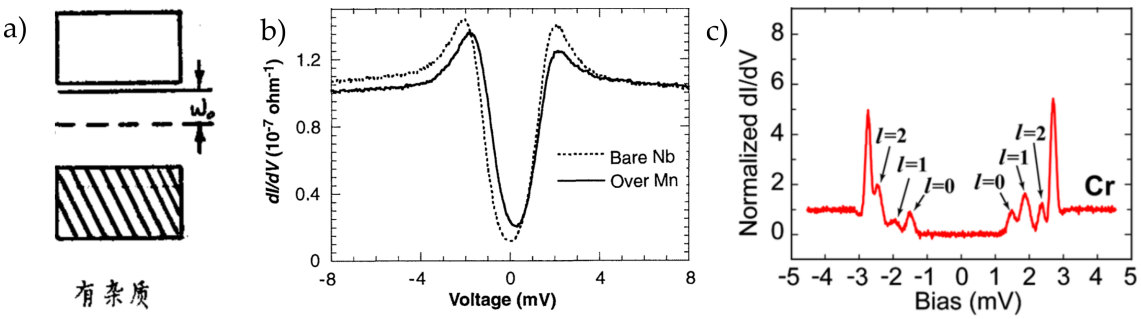

Evolution of YSR states detection. a) Sketch of a YSR state by Yu. Reproduced from [4]. **b)** YSR from a Mn atom on Nb(110) measured at 3.8K using a metallic tip. Reproduced from [8].**c)** Different YSR states from Cr on a Pb film resolved using a superconducting Nb tip at 0.4K. Reproduced from [9].

Outline

The contents of this Thesis are organized as follows:

Chapter 1 introduces BCS theory and examines the properties of YSR states derived from the works of Shiba and Rusinov

Chapter 2 introduces the experimental methods used in this Thesis

Chapter 3 reviews the properties of β-$Bi_2Pd$and describes sample and tip preparation procedures

Chapter 4 examines the spin polarization of bands in β-Bi_2Pd using quasiparticle interference

Chapter 5 reports the formation of extended YSR states in V adatoms on β-$Bi_2Pd$and the relation of these states with the band structure of the superconductor

Chapter 6 analyzes the YSR excitations of structures constructed by lateral manipulation using Mn adatoms

Chapter 7 shows the detection of broken degeneracies in the vibrational modes of Vanadium hydrides using superconducting tips

Chapter One

Theory of Superconductivity and Yu-Shiba-Rusinov States

The theory of superconductivity developed by Bardeen, Cooper and Schrieffer is one of the greatest scientific advancements of the 20^{th} century, describing a macroscopic coherent state in terms of interactions between electrons. Yu-Shiba-Rusinov states probe the atomic-scale interaction of these electrons with magnetic atoms, opening a door into the microscopic details of the superconducting state.

This chapter reviews some of the fundamental concepts of BCS theory and YSR states. Beginning with the formulation of the microscopic theory of superconductivity, the pairing Hamiltonian is informally derived as a motivation for the introduction for the Bogoliubov-Valatin transformation. The resulting quasiparticle eigenstates, the Bogololiubov quasiparticles, are described as the single-particle excitations found in superconductors. Their mixed electron-hole character is reviewed in terms of the coherence factors u_k and v_k. Multi-band superconductivity is briefly introduced afterwards. Combination of the superconducting state with isolated magnetic impurities is shown to lead to the in-gap excitations known as Yu-Shiba-Rusinov states. The spatial distributionof their wavefunction is explicitly derived in the last section as the fundamental analysis tool used in this work.

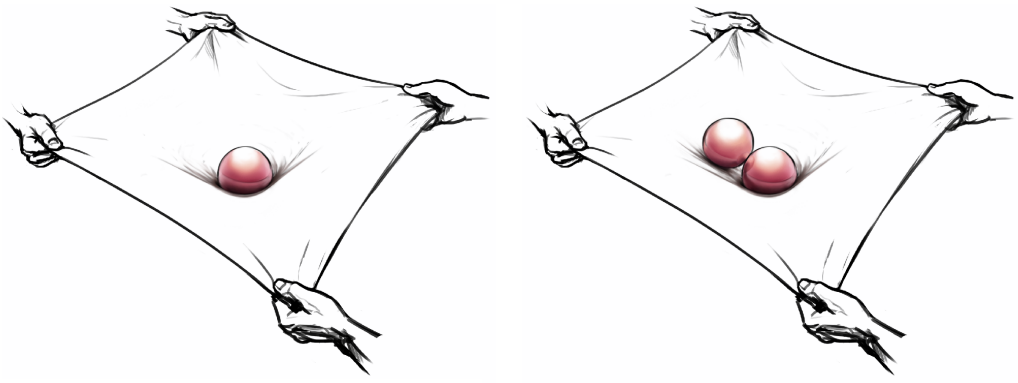

Image by I. Tetin. Reproduced from (XX)

1.1 Microscopic theory of superconductivity

The microscopic theory of superconductivity materialized the combined effort of many scientists in the work by Bardeen Cooper and Schrieffer.[3] This section presents the steps which lead to the mean-field BCS hamiltonian as a motivation for the introduction of Bogoliubov quasiparticles. Rigorous derivations of these equations can be found in [20–26].

BCS THEORY

BCS theory, named after Bardeen, Cooper and Schrieffer, was the first full microscopical despcription of the superconducting state.[3] This theory summarizes all the common phenomena found in superconductors as the result of a coherent state formed by all the electrons close to the energy of the Fermi level. It is based on the idea that electrons close to the Fermi level tend to form so-called Cooper pairs, a bound state of two electrons which forms as the result of an attractive electron-electron interaction.[27] The energy of these correlated pairs is lower than the energy of the individual constituent electrons and so the energy of the system is lowered by their formation.

The mechanisms by which an attractive electron-electron interaction develops can be diverse. For conventional superconductors, this mechanism is the Fröhlich electron-phonon interaction.[28] A descriptive representation of the interaction mechanism is shown in Fig.1.1 a) and b). An electron passing through the lattice attracts positive ions from the crystal lattice and induces a vibration of ions. The movement of the electron is much faster than the lattice vibration, so by the time the lattice is displaced the electron is already long gone. A second electron is attracted by the modified lattice, thus indirectly interacting with the first electron. The interaction is modeled as the phonon-mediated momentum exchange between electrons shown in the Feynman diagram in Fig.1.1 c).

In BCS theory, the attractive phonon-mediated momentum exchange is assumed to be constant in an energy range defined by the Debye frequency ω_D as a measure of ion relaxation time. The associated potential includes shielded Coulomb interactions and is defined as:

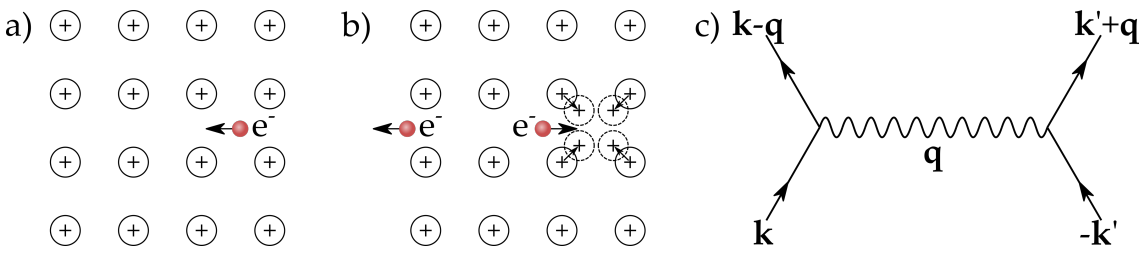

Figure 1.1: Electron-phonon interaction. a) Positive ions are attracted by an electron in their viccinity. **b)** By the time the lattice has displaced the electron is long gone, but a second electron is attracted by the excess positive charge. **c)** Feynman diagram of the phonon-exchange-mediated electron-electron interaction.

$$V_{\mathbf{k},\mathbf{k}'} = \begin{cases} -V_0 & \text{if } |\xi_{\mathbf{k}}| < \hbar\omega_D \text{ and } |\xi_{\mathbf{k}'}| < \hbar\omega_D \\ 0 & \text{otherwise.} \end{cases}$$

where $\xi_{\mathbf{k}} = \epsilon_{\mathbf{k}} - \epsilon_F$ is the electron energy relative to the Fermi level ϵ_F

Pairs of electrons within an energy range $\epsilon_F \pm \hbar\omega_D$ will preferably go into the correlated state than submerge into the Fermi sea as free electrons. An instability of the Fermi surface follows from this condition, as the Fermi sea is emptied from electrons that go into these pairs, lowering the energy of the system. As a consequence, the Fermi surface does not exist for superconductors. As the number of correlated pairs increases, they begin to interfere with each other. At this point, the pairs cannot be treated independently and the ground state becomes a many-body problem.

The many-body ground state of a a superconductor is constructed by adding superpositions of Cooper pairs. For conventional superconductors, these pairs have opposite momentum and spin and thus the ground state is:

$$|\Psi_{BCS}\rangle = \prod_{\mathbf{k}} (u_{\mathbf{k}} + v_{\mathbf{k}} c^{\dagger}_{\mathbf{k}\uparrow} c^{\dagger}_{\text{-}\mathbf{k}\downarrow})|0\rangle \tag{1.1}$$

where $c^{\dagger}_{\mathbf{k}\sigma}$ is the creation operator for an electron with momentum **k** and a spin σ and $|0\rangle$ is the vacuum state. $|v_{\mathbf{k}}|^2$ gives the average occupation of a pair with momentum (**k**,-**k**) and spin (↑,↓) and $|u_{\mathbf{k}}|^2$ the average non-occupation of the pair. The coefficients are subject to the normalization condition $|v_{\mathbf{k}}|^2 + |u_{\mathbf{k}}|^2 = 1$.

The superposition condition is imposed by the coherence factors $u_{\mathbf{k}}$ and $v_{\mathbf{k}}$ being non-zero and results in a mixture of states with an ill-defined number of particles. The opposite momentum and spin condition is imposed by $c^{\dagger}_{\mathbf{k},\uparrow} c^{\dagger}_{\text{-}\mathbf{k},\downarrow}$. A superconductor with non-zero total momentum can also be constructed by relaxing the ($\mathbf{k}_1$,$\mathbf{k}_2$) = (**k**,-**k**) condition, but the binding energy of the pair would be then reduced by a factor ($\mathbf{k}_1$+$\mathbf{k}_2$)^2, thus increasing the energy of the ground state.[26]

Pairing Hamiltonian

The pairing Hamiltonian of a conventional superconductor only includes the electron-electron interaction described in the previous section. This interaction appears as a scattering term subject to the potential $V_{\mathbf{k},\mathbf{k}'}$ and takes a pair of electrons with momentum (**k'**,-**k'**) into (**k**,-**k**):

$$\mathcal{H} = \sum_{\mathbf{k},\sigma} \xi_{\mathbf{k}} c^{\dagger}_{\mathbf{k}\sigma} c_{\mathbf{k}\sigma} + \frac{1}{N} \sum_{\mathbf{k},\mathbf{k}'} V_{\mathbf{k},\mathbf{k}'} c^{\dagger}_{\mathbf{k}\uparrow} c^{\dagger}_{\text{-}\mathbf{k}\downarrow} c_{\text{-}\mathbf{k}'\downarrow} c_{\mathbf{k}'\uparrow} \tag{1.2}$$

where N is the number of electrons in the system and $V_{\mathbf{k},\mathbf{k}'}$ is the interaction potential. Spin rotation invariance is imposed by making $V_{\mathbf{k},\mathbf{k}'} = V_{\text{-}\mathbf{k},\mathbf{k}'} = V_{\mathbf{k},\text{-}\mathbf{k}'}$ and singlet pairing is imposed by $c^{\dagger}_{\mathbf{k}\uparrow} c^{\dagger}_{\text{-}\mathbf{k}\downarrow} c_{\text{-}\mathbf{k}'\downarrow} c_{\mathbf{k}'\uparrow}$.

BCS theory uses a mean-field approximation to convert the Hamiltonian into:

$$\mathcal{H}^{MF} = \sum_{\mathbf{k},\sigma} \xi_{\mathbf{k}} c^{\dagger}_{\mathbf{k}\sigma} c_{\mathbf{k}\sigma} - \sum_{\mathbf{k}} \Delta^{*}_{\mathbf{k}} c_{\text{-}\mathbf{k}\downarrow} c_{\mathbf{k}\uparrow} - \sum_{\mathbf{k}} \Delta_{\mathbf{k}} c^{\dagger}_{\mathbf{k}\uparrow} c^{\dagger}_{\text{-}\mathbf{k}\downarrow} + const. \tag{1.3}$$

where the energy gap of the superconductor is given by the non-zero vacuum expectation value of Cooper pair creation and annihilation operators:

$$\Delta_{\mathbf{k}} \equiv -\frac{1}{N} \sum_{\mathbf{k'}} V_{\mathbf{k},\mathbf{k'}} \langle c_{-\mathbf{k'}\downarrow} c_{\mathbf{k'}\uparrow} \rangle \qquad \Delta^{*}_{\mathbf{k}} \equiv -\frac{1}{N} \sum_{\mathbf{k'}} V_{\mathbf{k},\mathbf{k'}} \langle c^{\dagger}_{\mathbf{k'}\uparrow} c^{\dagger}_{-\mathbf{k'}\downarrow} \rangle \tag{1.4}$$

The characteristic length scale of Cooper pairs follows from the ratio between the Fermi velocity of paired electrons v_F and the superconducting gap as a measure of the coherence length of the correlated pairs[1]:

$$\xi = \frac{\hbar v_F}{\pi \Delta} \tag{1.5}$$

Diagonalization of the mean-field Hamiltonian is not a straight-forward process due to the presence of bilinear $c_{\text{-}\mathbf{k},\downarrow} c_{\mathbf{k},\uparrow}$ and $c^{\dagger}_{\mathbf{k},\uparrow} c^{\dagger}_{\text{-}\mathbf{k},\downarrow}$ terms. It can be accomplished by means of the Bogoliubov-Valatin transformation[29,30]:

$$c_{\mathbf{k},\uparrow} = u_{\mathbf{k}} a_{\mathbf{k}\uparrow} + v_{\mathbf{k}} a^{\dagger}_{\text{-}\mathbf{k}\downarrow} \qquad c^{\dagger}_{\text{-}\mathbf{k},\downarrow} = -v^{*}_{\mathbf{k}} a_{\mathbf{k}\uparrow} + u^{*}_{\mathbf{k}} a^{\dagger}_{\text{-}\mathbf{k}\downarrow} \tag{1.6}$$

Cross-diagonal terms in the pairing Hamiltonian will be canceled if the coefficients $u_{\mathbf{k}}$ and $v_{\mathbf{k}}$ are such that:

$$|u_{\mathbf{k}}|^2 = \frac{1}{2}\left(1 + \frac{\xi_{\mathbf{k}}}{\sqrt{\xi^2_{\mathbf{k}} + |\Delta_{\mathbf{k}}|^2}}\right) \tag{1.7}$$

$$|v_{\mathbf{k}}|^2 = \frac{1}{2}\left(1 - \frac{\xi_{\mathbf{k}}}{\sqrt{\xi^2_{\mathbf{k}} + |\Delta_{\mathbf{k}}|^2}}\right)$$

The mean field Hamiltonian can then be rewritten in a simpler form using the operators defined by the Bogoliubov-Valatin transformation:

$$\mathcal{H} = E_0 + \sum_{\mathbf{k},\sigma} E_{\mathbf{k}} a^{\dagger}_{\mathbf{k}\sigma} a_{\mathbf{k}\sigma} \tag{1.8}$$

[1] From this point on, Δ, $u_{\mathbf{k}}$ and $v_{\mathbf{k}}$ are considered real without loss of generality.

where E_0 is the energy of the ground state and $E_{\mathbf{k}}$ is the dispersion relation of the eigenstates defined by the Bogoliubov-Valatin transformation. The second term gives the increase in energy above the ground state in terms of the operators $a_{\mathbf{k},\uparrow}\, a^{\dagger}_{\text{-}\mathbf{k},\downarrow}$. As a result, the eigenstates defined by these operators describe the excitations of the superconductor, the Bogoliubov quasiparticles.

BOGOLIUBOV QUASIPARTICLES

In the previous section, the pairing hamiltonian was diagonalized by means of the Bogoliubov-Valatin transformation. This transformation defines the excitations in a superconductor by means of a new set of eigenstates called Bogoliubov quasiparticles. The general expression for the creation of a Bogoliubov quasiparticle with momentum $\mathbf{k}$ and spin σ is given by:

$$a^{\dagger}_{\mathbf{k},\sigma} = c^{\dagger}_{\mathbf{k}\sigma} u_{\mathbf{k}} + sgn(\sigma) c_{\text{-}\mathbf{k}-\sigma} v_{\mathbf{k}} \tag{1.9}$$

Bogoliubov excitations coherently combine creation and annihilation of electrons with opposite spin, weighted by the coherence factors $u_{\mathbf{k}}$ and $v_{\mathbf{k}}$. Physically, this situation corresponds to mixing electron and hole bands into a new fermionic eigenstate following the dispersion relation:

$$\pm\, E_{\mathbf{k}} = \pm\sqrt{\xi^2_{\mathbf{k}} + |\Delta_{\mathbf{k}}|^2} \tag{1.10}$$

The dispersion relation $E_{\mathbf{k}}$ is plotted in Fig.1.2 a). The superconducting gap Δ marks the minimum excitation of Bogoliubov quasiparticles. For states around the superconducting gap, electron and hole bands are mixed and thus the electron or hole character of the excitation will be given by the energy-dependent amplitude of the coherence factors (Eq.1.7), depicted in Fig.1.2 b).

Besides being a base transformation, the Bogoliubov transformation emphasizes the electron-hole symmetry present in superconductors. For a given energy within the particle-hole mixing range, there are two different eigenstates corresponding to the creation of an electron and a hole. This is a consequence of electron-hole symmetry in superconductors. Behind this symmetry lies the fundamental transport characteristic of superconductors: Andreev reflection of an electron into a hole and viceversa.[31]

The density of states of Bogoliubov quasiparticles can be calculated from their dispersion relation. Fig.1.2 c) shows the excitation spectrum of a superconductor as calculated by:

$$\rho(E) = \frac{1}{N} \sum_{\mathbf{k}} \left[|u_{\mathbf{k}}|^2 \delta(E - E_{\mathbf{k}}) + |v_{\mathbf{k}}|^2 \delta(E + E_{\mathbf{k}}) \right] \tag{1.11}$$

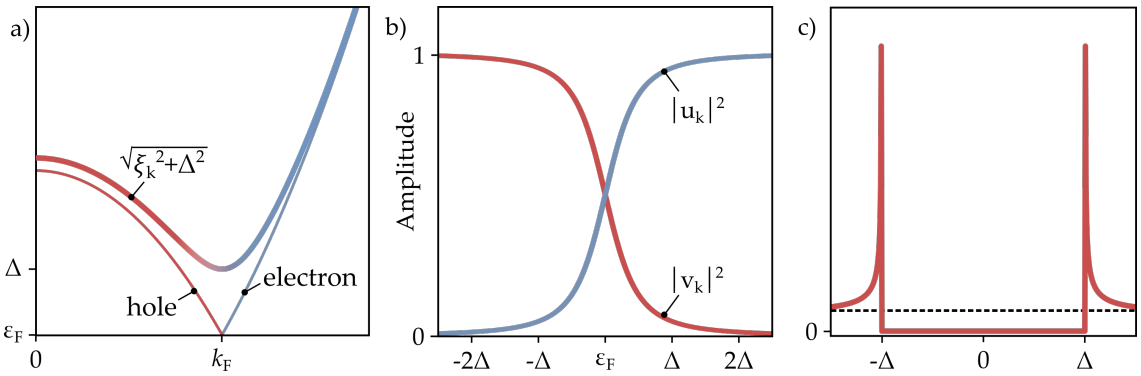

Figure 1.2: Bogoliubov quasiparticles. a) Dispersion relation of Bogoliubov quasiparticles. **b)** Amplitude of the coherence factors around the Fermi level. **c)** Density of states in a superconductor, showing the absence of states for excitation energies below the superconducting gap. The density of states in the normal states is marked by a dashed line.

1.2 Multi-band Superconductivity

From the perspective of the single-band singlet s-wave superconductor shown before, electrons with opposite spin and momentum bound together in order to from Cooper pairs. However, in systems where several bands cross the Fermi level this picture acquires an additional level of complexity, as different bands may become superconducting at different temperatures with different superconducting gaps and electrons may scatter between them.

The first take on the problem studied the case of two overlapping bands α and β in which both intra- and inter-band scattering of electrons are allowed. The two-band model developed by Suhl *et al.*[32] was based on the BCS formalism and contained two intra-band pairing terms corresponding to pairing in the form:

$$\sum_{\mathbf{kk'}} V_{ii} c^\dagger_{i,\mathbf{k}\uparrow} c^\dagger_{i,-\mathbf{k}\downarrow} c_{i,-\mathbf{k'}\downarrow} c_{i,\mathbf{k'}\uparrow} \tag{1.12}$$

In order to account for the intra-band processes, he also included two additional terms:

$$\sum_{\mathbf{kk'}} V_{ij} c^\dagger_{i,\mathbf{k}\uparrow} c^\dagger_{i,-\mathbf{k}\downarrow} c_{j,-\mathbf{k'}\downarrow} c_{j,\mathbf{k'}\uparrow} \tag{1.13}$$

where i, j represents the band index and V_{ij} is the averaged interaction energy resulting from phonon emission and adsorption by i-j processes minus the corresponding shielded Coulomb interaction. Under this framework, an electron from band α or β may emit a phonon which would then be reabsorbed by an electron from the same band ($V_{\alpha\alpha}$ or $V_{\beta\beta}$) or from the other band ($V_{\alpha\beta}$).

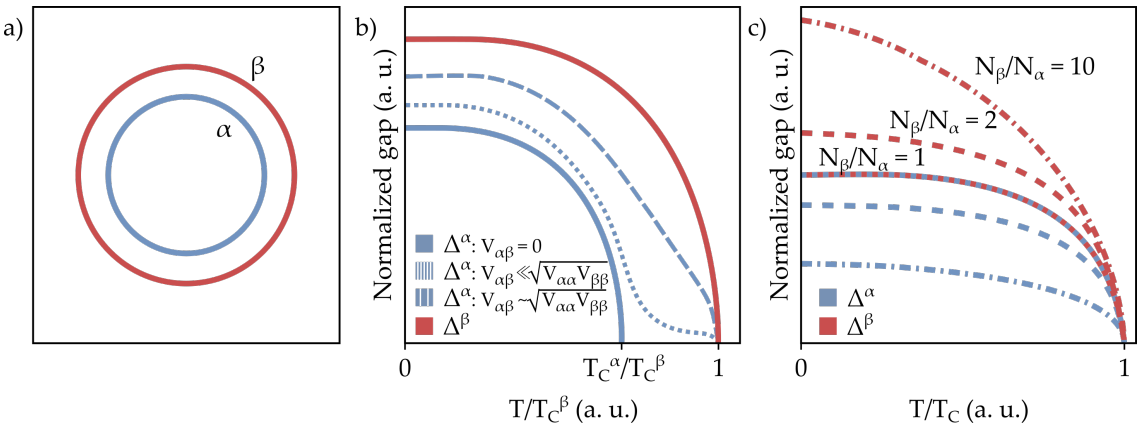

Figure 1.3: Gap evolution in a two-band superconductor. a) Fermi surface showing two bands α and β at the Fermi level. b) Temperature dependence of the normalized gap in the presence of intra-band scattering for different inter-band scattering strenghts $V_{\alpha\beta}$. c) Influence of the density of states of each band on the amplitude of the superconducting gap for the case of purely inter-band scattering ($V_{\alpha\alpha} = V_{\beta\beta} = 0$). b) and c) Adapted from [33].

Depending on the values of V_{ij}, the system evolves into different situations. Starting with a system in which both α and β bands become superconducting, for the case of pure intra-band scatering ($V_{\alpha\beta} = 0$), the gaps will be completely independent as depicted in Fig.1.3 b) with solid lines. Both superconducting gaps show a standard BCS temperature dependence and each band has a critical tempertature.

As inter-band scattering is turned on, the band with the highest T_C (β) raises the critical temperature of the other one α (see dashed lines). Δ_α develops a tail which closes at the critical temperature of Δ_β, thus resulting in a single superconducting transition temperature. As the inter-band scattering strength increases, the tail disappears and the behavior of Δ_α approaches that of Δ_β.

For the case of purely inter-band scattering ($V_{\alpha\alpha} = V_{\beta\beta} = 0$), both Δ_α and Δ_β will display BCS curves with the same critical temperature. However, the amplitude of the gaps will differ depending on the density of states N_i of each band. Fig.1.3 c) shows the influence of the ratio between N_α and N_β on the relative amplitudes of the gaps. According to this model, only for the case in which $N_\alpha = N_\beta$ the system will display a single gap.

Besides providing the mechanism for multi-gap superconductors to display a single transition temperature, single-quasiparticle inter-band scattering results in the formation of Cooper pairs from different bands,[34] what may give rise non-zero-momentum Cooper pairs. In the case of a strong-enough interaction, it also provides the mechanism for a superconducting band to proximitize a metallic band.[33]

1.3 Magnetic Impurities in Superconductors

Experiments performed on different superconductors containing magnetic and non-magnetic impurities show the two kinds of dopants act differently on the superconducting state.[35,36] Non-magnetic impurities have very little effect on superconductivity in a broad doping density range and were considered from a theoretical point of view in Anderson's model of dirty superconductors.[37] Magnetic impurities, on the other side, break time-reversal symmetry and strongly modify the superconducting state.

YU-SHIBA-RUSINOV SSTATES

From a microscopic point of view, paramagnetic impurities act as magnetic scattering centers for Bogoliubov quasiparticles. The interaction is represented by an *s-d* interaction term:[4,6,7]

$$\mathcal{H}_{s-d} = -\frac{J}{2N}\sum_{\mathbf{k},\mathbf{k}'} c^{\dagger}_{\mathbf{k}}\boldsymbol{\sigma} c_{\mathbf{k}}\mathbf{S} \tag{1.14}$$

subject to the conditions $J \to 0$, $S \to \infty$ and $JS = finite$ that describe a classical spin. J is the exchange integral term, $\boldsymbol{\sigma}$ is a Pauli spin operator and $\mathbf{S}$ is a classical vector representing the spin of the impurity.

Solutions of the Hamiltonian for purely magnetic scattering from a spin oriented along the z axis yield a state at energy:

$$\epsilon_0 = \Delta\frac{1-(JS\pi N_0/2)^2}{1+(JS\pi N_0/2)^2} \tag{1.15}$$

where N_0 is the DOS in the normal state.

Paramagnetic impurities thus create a state inside the superconducting gap known as Yu-Shiba-Rusinov (YSR) state, as depicted in Fig.1.4 a). Phenomenologically, the state can be understood as the result of the polarization of electrons in Cooper pairs by the impurity.[7] This interaction diminishes the binding energy of the pair, creating a bound state that can be excited with an energy $<\Delta$. The eigenstate of the system is a Bogoliubov quasiparticle with $\epsilon_0<\Delta$ that, due to the mixed electron-hole character of these excitations, appears as a pair of peaks at symmetric energies inside the superconducting gap, as shown in Fig.1.4 b). The spin-orientation of the YSR state is parallel to the impurity spin and, following Eq.1.9, will be opposite for its electron and hole components.

The energy of the YSR state will strongly depend on the exchange integral J. Increasing J the energy of the bound state is lowered as shown in Fig.1.4 c). For a given S there exists a critical J value J_C above which the binding energy of the YSR state is higher than the binding energy of Cooper pairs and the ground state

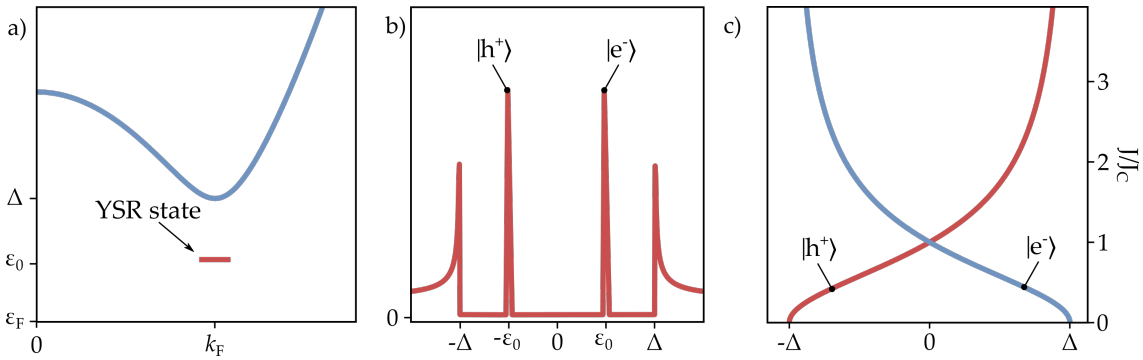

Figure 1.4: Yu-Shiba-Rusinov states. a) YSR states as a bound state in the Bogoliubov dispersion. **b)** Spectroscopic signature of YSR states showing energy-symmetric electron-like ($|e^-\rangle$) and hole-like ($|h^+\rangle$) components. **c)** Energy of $|e^-\rangle$ and $|h^+\rangle$ as a function of JS. Above a critical value, the character of the components is inverted.

of the system is no longer $|\Psi_{BCS}\rangle$ but the formerly excited state of the system, resulting in a quantum phase transition.

YSR Wavefunction

The previous section described the formation of a bound state in a superconductor by the presence of a clasical spin. Following Rusinov and Yu, the problem can be solved by means of a Bogoliubov transformation to obtain the spatial dependence of the excited state electron and hole components. In this picture, the impurity acts as a combined spin-indpendent electrostatic potential U and a spin-dependent magnetic potential JS, both of them δ-like, described by:

$$V(r) = \frac{2\pi}{m}\left(U(r) + J(r)\sigma S\right) \tag{1.16}$$

Solutions for that potential are obtained Fourier-transforming the eigenstates of the Bogoliubov-de-Gennes hamiltonian and expanding $u_{\mathbf{k}}$, $v_{\mathbf{k}}$ and the impurity potential in spherical harmonics[balatsky_impurity_2006]. The energy of the l-th harmonic of the YSR state is then given by:

$$\epsilon_l = \Delta \frac{1 + k_F^2\left[U_l^2 - (J_l S)^2\right]}{\sqrt{\left[1 + k_F^2\left(U_l^2 - (J_l S)^2\right)\right]^2 + 4k_F^2\left(J_l S\right)}} \tag{1.17}$$

where k_F is the Fermi wavevector, and U_l and J_l represent the l-th harmonic of the delta-like potentials. A scattering phase $\delta^{\pm}$ for the electron-like (+) and hole-like (-) components can be defined from the values of the potentials as:

$$U_l \pm J_l S = tan(\delta_l^{\pm}) \tag{1.18}$$

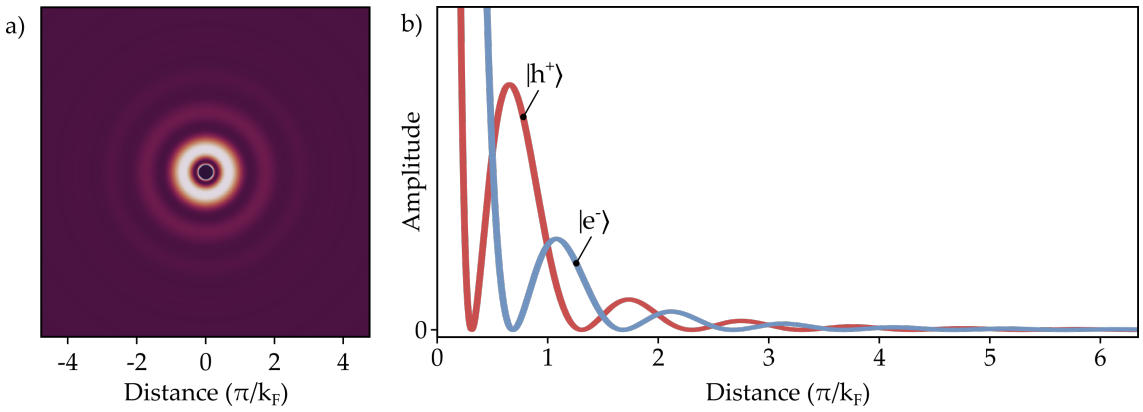

Figure 1.5: Wave function of YSR states. Simulated spatial distribution of the electron and hole components for JS=1.5 and $Delta = 1$. **a)** Radial distribution of $u(r)^2_{\mathbf{k}}$. **b)** Lateral profiles showing the decay of $u(r)^2_{\mathbf{k}}$ and $v(r)^2_{\mathbf{k}}$.

Equation1.17 describes a discrete set of bound states, but restricting scattering to the isotropic case (l=0) yields a single bound state with $u(r)_{\mathbf{k}}$ and $v(r)_{\mathbf{k}}$ away from the impurity given by:

$$u(r)_{\mathbf{k}} = \frac{sin(k_F r - \delta_0^+)}{k_F r} e^{-r/\xi |sin(\delta_0^+ - \delta_0^-)|} \tag{1.19}$$
$$v(r)_{\mathbf{k}} = \frac{sin(k_F r - \delta_0^-)}{k_F r} e^{-r/\xi |sin(\delta_0^+ - \delta_0^-)|}$$

The square of $u_{\mathbf{k}}$ and $v_{\mathbf{k}}$ will show an oscillating behavior decaying as $1/r^2$ that represents the modulated amplitude of the electron and hole components as shown in Fig.1.5. The dephasing between the two components is given by the $\delta^{\pm}$ and will thus be exchange-coupling dependent for purely magnetic scattering.

In the absence of superconducting correlations, Eqs.1.19 describe a free-electron in a centrally-symmetric field[7]. In the superconducting state, Bogoliubov quasiparticles play the role of the free-electron and manifest the effects of the interaction in their electron and hole components. Both $u_{\mathbf{k}}$ and $v_{\mathbf{k}}$ are experimentally-measurable quantities in YSR states, and thus from the analysis of their energies, periods of oscillation and phase shifts, information about the magnetic impurity and the superconducting host can be obtained[38–40].

Chapter Two

Experimental Techniques

Scanning Tunneling Microscopy was the first technique to allow for the direct visualization of individual atoms. Developed by Gerd Binnig and Heinrich Roher, STM is a member of the family of Scanning Probe techniques that relies on electron tunneling between a metallic tip and sample to measure topographic changes in the order of few picometers on the surface of a sample. Moreover, STM also provides access to the local density of states (LDOS) of a sample and thus the atomic-scale electronic structure of materials.

This chapter reviews the basic principles of STM imaging and STM high-resolution spectroscopy using superconducting tips. The main modes of operation used in this work are then lsited, with a brief introduction to lateral manipulation. The experimental setup is described in the last section of this chapter.

2.1 Scanning Tunneling Microscope

This section reviews the basic principles of operation of an STM. Extensive descriptions can be found in literature.[41,42] On its most basic version, an STM consists on a metallic tip and a sample whose position can be controlled with pm precision by means of piezoelectric actuators. The tip and the sample are brought into proximity to each other while subject to a potential drop, the bias voltage. For tip-sample distances in the order of 1 nm, electrons can tunnel through the vacuum barrier between tip and sample with a probability proportional to the exponential of the distance between the tip and the sample. The current generated by these electrons is used as a measure of the distance between the tip and the sample. A PI controller is used to control the piezoelectric actuator that positions the tip and keep it at a constant distance from the sample by setting a setpoint current. Slowly moving the tip in X and Y by means of additional piezoelectric actuators, surface topography can be recorded by tracking the tip position. A schematic representation of the process is shown in Fig.2.1.

Z-resolution in the pm-range is achieved thanks to the exponential distance-dependence of the tunneling current. At typical working bias voltages, increasing the distance between the tip and the sample by 0.1 nm (approximately the height of an atom) results in a decrease in the tunneling current by a factor ∼10. This implies that most of the contribution to the tunneling current comes from the very end of the tip apex. If the tip is terminated by a single atom, lateral resolution will only be limited by the lateral dimensions of that atom.

The current of tunneling electrons flowing between the tip and the sample results from the elastic transmission of electrons in filled states on one side to empty states in the other. The tunneling current is hence the result of the combined LDOS of the tip and the sample. The total tunneling current for an applied bias voltage V_{bias} will result from the contribution of all the energies in the range

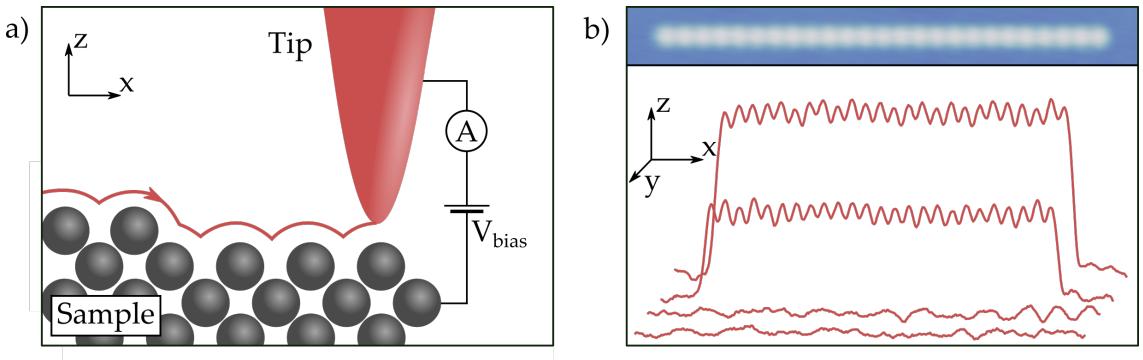

Figure 2.1: Topography acquisition in STM. a) The distance between tip and sample is kept constant while the tip is displaced. An ammeter measures the tunneling current caused by the potential drop (V_{bias}) between the tip and the sample. **b)** The procedure is repeated over several lines along a scan area (top) and the profiles (bottom) are used to generate a 2D map.

between the Fermi energy ϵ_F and ϵ_F+eV_{bias}, as shown in Fig.2.2 a). This can be expressed as an integral:

$$I_{tunnel}(V) \propto \int_{\epsilon_F}^{\epsilon_F+eV} dE\rho_t(E-eV)\rho_s(E)\left[f_t(E-eV)-f_s(E)\right]|M|^2 \tag{2.1}$$

where $|M|$ is the tunneling matrix element (assumed to be constant around ϵ_F), ρ_s and ρ_t are the DOS of the sample and the tip, respectively, and f is the Fermi-Dirac distribution.

Spectroscopy using Superconducting Tips

The Fermi-Dirac distribution of electron energies around the Fermi level is responsible for finite-temperature broadening of electronic features around the Fermi level and limits the energetic resolution in STM. It can be circumvented using superconducting tips on superconducting samples (Fig.2.2 b). In this case,

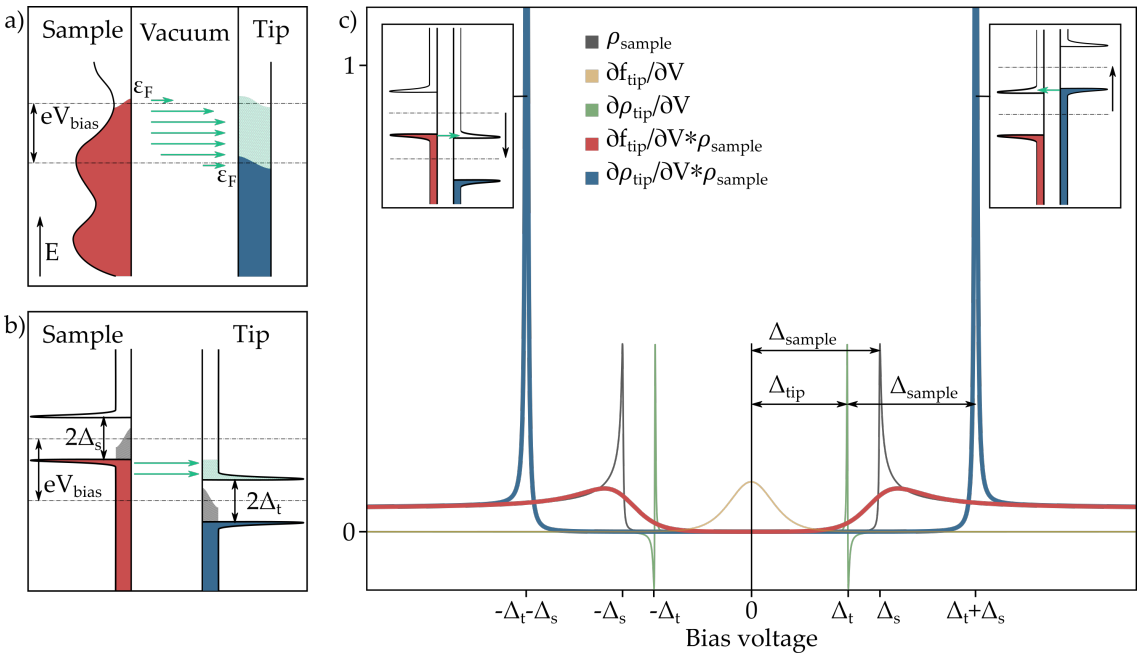

Figure 2.2: Metallic and superconducting tips. a) Elastic tunneling of electrons between two metals at finite temperature. Electrons in occupied states within the range defined by eV_{bias} can tunnel into empty states on the other side, indicated by a green area. Spectroscopic features are broadened by the thermal distribution of electrons around ϵ_F. **b)** Elastic tunneling between two superconductors. The superconducting gap is larger than the thermal distribution of energies(represented by gray areas around ϵ_F), preventing thermal broadening. Spectroscopic features are shifted by Δ_{tip}, the energy difference between ϵ_F and the first available states. **c)** Numerical convolution of a $50\mu eV$-broadened superconductor DOS (grey) with the derivative of the Fermi-Dirac distribution at 1.3K (red) and the derivative of a superconducting tip subject to a $50\mu eV$ broadening. For clarity, the derivatives are shown in the image (yellow:Fermi-Dirac at 1.3K, green:superconducting tip. Y-axis magnified in both cases.).

the density of states is gapped and the first available states appear at an energy Δ_{tip}+Δ_{sample} from ϵ_F. Provided the superconducting gap is bigger than the width of the Fermi-Dirac distribution of energies, the energy of these states is not thermally-broadened and Eq.2.2 can be approximated assuming the Fermi-Dirac distribution is a step function:

$$I_{tunnel}(V) \propto \int_{\epsilon_F}^{\epsilon_F+eV} dE\rho_t(E-eV)\rho_s(E) \tag{2.2}$$

The previous equation represents a mathematical convolution between the density of states of the the sample and the tip. Its derivative with respect to the bias voltage will be:

$$\frac{dI_{tunnel}(V)}{dV} \propto \int_{\epsilon_F}^{\epsilon_F+eV} dE\frac{\partial\rho_t(E-eV)}{\partial V}\rho_s(E) \tag{2.3}$$

The dI/dV signal using superconductings tip will thus not directly reflect the LDOS of the sample ρ_s , but a convolution with the derivative of the DOS of the tip ρ_t. The main features found in this derivative are associated to the δ-like shape of the coherence peaks and hence they just introduce an energy shift and a small broadening associated to finite-lifetime effects. Fig.2.2 c) shows a comparison of the lifetime-broadened-DOS of a superconductor and the corresponding dI/dV signal using a metallic tip and a superconducting tip at 1.3K. Using a metallic tip, the energy resolution of the measurement is limited by the width of the derivative of the Fermi-Dirac function at the working temperature. Using a superconducting tip, resolution is limited by the width of the derivative of ρ_t. As the DOS of the tip is approximately a δ function, its derivative is much less wide than the equivalent thermal broadening.

Inelastic Electron Tunneling Spectroscopy

Conventional tunneling in STM is an elastic process in which electrons from the tip populate empty states in the sample. However, inelastic processes can also contribute to the tunneling current. When the tip is used to probe atoms or molecules with discrete energy levels, electrons can excite the system into a hgher-energy state, losing the corrsponding energy in the excitation. This process is known as inelastic tunneling and has been used to probe vibrational modes of molecules and to promote magnetic systems to excited states.[43–45]

The signature of inelastic tunneling is an increase in the tunneling current above the energy of the excited state. The spectroscopy curve of an inelastic excitation is displayed in Fig**??**. The increased current is caused by the opening of an additional tunneling channel in which the electrons lose some energy to excite the mode and then probe the density of states at eV-E_{exc}.

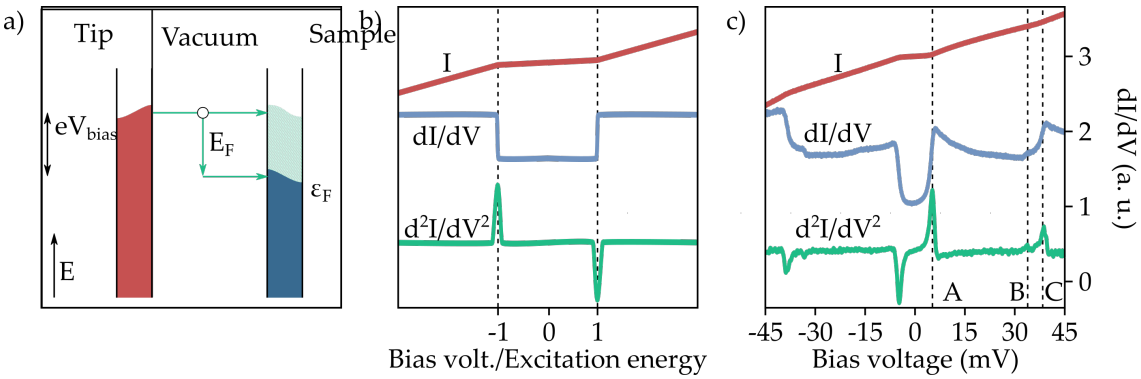

Figure 2.3: Inelastic excitation of vibrational modes and spin excitations. a) Schematic representation of the inelastic conduction channel. An electron loses an energy E_{exc} to excite a mode in the atom/molecule. **b)** Signatures of an inelastic excitation in the tunneling current, its first derivatiive and its second derivative. **c)** Spectroscopy of a nickelocene molecule on top of a Ni atom showing a spin excitation (A), a vibrational mode (B), and a vibration-assisted spin excitation.

2.2 Modes of operation

This section describes the main techniques used for data acquisition in this work: bias spectroscopy, dI/dV mapping and spectroscopy grids

Bias Spectroscopy

Experimental acquisition of dI/dV spectra is performed by sweeping bias voltage while the tip is held at a fixed distance from the surface. ϵ_F is fixed at V_{bias}=0. Different bias voltages yield a I_{tunnel} given by Eq.2.2, from which dI/dV is calculated by means of an AC modulation V_{RMS} added to V_{bias} and a lock-in amplifier.

dI/dV mapping

The spatial distribution of spectroscopic features can be measured by simultaneously recording the dI/dV signal while the area is scanned in topographic imaging mode. V_{bias} should be chosen to match the energy of the desired spectroscopic feature and a suitable lock-in modulation should be added to the DC signal. In gapped systems no tunneling current flows between the tip and the sample for energies inside the gap and thus this procedure is not suitable for mapping the spatial distribution of in-gap states. Additionally, as the tunneling current integrates the LDOS of the sample between ϵ_F and V_{bias}, spectroscopic features at low bias may result in unrealistic topographies that combine topography and spectroscopic features.

For those cases in which in-gap states or low-bias features want to be mapped, an additional acquisition method is used: dual-pass scan. In this mode of operation the surface is first scanned at a V_{bias} at which topography can be properly measured. The current feedback is then stopped and V_{bias} changed to the desired

value. The tip is forced to repeat the same trajectory it followed during the first scan, while dI/dV at the new V_{bias} is recorded. The procedure is done line-by-line in order to prevent drifting.

SPECTROSCOPIC GRIDS

For systems in which spectroscopic features appear at different energies, the spatial distribution of those features is more effectively acquired measuring a bias spectrum at each point of the scanned area. The generated 3D dataset contains dI/dV maps at each one of the energies of the spectra. As a spectrum is measured at each pixel, the acquisition time per map point is typically more than ten times longer than for dI/dV maps, and hence spatial resolution needs to be reduced in order to avoid drifting during the acquisition time.

2.3 Atomic Manipulation

One of the initial motivations behind this works was the possibility of constructing custom nanostructures on superconductors in order to probe Majorana physics. The mechanism by which atoms can be manipulated on a surface depends on many factors such as the tip apex composition or the adsorption state of the atom. It also requires a precise control of tip positioning, for which purpose an atom manipulation software was developed at the beginning of this project.

Manipulation of atoms can be performed using different mechanisms. The one used in this work is referred to as lateral manipulation and was first used by Eigler and Schweizer to write 'IBM' using Xenon atoms on Ni(110).[46] This mechanism relies on tip-atom interaction in order to push or attract the atom to its new position and is strongly dependent on the chemical composition of the tip apex.

During lateral manipulation, the tip approaches the atom from its side. As the tip gets closer to the atom, repulsive/attractive interactions result in the atom being displaced away/closer to the tip apex. Depending on whether the atom is attracted to the tip or repelled, the displacement will be deemed pulling or pushing, respectively. This procedure can be done while keeping the feedback open (constant height mode) or with a constant current setpoint (constant current mode). An schematic representation of a constant-current pulling manipulation is depicted in Fig.2.4 a). The tip approaches the atom from the left, passes above it and once the tip reaches a certain position, the atom jumps towards it into the next available adsorption site. The procedure is later repeated as many times as required until the atom is placed in its final location.

In constant-current mode, the distance between the tip and the sample is controlled by means of the applied bias voltage and the setpoint current, what allows us to define it in terms of the junction resistance. The value of the junction resistance plays an important role in the manipulation procedure. Depending on

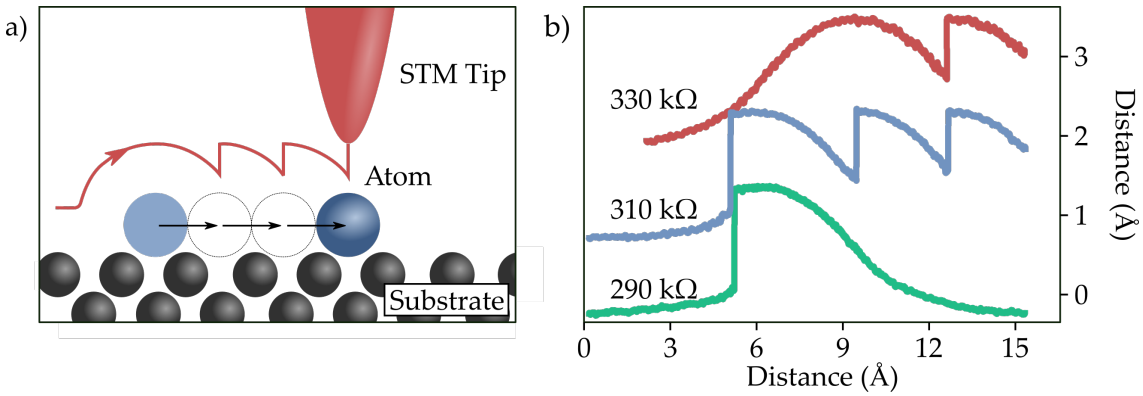

Figure 2.4: Lateral manipulation of atoms. **a)** Schematic representation of constant-current lateral manipulation showing the initial position of the atom in shaded blue, intermediate steps as white circles and final position in blue. The tip trajectory during manipulation is indicated by a red line. **b)** Tip height during lateral manipulation of Mn adatoms on β-Bi_2Pd at different junction resistances.

its value, different interaction mechanisms will govern the manipulation procedure. This is exemplified in Fig.2.4 b), a Mn adatom is displaced on the surface of β-Bi_2Pd using different junction resistances. As the junction resistance is lowered, the tip is set closer to the atom during manipulation and instead of pulling the atom in the desired direction it does so in the opposite one. This is the result of the variations in tip shape and structure, what results in different junction resistance requirements in different directions.

The precise interactions which result in the displacement of the atom strongly depend on the chemical composition of the tip apex, the atom species and the way the atom is bounded to the substrate. As a consequence, not every atom can be manipulated on every surface. The method explained here worked for Mn and, to some extent, for V. Lateral manipulation of Fe, Co, Ni was also tried unsuccessfully. Vertical manipulation, which consists on attaching an atom to the tip and then releasing it in a new position, was not effective in any case.

2.4 Experimental setup

The experiments shown in this work were carried in a commercial Low-Temperature system designed and manufactured by Specs GmbH. The system consists of a sample preparation chamber and an analysis chamber, both of them kept at pressures in the Ultra-High Vacuum (UHV) range in order to avoid contamination of samples. Both chambers are connected through a gate valve which can be opened to transfer samples and tips between them using a lateral manipulator.

The preparation chamber consists of standard sample preparation equipment that allows for sputtering and annealing of both samples and tips prior to transferal into the analysis chamber were experiments are carried out. During the time of this thesis a tip-preparation module was designed and installed in

this chamber with the purpose of heating up tips to high temperature and field-emission sharpening.

Experiments are carried out in the analysis chamber. It consists of an STM head attached to temperature-shielding liquid Nitrogen cryostat and a liquid Helium cryostat that cools the system down to 4.2 K. An additional refrigerator based on the Joule-Thomson cycle allows for further cooling of the STM head down to 1.3 K. Closed-cycle pumping of this refrigerator allows to lower the temperature down to 1K, the base temperature of the system. The STM head is surrounded by a superconducting magnet capable of producing magnetic fields up to 3 T perpendicular to the sample surface.

The STM head is surrounded by different shields that isolate it from external radiation sources. These shields can be opened temporarily in order to transfer samples or evaporate materials on the surface of a cold sample. All the electric wires entering the system but the tunneling current are filtered using either custom-made LC filters for the case of the bias voltage or π filters for temperature sensors and piezotubes control.

Bias voltage is provided by the electronic control unit (Nanonis v4) and it is added to an AC modulation provided by a 7270 DSP lock-in amplifier by AME-

Figure 2.5: SPECS UHV-LT STM system. Picture of the STM system used in this work.

TEK, Inc. using a passive summer circuit. The combined signal is divided by 1/100 and filtered by an LC filter before being sent to the sample. The tunneling current is recovered from the STM tip using a DLPCA-200 current amplifier and I/V converter fabricated by FEMTO Messtechnik GmbH and then is sent to both the inputs of the lock-in and the control electronics, the latter input having a custom-made RC filter.

Evaporation of metals is performed with the sample kept at low temperatures in the STM chamber using a EBE-1 e-beam evaporator commercialized by Specs GmbH. Evaporation is done from pure metal sources while the evaporator is pointed directly to the sample. Access to the sample is done through a shield opening that is closed after deposition. Deposition temperatures range between 4 and 15 K.

Chapter Three

Materials: β-Bi_2Pd

β-Bi_2Pd is a superconducting material that has recently made its way into many labs around the world. Depsite being discovered more than 60 years ago, recent findings on the unconventional nature of its band strucutre and the possibility of hosting triplet components have boosted interest on this material.

This chaper describes β-Bi_2Pd in preparation for the rest of the thesis. In the first part, we describe the main properties of the material and review recent research on β-Bi_2Pd. We describe the methodology employed to prepare clean surfaces by mechanical exfoliation. We then explain the procedure used to fabricate superconducting β-Bi_2Pd by indentation and characterize the energy resolution of the tips. In the last part, we show the superconducting gap of the material as characterized with β-Bi_2Pd tips.

3.1 Review of Recent Research

β-Bi_2Pd is a type-II superconductor from the family of Bi-Pd alloys[47] with a critical temperature of ∼5.4 K.[48] This particular phase crystallizes into a tetragonal structure with lattice constant a=3.362 Å where eight Bi atoms surround each Pd atom in the layered unit cell[49] (Fig.3.1 a). Consecutive layers are Van der Waals-stacked, defining an easy cleavage-plane perpendicular to the (001) direction.

Bulk β-Bi_2Pd crystals show an isotropic s-wave superconducting order parameter, despite experimental observations of multi-band effects.[48,51] The magnitude of $\Delta_{\beta\text{-}Bi_2Pd}$ found in literature oscillates between 0.76 meV and 0.8 meV depending on the growth procedure.[50,52,53] The thermal evolution of the superconducting gap is shown in Fig.3.1 c), where the working temperature of our system is indicated by a red arrow.

Early research on β-Bi_2Pdfocused on the study of multi-band superconductivity in this material[50–55], in part motivated by the initial of observation of Imai *et al.* of compatible effects in the temperature dependence of the upper critical field and specific heat.[48] Later Spin-Resolved Angel-Resolved PhotoEmission Spectroscopy (SR-ARPES) found that this material has a singular band structure for a superconducting material, with spin-polarized topological and trivial spin-

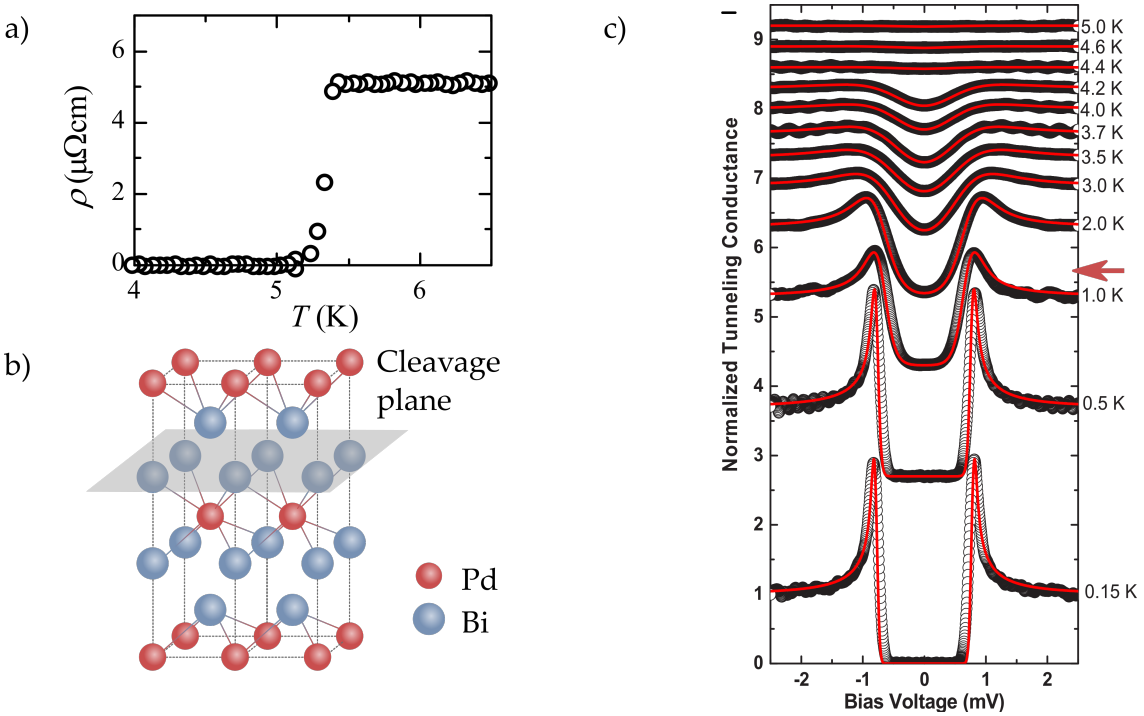

Figure 3.1: β-Bi_2Pdcrystals. a) Superconducting transition of β-Bi_2Pd. Resistance drops to 0 at ∼5.4 K. Reproduced from [48] **b**) Crystal structure of β-Bi_2Pdshowing the stacked Bi-Pd-Bi layers and the cleaveage plane. **c)** Temperature dependence of the superconducting gap in bulk β-Bi_2Pd. The working temperature of our system is indicated by a red arrow. Reproduced from [50].

polarized surface states crossing the Fermi level,[56] a discovery that boosted interest on this material due to the possibility of hosting triplet superconductivity[57].

Recent experiments have extended the in-plane spin-polarization to all the bands crossing the Fermi level, making it an even stronger candidate for non-conventional pairing. Fig.3.2 shows the Fermi surface of β-Bi_2Pd(a) as measured with ARPES[56], the spin polarization along the X axis calculated by Iwaya *et al.*[58] and a schematic representation of the spin polarization measured by Xu *et al.*.[59]. In the lower part, (d) shows the calculated dispersion of the bands and the surface states. (e) and (f) show ARPES and SR-ARPES momentum distribution curve, respectively[59].

To date no clear experimental signature of anomalous pairing has been observed in non-doped bulk crystals, but experiments on thin MBE-grown films[60], polycristaline rings[61] and doped bulk crystals[62] show good indicators of unconventional superconductivity. The discrepancy between the conventional pairing in bulk crystal samples and the aforementioned effects in other types of samples has been tentatively attributed to Dirac-fermion-mediated parity mixing and an increase in surface weight resulting from a chemical potential shift in thin films.[63] Whether in its bulk form, thin films or other types of samples, band-structure effects on the superconducting properties of β-Bi_2Pdstill remain largely unexplained and will for sure be subject to extensive research in the next years.

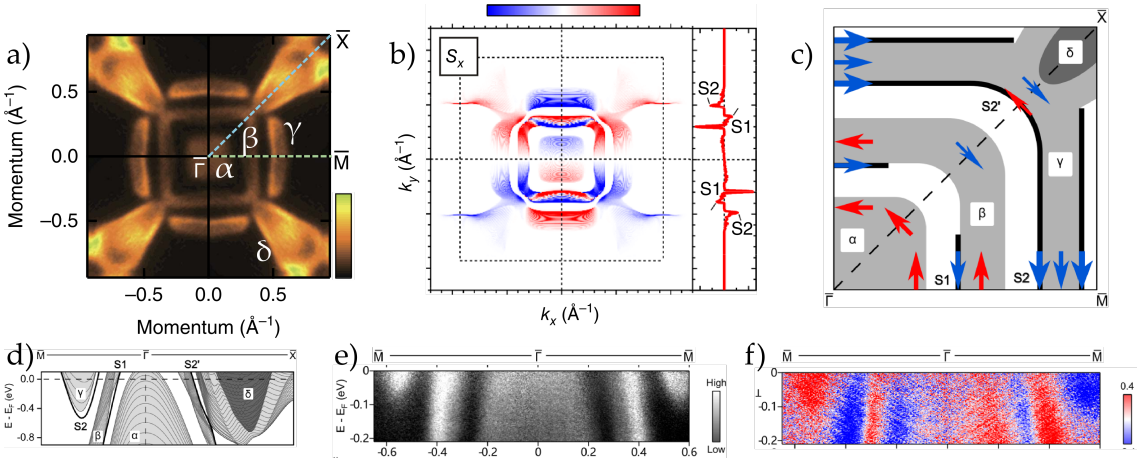

Figure 3.2: Spin polarization of the Fermi surface of β-Bi_2Pd. a) 4-fold symmetrized Fermi surface . Bulk bands are indexed with greek letters. Reproduced from [56]. **b)** Calculated spin polarization at E=+30 meV. Reproduced from [58]. **c)** Schematic representation of the experimental spin polarizations close to ϵ_F. Arrows indicate clockwise and anti-clockwise spin chiralities. Reproduced from [59]. **d)** Calculated electronic structure on the (001) surface. Reproduced from [59]. **e)** Momentum distribution curve along the $\overline{M\Gamma M}$. Reproduced from [59]. **f)** In-plane spin polarization along the $\overline{M\Gamma M}$ direction with the spin component perpendicular to the momentum. Reproduced from [59].

3.2 Sample preparation

The crystals used for our experiments were fabricated by Edwin Herrera, Isabel Guillamón and Hermann Suderow in Universidad Autónoma de Madrid using the procedure in Ref.[50]. Bi and Pd are introduced in a sealed quartz ampoule with He gas that is heated to 900 C and slowly cooled to 395 C to obtain the β phase of Bi_2Pd. The samples are then quenched to room temperature to avoid the formation of the RT-stable α phase of the material. The critical temperature of crystals grown using this technique is 5 K and they moderately lie in the dirty-superconductor limit, with a mean-free path l=15.3 nm and a coherence length ξ=23 nm[50].

Clean surfaces are obtained cleaving crystals in UHV conditions. Samples are glued onto Mo holders using low-temperature conductive epoxy (Lake Shore Cryotonics, Inc. ESF) or held using molybdenum plates, as shown in Fig.3.3 a). A piece of tape (Nitto SPV-224S) is adhered to the crystal surface before the sample is transferred into the UHV chamber. The sample is then placed in a room-temperature manipulator or in a sample slot at 77 K depending on the desired exfoliation temperature and the tape is removed using a wobble stick with tweezers at its end (see Fig.3.3 b). Due to the weak interlayer-coupling, the uppermost layers of the crystal stick to the tape, exposing a clean Bi-terminated (001) surface. After exfoliation, the sample is directly transferred into the STM head within seconds in order to avoid contamination.

Samples cleaved using this method present flat areas extending over several hundreads of nms with infrequent wrinkles caused by forces exerted during the exfoliation procedure[64] (Fig.3.4 a). Layer thickness is estimated to be ~6 Å from a line profile measured along a terrace step in Fig.3.4 b). The areas to which we refer as flat along this work (Fig.3.4 c) show a series of intrinsic vacancies and impurities that will be described in chapter 5. In the image, dark squares correspond to Bi vacancies. The square lattice of the Bi-terminated (001) surface

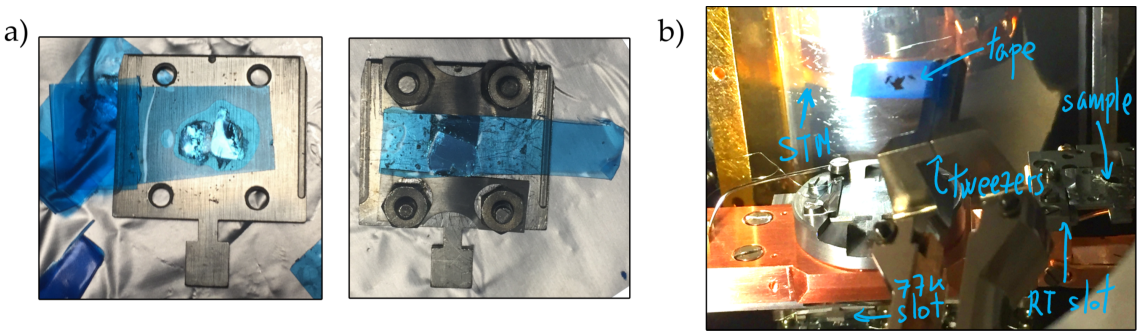

Figure 3.3: Clean Surface Preparation. **a)** Samples mounted in sample holder using conductive epoxy (left) or Mo plates (right). **b)** Exfoliation setup showing the tweezers holding a piece of tape after exfoliation. Exfoliation can be performed at room temperature or 77 K depending on which sample slot is used. The STM head is behind the shield indicated in the image.

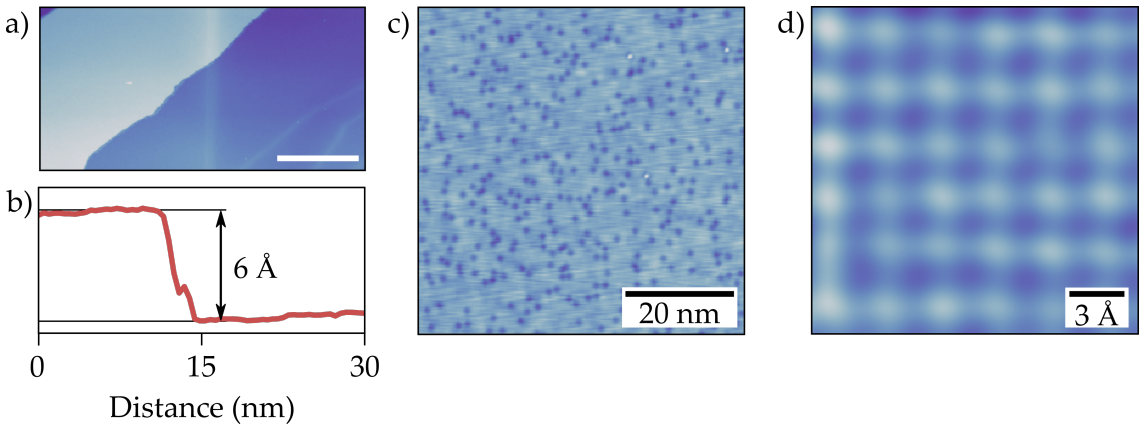

Figure 3.4: Topographic characteristics of samples. **a)** 400x200 nm area showing flat terraces. Wrinkles in the bottom right corner appear as a result of exfoliation. Inset bar corresponds to 100 nm. (V_{bias}=1 V, I_t=10 pA). **b)** Topographic profile along a terrace step. **c)** Flat 60x60 nm area in a sample exfoliated at low temperature. (V_{bias}=1 V, I_t=100 pA) **d)** Atomic resolution of the Bi(001) surface. (V_{bias}=3 mV, I_t=10 nA)

is resolved in the atomic resolution image in Fig 3.4 d) with a lattice parameter a=3.36 Å, in agreement with first-principle calculations.[65]

3.3 Tip preparation

Superconducting β-Bi_2Pdtips are formed by indentation of metallic tips into the sample surface. The tip is indented distances in the order of 20-30 nm while simultaneously moving in X or Y at slow speeds. As a result of the indentation, small β-Bi_2Pdgrains attach to the tip apex and a sample area of ∼200-300 nm around the indentation point is rendered unusable. As all the tunneling characteristics of these tips follow from the properties of the grains at the tip apex, we will refer to these β-Bi_2Pd-coated tips as β-Bi_2Pdtips for simplicity. β-Bi_2Pdspectroscopy using metallic and β-Bi_2Pdtips is shown in Fig.3.5 a). The spectrum measured with a metallic tip shows the thermally-broadened superconducting gap at the working temperature of 1.3 K. Using β-Bi_2Pd-coated tips, all the spectroscopic features are shifted by Δ_{tip} and the coherence peaks appear at $\pm(\Delta_{sample}+\Delta_{tip})$ ±1.58 mV.

The value of Δ_{tip} can be calculated from the energy of the coherence peaks. In view of our experimental value of ±1.58 mV, we estimate that the superconucting gap of the tip is similar to the one found in the bulk crystal and thus we approximate throughout this work as $\Delta_{tip} = \Delta_{sample} \simeq 0.79$ meV, in agreement with values found in literature.[50,52,53]

The degree of improvement in the energetic resolution of the measurement coming from the use of superconducting tips is extremely dependent on the properties of the grain attached to the tip apex. The energy resolution is defined as the full width at half maximum (FWHM) of the coherenece peaks. Lower FHWM transaltes into higher coherence peaks and hence the ratio between the coherence

peak height and the conductance in the continuum of states is an indicator of the energy resolution. In Fig.3.5 b) three diffferent β-Bi_2Pdtips are used to measure the superconducting gap of β-Bi_2Pd. The best energy resolution is obtained with the tip in the blue curve and the worst with the tip used for the curve in green. The curves are fitted as thermally-broadened superconductor-insulator-superconductor junctions with fixed Δ_{sample}=0.79 meV to calculate Δ_{tip} and the equivalent temperature broadening (values for each curve in figure). Using the tip in the blue curve an energy resolution equivalent to measuring with a metallic tip at a temperature of 0.23 K is achieved, 5.6 times better than the one obtained using metallic tips at the working temperature of 1.3 K.

The most common kind of tip formed during indentation corresponds to the lowest-resolution case in the previous figure. However, a series of procedures can be followed in order to ensure tips with high energy resolution are obtained. The chemical composition of the tip apex prior to indentation plays an important role. We found that freshly Au-coated W tips easily pick β-Bi_2Pdgrains and yield the best energy resolutions. Once they are coated with β-Bi_2Pd, succesive indentations degrade the energy resolution and eventually the tips stop being superconducting. We speculate that succesive indentations tend to destroy the crystal structure of β-Bi_2Pdgrains and therefore superconductivity at the apex is the result of proximitized Bi and Pd clusters.

The microscopic character of the grains attached to the tip manifests in the magnetic field dependence of its superconducting gap. Fig.3.5 c) shows different spectra measured above the upper critical field of β-Bi_2PdH_{c2} = 0.61 T[51], where the sample is brought into the normal state (for 0.5 T the spectra is taken in the center of a vortex core). Spectra shows a thermally-broadened $\sim \pm 0.79$ meV su-

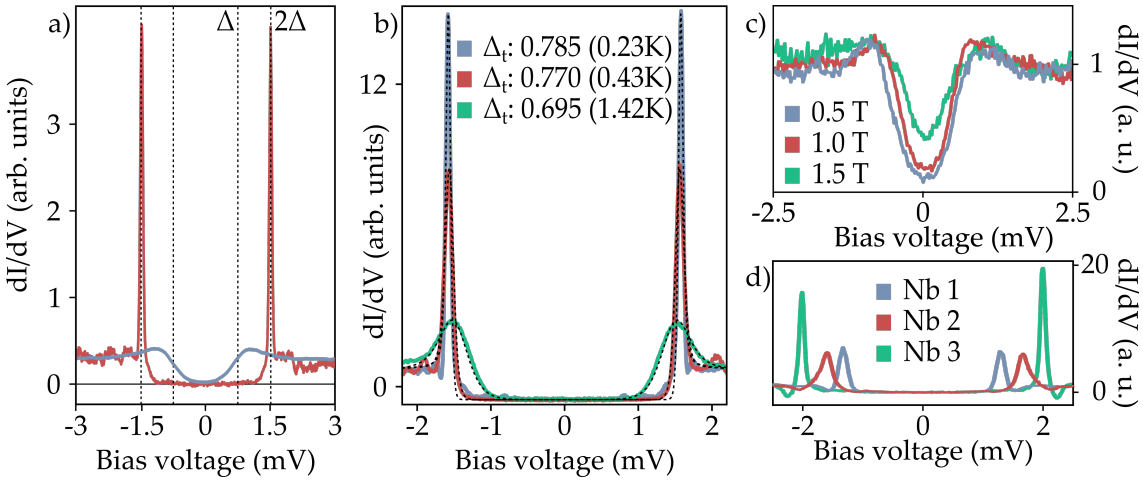

Figure 3.5: Characteristics of different superconducting tips on β-Bi_2Pd. a) Comparison of spectra on the bare β-Bi_2Pd surface using a metallic tip (blue) and a β-Bi_2Pd tip (red). **b)** Energy resolution from different β-Bi_2Pd tips. Legend shows the energy resolution achieved in each case. **c)**Effect of magnetic field on a β-Bi_2Pd tip. Note the substrate is not superconducting. **d)** Spectra measured on the bare β-Bi_2Pd surface using different Nb tips. *For all spectra shown here V_o=3 mV, I_o=300 pA, V_{RMS}=25 μV.

perconducting gap associated to the superconducting tip. 1.5 T are required to induce significant magnetic-field effects in the superconducting tip gap. The larger H_{c2} found in the superconducting tip is a characteristic effect found in small superconducting grains[66] and allows us to estimate that the size of the grains is effectively microscopic as expected from topographic maps measured in indentation areas.

We also searched for other types of superconducting tips which could manipulate atoms easily while preserving a clean superconducting gap. One of many candidates was Niobium. Nb wires, 250 μm of diameter, were cut in ambient conditions and then treated using different procedures. Field emission against a W wire[67], radiative heating, sputtering and electrochemical etching[68] all yielded not-clean and non-reproducible superconducting tips. Fig.3.5 d) shows three spectra taken on the surface of β-Bi_2Pdusing tips prepared by combinations of the previous methods. These tips show assymetric coherence peaks (Nb 3), unconventional tails (Nb 2) and negative conductance above the energy of the coherence peaks (all cases).The best spectra were obtained with tips that were cut, directly transferred into UHV and sputtered for several hours (Nb 1), although even in this case the gap of the tip would change upon succesive sputterings and dips would appear above the energy of the coherence peaks.

3.4 Single gap in β-Bi_2Pd

In the introduction we listed several experiments in which non-conventional pairing appears in non-bulk β-Bi_2Pdsamples. Although no traces of this coupling have been found in bulk samples, we wanted to verify this was the case in our samples. The main interest on reproducing a previous experiment performed with metallic tips at lower temperatures[50] was the possibility of resolving additional peaks close to the superconducting gap using superconducting tips. Although the energy resolution may not be significantly improved (our energy resolution is comparable to the one obtained at those temperatures), the convoluted densiy of states of the sample and the tip derivative is capable of resolving very-close peaks as peaks followed by a dip[69]. This effect, characteristic of SIS tunneling, allows to identify the presence of multiple gaps that would not be otherwise detectable using metallic tips with the same energy resolution.

In Fig.3.6 a) we show a spectrum measured between $\pm$ 3 mV. There is no signature of additional gaps in the region around the superconducting gap. Particularly, we see no dips appear in the vicinity of the main coherence peaks, thus allowing us to confirm the absence of a second gap in our crystals. In Fig.3.6 b) we reproduce the spectra measured by Lv and coworkers on a thin β-Bi_2Pdfilm[60], where the bulk gap appears as an assymetric pair of ipeaks inside the bigger surface gap associated to topological superconductivity. This surface gap appears at $\sim$2 meV in the thin film and is clearly absent in bulk crystal (would appear at $2+\Delta_{tip} sim 2.79$ mV).

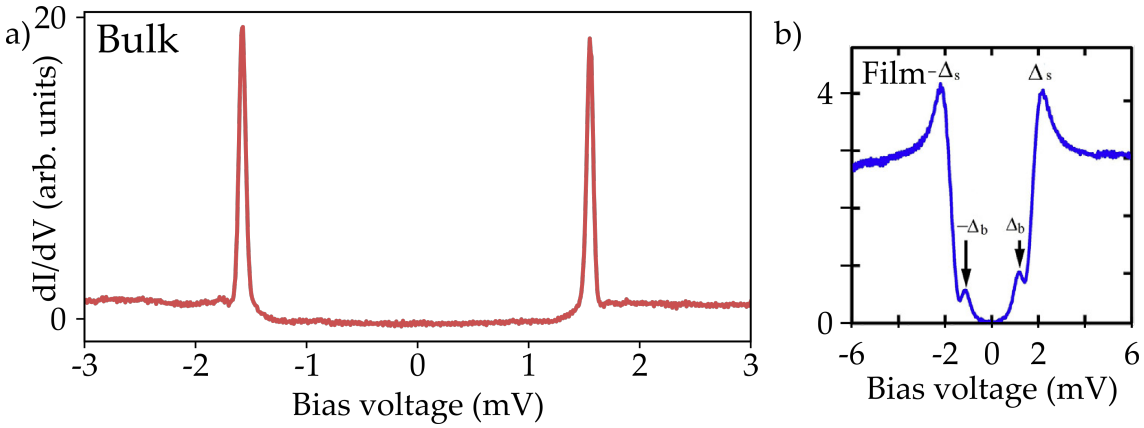

Figure 3.6: Comparing the spectra of bulk crystals and thin films. a) Spectra measured on the surface of β-Bi_2Pdusing a β-Bi_2Pd-coated superconducting tip. No foreign peaks or dips can be detected in its bias range. (V_0=3 mV, I_t=300 pA, V_{rms}=12.5 μV) **b)** Spectra measured on a β-Bi_2Pdfilm, showing both the bulk gap (Δ_b) and the topological surface gap (Δ_s). Reproduced from [60].

Attending to the slightly dirty limit in which these samples lie[50] and the presence of the topological surface state in bulk crystals[56], we propose besides interband scattering[50] and a Fermi level shift[63] impurities may also lead to the absence of the topological state in our samples. These would agree with the model proposed by Gusman for multi-band superconductors containing non-magnetic impurities[70]. In this extension of the Anderson theory of dirty superconductors[37] to multi-band systems, an intermediate limit between the dirty and clean superconductor levels of doping results in an effective band mixing in which a single-gap appears while the sample is not still in the dirty limit. This idea could be tested by evaluating the behavior of thin β-Bi_2Pdfilms under increasing numbers of point defects generated on the surface by Ar sputtering[71], what would provide an additional piece of information about the nature of superconductivity in this system.

Chapter Four

Spin-dependent Quasi-Particle Interference in the surface of β-Bi_2Pd

The spin polarization of the different bands in β-Bi_2Pd does not only influence the superconducting state, it has profound implications in the selection rules of quasiparticle scattering far from the superconducting gap.

In this chapter, we investigate the spin polarization of the bands in the (001) surface of bulk β-Bi_2Pdcrystals. We begin with the description of Quasi-Particle Interference and model how different characteristics of the band structure are reflected in the wavefunction of quasiparticles scattered by impurities. Using atomic resolution imaging, we identify the defects that act as scattering centers in bulk β-Bi_2Pd crystals. From the combined analysis of local LDOS variations around impurities and Fourier-Transform STM, we verify the spin polarization of the bands in our samples and the spin dependence of quasiparticle scattering.

The results obtained in this chapter serve as the starting point for the analysis of the excitations inside the superconducting gap.

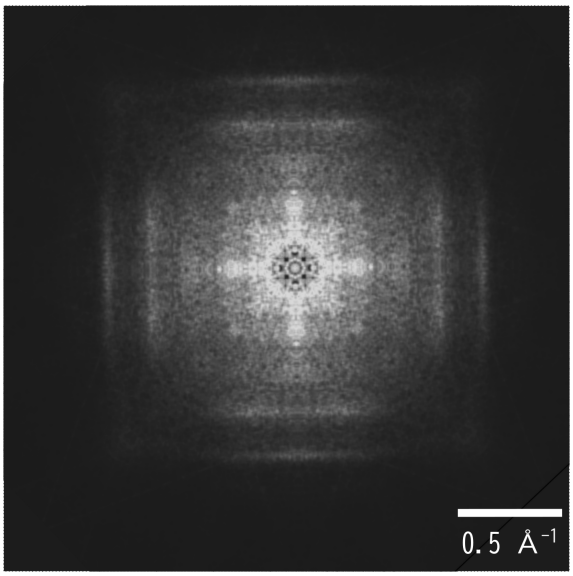

4.1 Quasi-Particle Interference

A significant part of material characterization involves the study of momentum-space properties such as the band structure of a material. Being a real-space technique, STM does not directly provide access to this fundamental piece of information. Nevertheless, its hallmark is imprinted in the wavefunction of the quasiparticles measured with STM and can be exposed by wave interference phenomena. Quasi-particle interference (QPI) studies modulations of the LDOS around impurities, a result of constructive interference between scattered quasiparticles with wavevectors defined by the band structure of the material. The scattering vectors can be identified by Fourier Transformation, hence providing an indirect mechanism to probe the band structure of materials.

From a microscopic point of view, an incoming electron is elastically scattered into another eigenstate by the point-like Coulomb potential created by an impurity[72]. In the absence of scattering, the incoming and outgoing electrons would be described by Bloch wavefunctions $\phi_{\mathbf{k}}$ and would have well-defined energy ϵ_k and momenta $\boldsymbol{k_1}$ and $\boldsymbol{k_2}$. Scattering mixes the electrons into a new eigenstate ψ constructed from the unperturbed $\phi_{\mathbf{k}}$s as:

$$\psi_{\mathbf{k},\sigma} = \sum_{\substack{\mathbf{k} \\ \mathbf{k}\in\epsilon_k}} \alpha(\mathbf{k})\phi_{\mathbf{k},\sigma} \tag{4.1}$$

where perturbation theory shows that the wavevector of the resulting state ψ is given by $\boldsymbol{k_q} = \boldsymbol{k_1} - \boldsymbol{k_2}$[73].

The band structure of a material defines the energies and momenta of its electrons. A constant-energy cut at a given energy E will therefore contain all the k-space information about the possible $\boldsymbol{k_1}$ and $\boldsymbol{k_2}$ that can form a scattering state

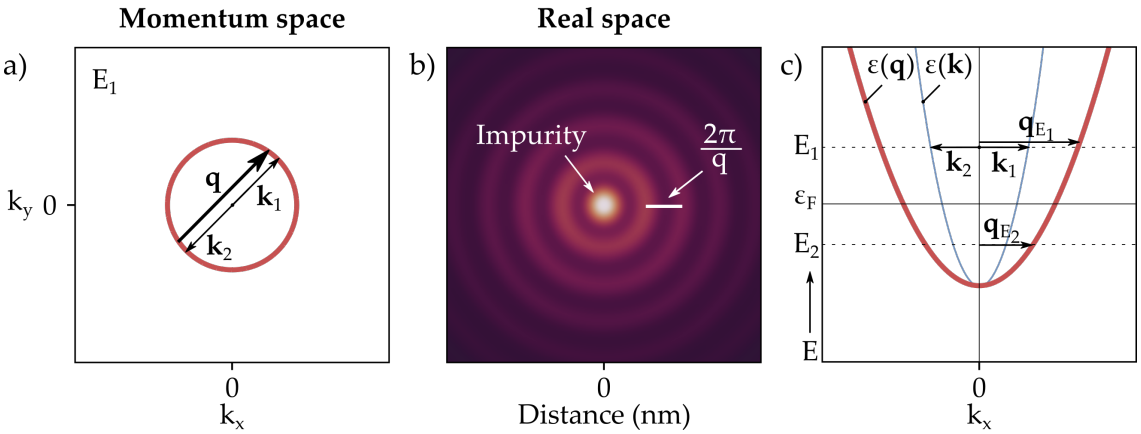

Figure 4.1: Impurity scattering of free electrons. **a)** Constant-Energy Contour at E_1 showing two wavevectors $\mathbf{k}_1$ and $\mathbf{k}_2$ and the associated scattering vector $\mathbf{q}$=$\mathbf{k}_1$-$\mathbf{k}_2$. **b)** Real-space modulation of LDOS showing a characteristic period defined by the scattering vectors. **c)** Electron dispersion of a free electron (blue) showing how the scattering vector $\mathbf{q}_i$ changes at different energies, defining a new scattering vector dispersion (red).

at that energy. We will refer to these cuts as *k*-space Constant-Energy Contours (CEC), among which the Fermi surface is the particular case at E=ϵ_F. Scattering states ψ will equivalently have an associated CEC defined by all the possible $\boldsymbol{q}$ resulting from combinations of $\boldsymbol{k_1}$ and $\boldsymbol{k_2}$, to which we refer as *q*-space CEC.

For a circular CEC as the one shown in Fig.4.1 a), perturbation theory shows that the sum of two scattering electrons results in the formation of a standing wave with wavevector $\mathbf{q}$ = $\mathbf{k}_1$ - $\mathbf{k}_2$[73] . Summing over all the $\phi_{\mathbf{q},\sigma}$ defined by the CEC at E_1 results in the standing wave in Fig.4.1 b). This standing wave can be probed with the STM, thus providing access to momentum-space properties of the material.

In the same way the dispersion relation of free-electrons defines the availabe $\boldsymbol{k_1}$ and $\boldsymbol{k_2}$ at a given energy, the scattering vectors $\mathbf{q}$ will have a dispersion relation that derives from the free-electron one. Fig.4.1 c) shows how scattering-vector dispersion is defined. For each energy, the modulation of LDOS will change in accordance to the scattering-vector dispersion, thus providing an indirect real-space signature of the electron bands.

Surface States, Bulk Bands and Vector Nesting

The microscopic description of the scattering process in QPI does not explicitly deal with the effect of the system dimensionality on the formation of standing waves. The change from bulk bands (3D) to surface states (2D) manifests as an increase in the extension of the standing waves.

Three different CECs are shown in Fig4.2 with their associated real-space LDOS modulation and the q-space CEC obtained as the self-correlation of the k-space CEC. In each case, the scattering vector $\mathbf{q}$ is plotted as originating from different points of the CEC.

For the bulk-like band in a), many different scattering vectors can equally contribute to QPI. Focusing on the k_x axis, $\mathbf{q}$ is just one among the many possible scattering vectors. The resulting q-space plot shows a continuous number of possible scattering vectors. As a result, the LDOS distribution around the impurity does not show a clear oscillating pattern because it lacks a dominating scattering vector, and the sum of all the possible ones results in destructive interference.

For the surface-state-like CEC in Fig.4.2 b), the picture is different. Along the k_x axis, there is a single scattering vector $\mathbf{q}$. This is the only available vector along this direction, and its magnitude is the same as that of all the other scattering vectors passing through zero. This results in a $\mathbf{q}$-dominated momentum space. The associated spatial distribution of the LDOS modulations shows a clear wavevector defined by $2\pi/|\mathbf{q}|$.

A third CEC is shown in Fig.4.2 c). This case represents a quasi-1D CEC, with a pair of flat areas yielding an increased number of $\mathbf{q}$. This phenomenon is known as vector nesting or electron focusing and dominates the formation of the

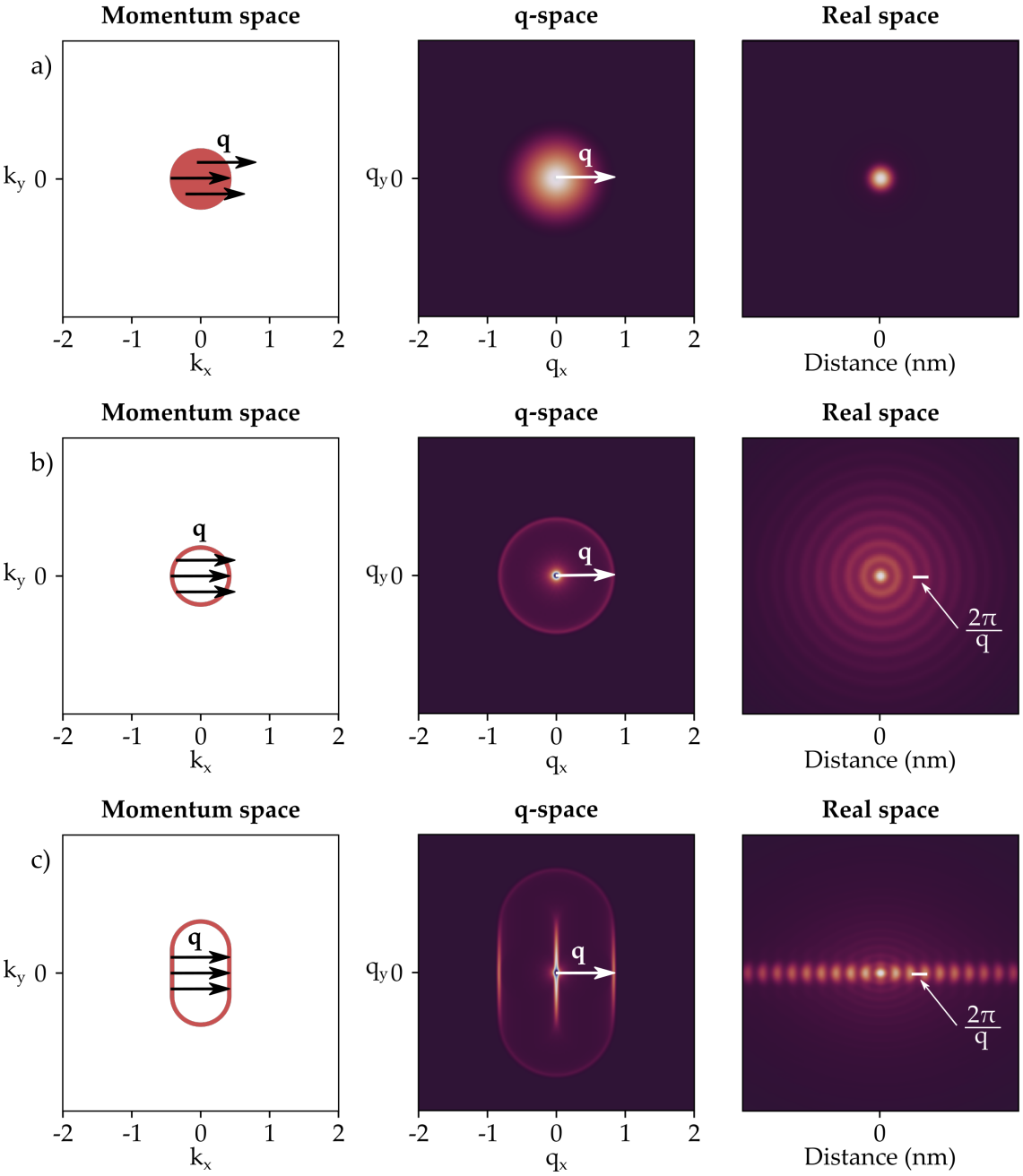

Figure 4.2: QPI from surface states and bulk bands. a) QPI from a filled CEC, resembling a bulk band. The real-space modulations and q-space intensity lack a defined scattering vector. **b)** QPI from a contour CEC, resembling a surface state. In this case the patterns reflect the scattering vector magnitude. **c)** A contour CEC with nesting vectors shows an increased decay length of LDOS modulations and an increased intensity in q-space for the nested vectors.

q-space plot. The corresponding LDOS is dominated by these vectors, showing a longer-ranged coherence path along the direction over which nesting occurs.

A comparison between the three previous cases shows the sharp CEC edges and flat areas present at each dimension increase the coherence length of the

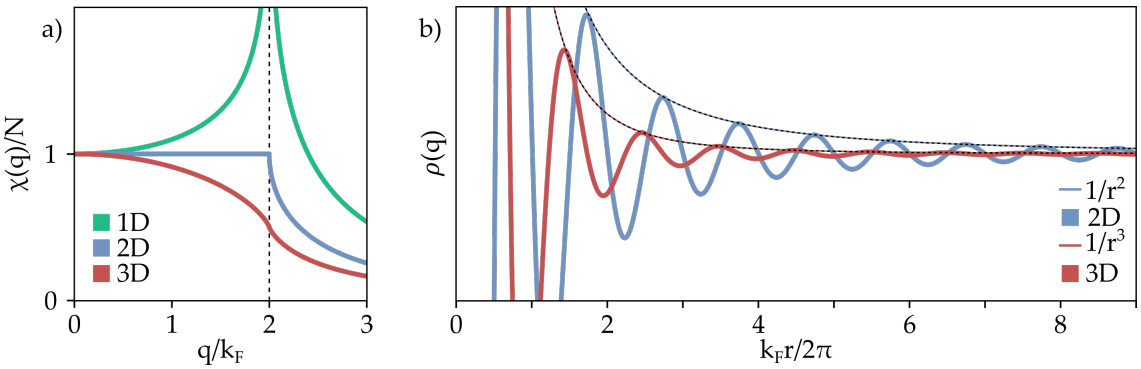

Figure 4.3: Lindhard response function a) Normalized Lindhard response function for different dimensions d. **b**) Fourier transform of the Lindhard response function, showing the density modulations around an impurity located at 0. A fit

LDOS modulations. A more explicit derivation of this idea can be formulated from linear response theory. Under this framework, the scattering problem at the Fermi level is analyzed in terms of the charge density required to screen the electrostatic potential induced by the impurity[74]. When an impurity is placed on the surface of a metal. it induces an excess charge. As no long-range electric field can persist in a conductor, conduction electrons screen the excess charge in short distances. The accumulation of conduction electrons in the vicinity results in the increased LDOS around the impurity with its characteristic modulation and decay. In the random-phase approximation, this charge distribution around the impurity is described by the Fourier transform of the q-dependent Lindhard response function $\chi(\mathbf{q})$.[75]

The Lindhard response function depends on the dimensionality of the system, showing discontinuities (either itself or its first derivative) at $\mathbf{q} = 2\mathbf{k}_F$ (see Fig.4.3 a). Its Fourier transform reflects this discontinuity as a modulation with period $\mathbf{q}/2\pi$ in the charge density distribution. As the character of the discontinuity depends on the dimension, so do the charge modulations. Particularly, lower dimensions show a more pronounced discontinuity and a more extended charge modulation, as depicted in Fig.4.3 b). In the 3D case, modulations decay in the vicinity of the impurity following r^{-3}, whereas for 2D the decay is r^{-2}. The 2D or 3D character of a Fermi surface will manifest thus in the range of the LDOS modulations. Vector nesting increases the extent of these modulations, what results in an effective lower dimensionality of the system.

Anisotropy: Fourier-Transform STM

Local variations of the DOS at fixed energy are mapped in dI/dV maps. For the case of QPI, these maps show the sum of the standing waves at each impurity, forming a wave interference pattern. The period of the oscillations can be directly measured in line profiles and the associated scattering vector obtained from the periodicity.[76,77] When the number of impurities is high or the CEC is not simple, the picture becomes more complex, which may prevent direct identification of

the scattering vectors. In such cases, the scattering wavevectors are measured through the Fourier-transform of the dI/dV map.

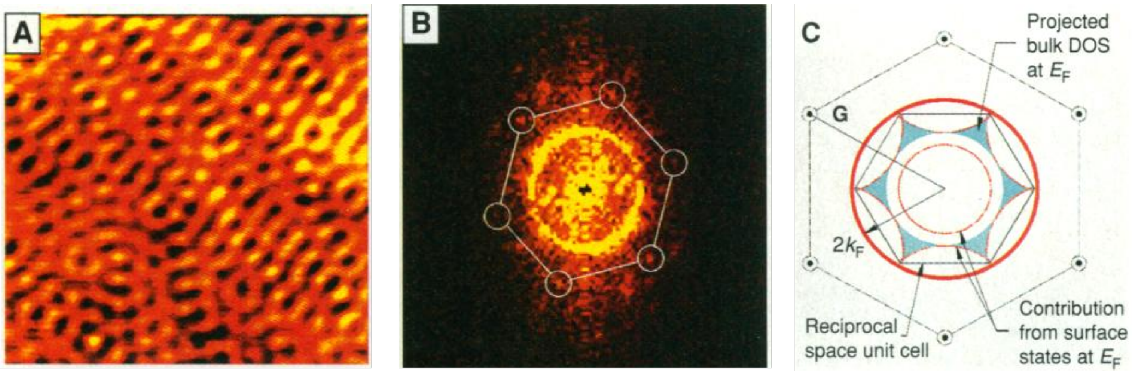

Figure 4.4: Fourier-Transform STM. a) STM image of LDOS modulations at the surface of Be(0001) at V=+4 mV and I=1.5 nA. **b)** 2d Fast-Fourier Transform of a). **c)** Fermi surface of Be(0001) showing the vectors that contribute to the formation of the oscillatory pattern.* a), b) and c) reproduced from[78]

The wave-interference pattern in Fig.4.4 a) shows the modulations at the surface of Be(0001) as an example of a more complex LDOS modulation[78]. Applying a Fast-Fourier Transform algorithm, the modulations in real space are translated into momentum space and the scattering vectors identified from the resulting image, as shown in Fig.4.4b) and Fig.4.4 c).

Using this technique, not only the scattering vectors but also their direction can be easily extracted from dI/dV maps. The shape of the CEC dictates the direction of the scattering vectors, and thus this technique provides information about the symmetry of the band structure of the material[79] Fig.4.5 shows the effect of a different CEC shape in the formation of standing waves and the corresponding q-vector space accessible with the STM.

A square-shaped CEC yields cross-shaped standing waves around the impurity, as shown in Fig.4.5 a). A similar square characterizes its correpsonding q-space, but the sides of the square are double the k-length of the generating CEC. Similarly, an hexagon-shaped CEC translates into 6-fold symmetric standing waves and the formation of a hexagon in q-space. In both cases, the periodicity of the modulations corresponds to the maximum scattering vectors, and both real-space and q-space maps share the symmetries of the generating CECs.

The q-space maps in Fig.4.5 a) and b) also contains smaller vectors, as can be seen in the non-zero value inside the square. These smaller scattering vectors correspond to other points connecting the CEC as the ones denoted by unlabeled arrows and account for the non-zero intensity. However, the presence of nesting vectors dominates the formation of the LDOS modulations and the q-space map.

Scattering vectors define symmetric q-space CECs due to the time-reversibility of the scattering process. If **q** exists, then **-q** must also exist. A hypothetical triangular shape would thus result in a similar pattern as the one defined by a

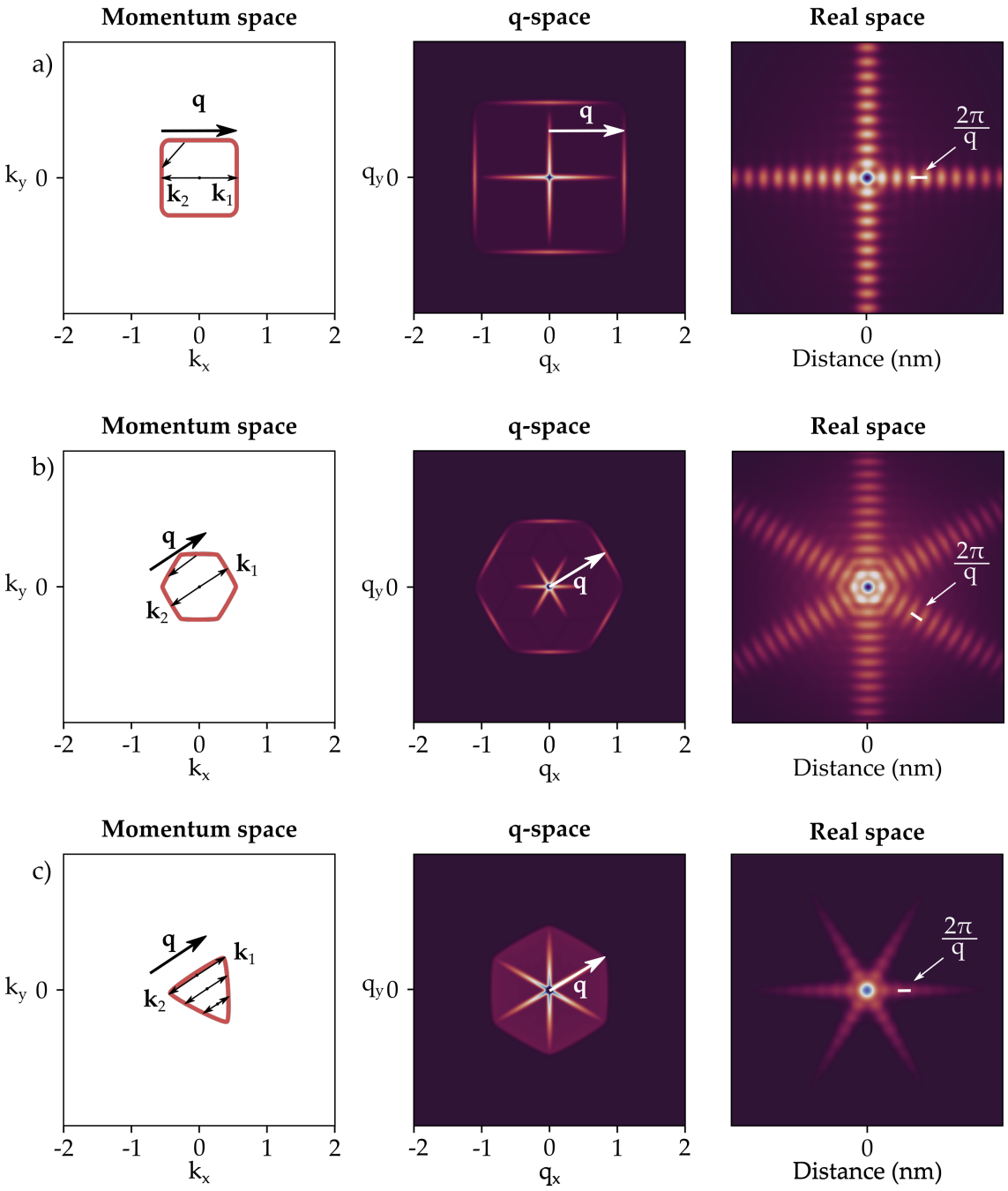

Figure 4.5: QPI from anisotropic CECs. The influence of the CEC shape on the construction of q-space and the symmetries of the real-space LDOS modulation visualized in: **a)** Square CEC **b)** Hexagonal CEC **c)** Triangular CEC

hexagonal CEC, as seen in Fig.4.5 c). Both configurations yield 6-fold symmetric standing waves and q-space CECs, but there are notable differences between the two cases. In real space, the decay of the standing wave pattern is much faster and resembles the shape of a star instead of the clear line-like extension found for a hexagon. In q-space, the difference manifests in the absence of a maximum at the edges of the hexagonal q-space map. This is the result of the absence of

flat areas in the k-space CEC and is responsible for the faster decay found in real space.

From this last example, the necessity of knowing the band structure of the material becomes evident. Otherwise, QPI patterns may be misleading. This would, in principle, disregard QPI as a suitabke characterization technique. In the next section, we show this is not the case and how the combined study from both perspectives provides an additional layer of information.

SPIN-DEPENDENT SCATTERING

In the last section, we showed how the shape of a CEC defines q-space. There are cases in which this one-to-one correspondence does not hold. The formation of a scattering vector relies on the sum of wavefunctions with different **k**, but other degrees of freedom may prevent the formation of such eigenstates.

Standing waves are the result of constructive interference of wavefunctions with different **k**, but interference can only happen between non-orthogonal eigenstates. Wavefunctions with different spin violate this non-orthogonality, and thus scattering vectors cannot be formed between areas of the CECs with different spin[80].

In Fig.4.6 we compare the case of two similarly-shaped CECs with different spin configurations. 4.6 a) shows a spin-degenerate CEC. As no restriction applies to the scattering vectors, the two bands can combine in the four main configurations shown in the left frame. In real space, this translates into a doubly-modulated standing wave showing a beat-frequency pattern. As no restriction limits the possible scattering processes, the number of squares corresponds to n^2 = 4, where n=2 is the number of bands. Note the sides of the squares reflect the length of the k-space CEC contours.

A spin-polarized CEC shows completely different behavior. In this case, only those scattering vectors that preserve spin are allowed. In 4.6 b) the different spin orientations are indicated with colors and arrows, showing that there is only one possible scattering vector. Both the standing wave pattern and the q-space contours are strongly modified by this reduction of possible vectors. The wave pattern now displays a single modulation with a characteristic wavevector defined by the inter-band spin-preserving scattering vector. A single square appears in q-space, reflecting that a degree of freedom prevents some of the scattering vectors.

Using this combined technique, one can compare the band structure of a material with the experimental q-space map obtained from FT-STM to infer properties of bands and allowed inter-band and intra-band scattering processes. This analysis does not restrict to spin; other degrees of freedom, such as the pseudo-spin in graphene, have also been probed using this methodology.[81]

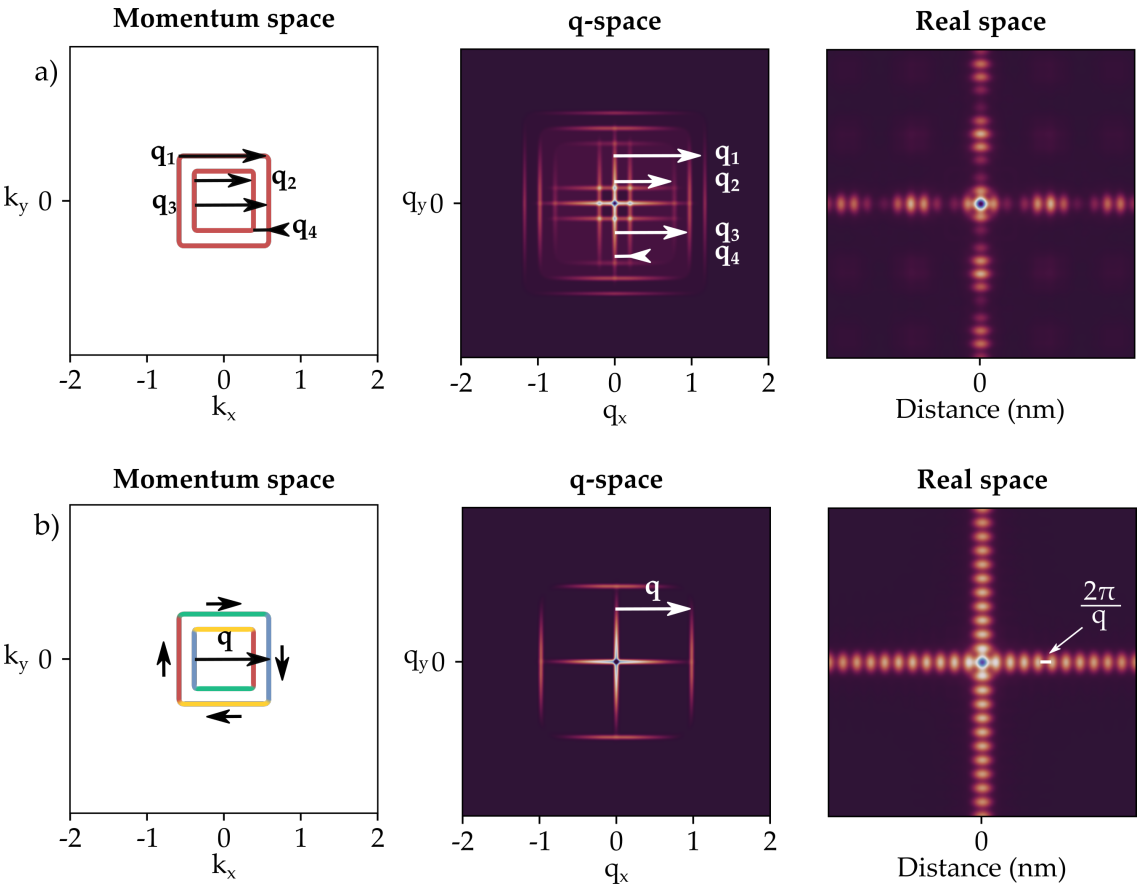

Figure 4.6: Role of spin in QPI. a) QPI from two spin-degenerate square CECs, showing all the availabe scattering vectors along k_x. The associated LDOS modulation is the result of the different scattering vectors. **b)** QPI from two chiral spin-polarized CEC with the polarization defined by the different colors. Some of the previous scattering vectors are absetn due to the orthogonality of the initial and final states.

4.2 Sources of scattering in β-Bi_2Pd

Scattering centers are a requirement for visualizing the oscillatory patterns associated with QPI. β-Bi_2Pd presents intrinsic defects that facilitate quasiparticle scattering on its surface. In this section, these defects are analyzed and identified by means of atomically-resolved topography and their behavior during lateral manipulation.

The as-exfoliated surface of β-Bi_2Pdshows a high density of defects, as seen in Fig.4.7 a). The topographic map, measured at -0.6 mV, shows three different topographic features associated with defects: dark square-shaped dips (d_A), small adatoms (d_B), and high adatoms (d_C). An area of 80x80 nm shows 620 defects of the first kind, 341 of the second, and 96 of the last. The density of defects of the first two kinds is similar to the one found in another STM work in similar β-Bi_2Pd crystals[58], whereas the number of d_C defects in our crystals is higher but strongly dependent on the exfoliation temperature (samples cleaved at 77K show no trace of d_C defects).

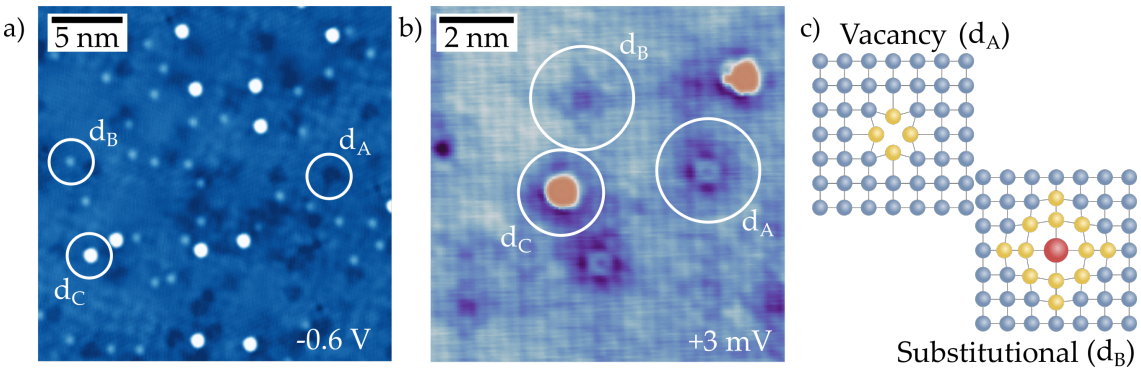

Figure 4.7: Scattering centers in β-Bi_2Pd. a) STM topography of a 25x25 nm showing the defect density at high bias. The circled areas correspond to: vacancy (d_A), substitutional defect (d_B) and Bi adatom (d_C). (V_{bias}=-0.6 V, I_t=6 nA). **b**) Topographic map of a 10x10 nm area showing atomic resolution of the lattice and defects. (V_{bias}=3 mV, I_t=1 nA). **c**) Schematic representation of two kind of defects and their effect on the crystal lattice. Yellow indicates Bi atoms displaced from their equilibrium position.

Bias voltage greatly influences the overall appearance of defects d_A and d_B. Fig.4.7 a) and b) show a comparison of the apparent shape of the different impurities at different voltages. d_A defects are imaged at -1 V as square-shaped ∼25-pm dips, d_B as 25-pm protrusions and d_C as 1 nm-high adatoms. When voltage is reduced to 3 mV, only d_C defects preserve their former appearance; d_A defects resemble a ring contained in an empty rhomboid and d_B defects appear as atomic-sized squares surrounded by a cross-shaped pattern.

When Mn or V impurities are added to the surface and positioned in the vicinity of impurities d_A, we find these defects 'capture' Mn and V adatoms when placed less than three atomic units away. When the adatoms are 'captured', they move to the center of the impurity site, which corresponds to a lattice Bi site. The apparent height of Mn and V reduces to ∼80 pm when placed in the new position and they cannot be further manipulated from this site. Defects d_B, on the other side, do not have a noticeable effect on the lateral manipulation of V or Mn. The adatoms can be positioned in the immediate surroundings of the defects without suffering any perturbation and they can be removed from the site using the usual manipulation parameters.

In view of the behavior of Mn and V in the vicinity of d_A impurities, we identify them as Bi vacancies. Fig.fig:Q.Fig7 c) sketches a proposed model of the atomic lattice in the absence of a Bi lattice atom. The four first-neighboring atoms are brought into the vacancy site, resulting in the ring-shaped feature found in atomically resolved maps. The ring is connected to the four diagonal Bi atoms which are now the first neighbors of the displaced atoms. A dip-like feature is left in the former position of the displaced atoms, approximately in the lattice site where these atoms would lie if a Bi atom were placed in the vacancy site. The vacancy is associated with a highly reactive site that chemically bonds V and Mn in its vicinity, in agreement with the experimental observations.

The apparent shape of d_B impurities at high voltages and their transparency for lateral manipulation of V and Mn indicate they are substitutional defects. Due to their different electronic configuration, they appear higher/smaller than Bi atoms around depending on the bias voltage. As their size is also different, the Bi lattice around suffers the local displacement found in atomically-resolved images. Furthermore, the defects are centered in a Bi atom site in accordance with the expected position of a substitutional defect. The proposed structure of the defect is sketched in Fig.fig:Q.Fig7 c). The high density of substitutional defects found in the samples and their homogeneous behavior suggests that these defects are Pd atoms occupying Bi sites.

Topographic imaging shows that d_C impurities resemble the shape of an adatom at every bias voltage. From atomic resolution pictures, we find they lie on top of Bi adatom sites, which is expected to be the least stable adsorption site for an adatom. Using lateral manipulation, we find they cannot be displaced from that position, a possible indicator of the formation of a chemical bond to atoms underneath. Another striking property of these defects is the strong dependence of their number with exfoliation temperature. Taking all these effects into consideration, we identify these impurities as Bi impurities lying on vacancy sites. Close inspection of the atomically-resolved image in Fig.4.7 b) shows a vacancy-like dip below the d_C, strengthening our proposition.

The chemical identification of these adatoms follows from the exfoliation in UHV conditions (P<10^{-10} mbar), excluding the possibility of finding foreign atoms on the surface. The surfaces exposed during exfoliation are Bi-terminated both in the crystal and the exfoliated layers, making it more feasible for these atoms to reach the surface than for Pd. The role of temperature is not clear from our observations, but the combined effect of mechanical deformation and room-temperature seems to promote the diffusion of atoms from the lattice to the surface of β-Bi_2Pd. These atoms diffuse over the nearby areas and bond to the reactive vacancy sites, from where they cannot be removed using lateral manipulation. This behavior is compatible with the binding to vacancy sites found for Mn and V.

Comparison of the number of vacancies with the number of Bi adatoms present on the surface (6:1) indicates the primary source of vacancies is not the promotion of lattice Bi atoms. Although a vacancy must be generated for each Bi adatom, the remaining vacancies must appear during crystal growth and cannot be minimized by changes in the exfoliation procedure. The number of substitutional defects is also exfoliation-independent and must then be the result of crystal growth.

4.3 QPI from Spin Polarized-Bands

In the first section of this chapter, we described how the spin-polarization of a material can be detected using QPI. Following the work by Iwaya *et al.*[58], we

study QPI on the surface of β-Bi_2Pd in order to confirm the spin-polarization of the bands in our samples.

In preparation for the study of QPI, a β-Bi_2Pd sample is exfoliated at room temperature and directly transferred to the STM head without any additional adatoms evaporated on the surface. Using this procedure we find the defect density shown in Fig.4.8 a), with an evenly-distributed number of defects of the three kinds. The dI/dV signal is simultaneously acquired while the surface is scanned in constant-current mode, generating the conductance map shown in Fig.4.8 b). An interference pattern forms all over the map, with dark and light patches randomly distributed along the scan area. A zoom into a 24x24 nm area shows no pinning of the modulation by defects. The interference pattern is the result of constructive interference between standing waves generated at nearby defects. The scattering centers do not pin the modulations and whether all defects behave as scatterers cannot be deduced from conductance maps at this defect density.

Following the methodology described in the introduction, we calculate the FFT of the conductance map in order to identify the scattering vectors giving rise to the interference pattern. The 4-fold symmetrized FFT at +50 mV is plotted in Fig.4.9 a). The q-space map shows 6 concentric squares with their sides perpendicular to the $\overline{\Gamma M}$ direction. The main scattering vectors correspond to the edges of these squares. Quantification of the scattering vectors is performed by visual analysis of the FFT map, marking the upper and lower limits of each edge. The resulting scattering vectors are plotted in Fig.4.9 b) on top of an intensity plot showing the averaged intensity in an area 1.25 $Å^{-1}$ above and below the $\overline{\Gamma M}$ axis. The values are listed in the table in Fig.4.9 c), where the error is estimated from the width of the square edges.

Comparison with ARPES measurements[56] shows a discrepancy between the expected number of scattering vectors and the experimentally observed ones. A system with five concentric bands along $\overline{\Gamma M}$ should show $5^2 = 25$ scattering vec-

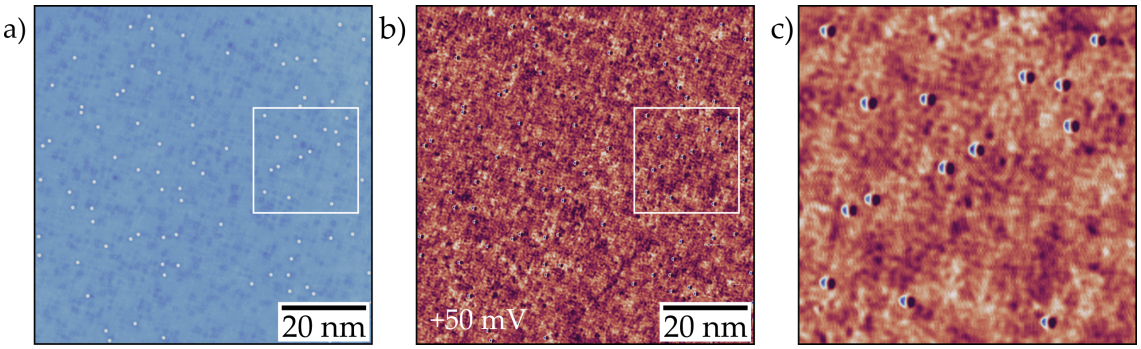

Figure 4.8: Quasi-Particle Interference at +50 mV. a) Topographic map of an 80x80 nm area showing the amount and distribution of defects. **b)** Simultaneously-acquired dI/dV map shoing the modulations associated to QPI. (V_o=50 mV, I_o=500 pA, V_{RMS}=100 μV). **c)** Zoom into the area marked by a white square, showing the modulations of dI/dV around defects. The modulations are homogeneously distributed along the area.

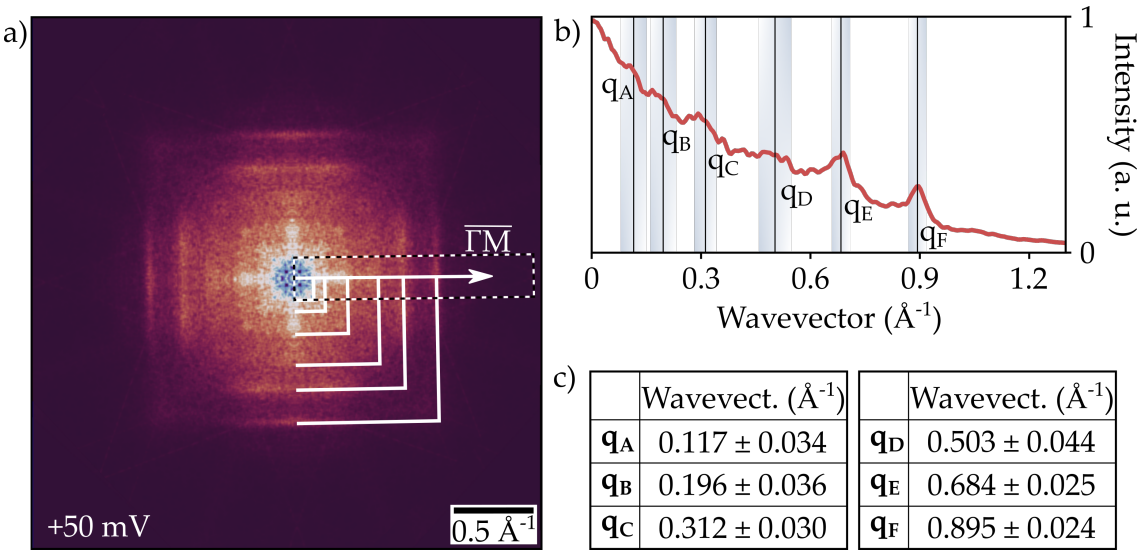

c)

	Wavevect. (Å^{-1})		Wavevect. (Å^{-1})
q_A	0.117 ± 0.034	q_D	0.503 ± 0.044
q_B	0.196 ± 0.036	q_E	0.684 ± 0.025
q_C	0.312 ± 0.030	q_F	0.895 ± 0.024

Figure 4.9: Scattering vector estimation from FFT. a) 4-fold symmetrized 2D-Fast Fourier Transform of the dI/dV map at +50 mV. Each square corresponds to a different scattering vector. **b)** Accumulated intensity in the area marked by a dotted square around the $\overline{\Gamma M}$ axis in a). Vertical lines indicate the scattering vectors and shaded areas indicate the estimation error. **c)** Table shows the estimated scattering vectors in a).

tors in q-space. In our case, only 6 scattering vectors are observed in FFT maps, indicating that a degree of freedom is preventing some of the scattering processes. From the calculations of the spin-polarization of the bands in β-Bi_2Pd performed by Iwaya *et al.*, we identify this degree of freedom as the in-plane polarization of quasiparticles in the bands.

The spin polarization of the bands along the y-axis as calculated in Ref.[58] is shown in Fig.4.10 a). Taking this calculation as a model, we define the CEC shown in Fig.4.10 b). Using this CEC for bands polarized along the Y-axis and rotating it 90 degrees for states polarized along the X-axis, we calculate the self-correlation in order to obtain the q-space intensity plot in Fig.4.10 c). The q-space map shows great agreement with the number of scattering vectors found in the experimental FFT. The squares which were used as an indicator in the experimental map are plotted on top of the calculated scattering vectors, showing the values obtained in the calculation match the ones measured experimentally.

The comparison between the calculated q-space and the experimental FFT shows the scattering vectors can be easily reproduced by this simple model. The filled areas found in the FFT are not captured in the model because the non-polarized inner structure of bands α and γ has not been taken into account. If included, they would contribute only by filling the areas between scattering vectors, but the edge scattering vectors would still have the same values (see Fig.4.5 c).

The calculated q-space shows that 6 scattering vectors are generated if only spin-preserving scattering vectors are considered. Direct comparison between

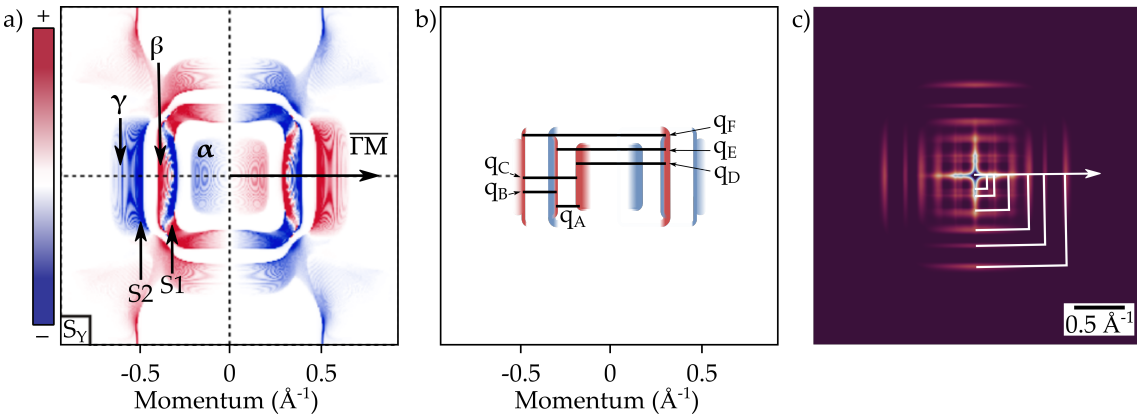

Figure 4.10: Scattering vector model. a) Calculated spin-polarization along the y axis of the bands at +30 mV. The different colors indicate the degree of polarization of the band at that energy. Reproduced from[58] . **b)** Spin-polarized CEC used for the q-space plot. The arrows indicate the bands connected by scattering vectors.**c)** q-space intensity plot for the spin-polarized CEC shown in b). White squares correspond to the experimental measurement.

the proposed CEC and the q-space map allows us to identify the scattering process giving rise to each scattering vector, which are summarized in the next table:

Vector	Bands	Wavevector ($Å^{-1}$)
q_A	S1 - α	0.117
q_B	S1 - S2	0.196
q_C	S2 - α	0.312
q_D	α - β	0.503
q_E	S1 - β	0.684
q_F	S2 - β	0.895

where the bands are labeled using Greek characters and the surface states as S1 and S2, following the terminology used in previous chapters.

As expected for a chiral in-plane polarization, no inter-band scattering is allowed in our β-Bi_2Pd samples. Instead, we find all the spin-preserving inter-band processes contribute to the interference pattern and extract the values of their associated scattering vectors. Our result is in agreement with the results obtained by Iwaya and coworkers and further extend their observations to the whole set of bands. Surface state S2 and band γ behave as an individual entity as expected by their proximity and their equivalent spin-polarization but, otherwise, all the bands can be identified in the FFT at +50 mV.

4.4 Conclusions

Combining our experimental quasi-particle interference maps with first-principles calculations, we have been able to verify the in-plane spin-polarization of all the

bands in β-Bi_2Pd. Using a simplified CEC model, we have captured the behavior of the real system and identified the scattering processes in our samples.

The implications of the results found in this section go beyond the identification of the bands and their spin polarization. From the values of the scattering vectors and their identification, we derive some of the properties of impurity-induced bound states in superconductors in the following chapter. These results also confirm that our samples preserve the theoretically-predicted band structure of β-Bi_2Pd.

Chapter Five

Band and spin selectivity of YSR states

The wavefunction of YSR states encodes information from both the magnetic impurity and the superconducting host into a single state. The spin configuration of adsorbed adatoms, the effective dimensionality of the Fermi surface of a superconductor or the particular orbitals giving rise to YSR states can be derived from the number of YSR states and their spatial distribution.

In this chapter, we study the asymptotic behavior of YSR excitations induced by vanadium atoms deposited on the surface of β-Bi_2Pd. From the number of YSR states and their spatial distribution around the atom, we identify the spin configuration of the adsorbed species. Furthermore, we find the anisotropy of the Fermi surface of β-$Bi_2Pd$is transferred to the YSR wavefunction, giving rise to states that extend over half the coherence length of the superconductor. From the analysis of the extended states we deduce properties of the band to which V couples and the scattering processes in which it is involved.

The results shown in this chapter emphasize the scattering nature of YSR states and the role of the band structure in the formation of YSR states. Furthermore, we establish an equivalent picture between conventional QPI and YSR-mediated Bogoliubov quasiparticle scattering.

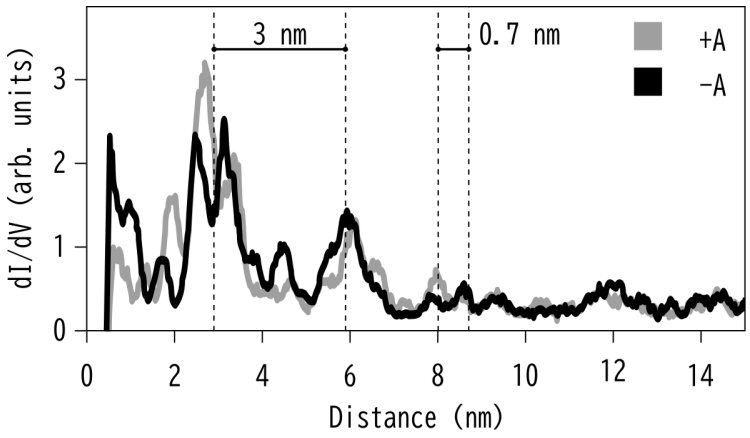

5.1 V deposition on β-Bi_2Pd

Vanadium was evaporated onto the cold ($\sim$ 14K) β-Bi_2Pd surface from a high purity (99.8%) rod while the sample was kept inside the STM head. Pristine V can be easily recognized as 140 pm-high randomly-distributed protrusions on the surface of the material. Besides pristine V, vanadium hydride molecules spontaneously form on the surface. They can be recognized as 80-pm high ring-shaped features that can be depleted of hydrogen scanning the area with a 1 V bias voltage. This chapter analyzes only the pristine species, leaving the identification and spectroscopic properties of hydrides for Chapter 7.

Fig.5.1 a) shows a large-scale STM image of the β-Bi_2Pdsurface with a disperse distribution of V adatoms appearing as orange spots. Such a small coverage is chosen so that most adatoms are far enough to be considered isolated from each other. No clusters are formed during deposition, suggesting that V loses its thermal energy fast upon landing on the surface. Fig.5.1 b) shows an atomically-resolved STM image of a pair of V adatoms and the underlying Bi square lattice. Combination of atomically-resolved images and lateral manipulation of the adatoms allows us to determine V adatoms adsorbe on the hollow site of the top-most Bi squared lattice, as shown in Fig.5.1 c). A height profile along an isolated V adatom shows the previously mentioned 140 pm height (Fig.5.1 d).

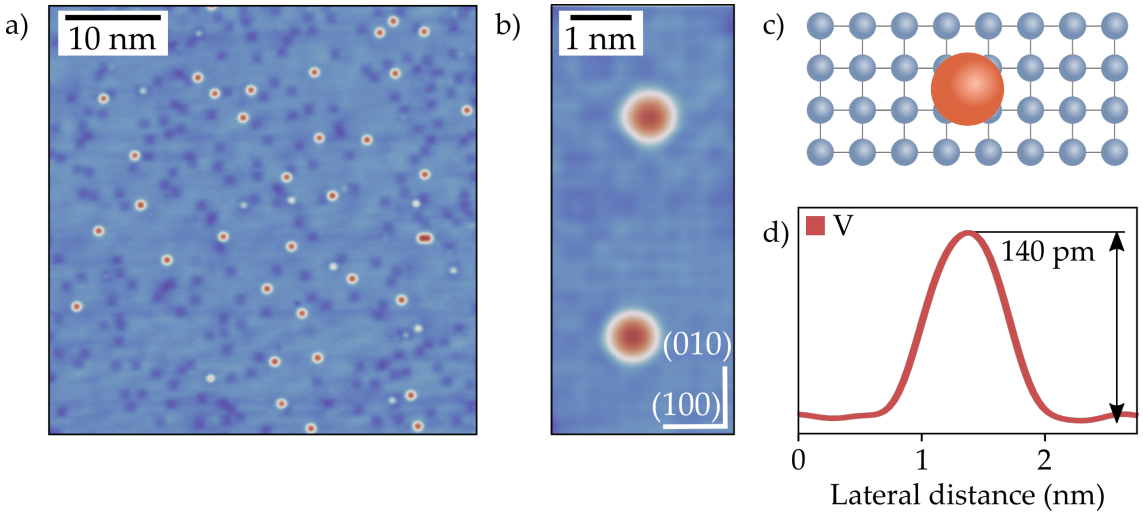

Figure 5.1: Evaporation of V. a) Sample coverage upon evaporation. Red spots correspond to V adatoms, white spots are Bi adatoms and square-shaped dark spots are vacancies. (V_{bias}=1 V, I_t=100 pA) **b** Atomic resolution of a 3x7 nm area showing two V adatoms and the underlying Bi lattice. (V_o=3 mV, I_o=1 nA) **c)** Depiction of V (orange) adsorption site on top of the square Bi (blue) lattice. **d)** Height profile on top of an isolated V adatom.

5.2 Excitation Spectra of V Adatoms

The excitation spectra of V adatoms shows a rich set of in-gap states associated to excitations of YSR states. Fig.5.2 a) shows a spectrum measured on an isolated V adatom using a β-Bi_2Pd tip. The spectrum shows 3 energy-symmetric pairs of peaks in the energy range between Δ_{tip} and $\Delta_{tip}+\Delta_{sample}$, labeled $\pm$A, $\pm$B and $\pm$C from lower to higher energy. Comparing the number of YSR states with the S=3/2 free-atom spin configuration of V ([Ar]$3d^3 4s^2$), we anticipate that each peaks corresponds to one of the half-occupied *d*-orbitals interacting with β-Bi_2Pd. This would confirm that V preserves its free-atom spin configuration when adsorbed on the surface of β-Bi_2Pd.

YSR states show a negative differential conductance (NDC) component that strongly depends on the spectrum acquisition site. To obtain a representative idea of the YSR state energies, we average over a set of 56x56 spectra measured in a 3x3-nm area around a V adatom (Fig.5.3 b). The YSR states can be directly identified in the averaged spectrum. We observe that, while peaks $\pm$C lie very close to the gap edge, peak $\pm$A is well defined around $\pm$1 meV, with a larger hole-like component.

The relative intensity of the electron and hole peaks also shows a strong dependence on the spectrum position on top of the atom, resembling effects observed in experiments with other transition metals in Pb.[14,15] In Fig.5.3 b), we show the spatial distribution of peak energies along the (100) crystallographic direction in a set of stacked spectra measured along a line on top of the V adatom. All peak intensities show a minimum at the center of the atom. There are no additional peaks at any other site around the adatom. NDC slightly shifts the energy of peak A to lower values in the vicinity of the atom.

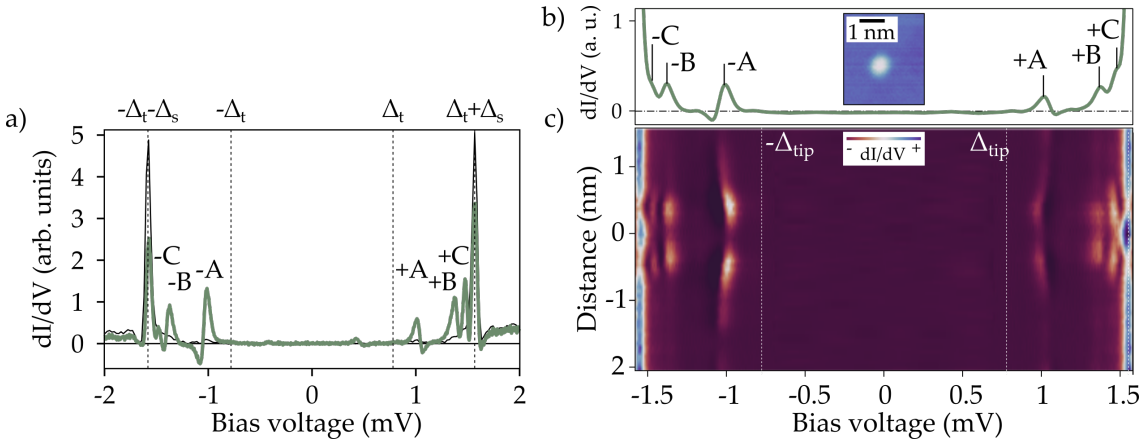

Figure 5.2: YSR excitation spectra of V. a) Spectrum measured on an isolated V adatom, showing 3 YSR states labeled $\pm$A, $\pm$B and $\pm$C. $\Delta_t=\Delta_{tip}$, $\Delta_s=\Delta_{sample}$(V_o=-3 mV, I_o=300 pA, V_{RMS}=25 μV) **b)** Averaged dI/dV over a 56x56 set of spectra measured in the area shown in the inset. (V_o=-3 mV, I_o=300 pA, V_{RMS}=25 μV). **c)** Set of stacked spectra measured along the (100) crystallographic direction showing the spatial distribution of peak energies. The atom is centered at 0.

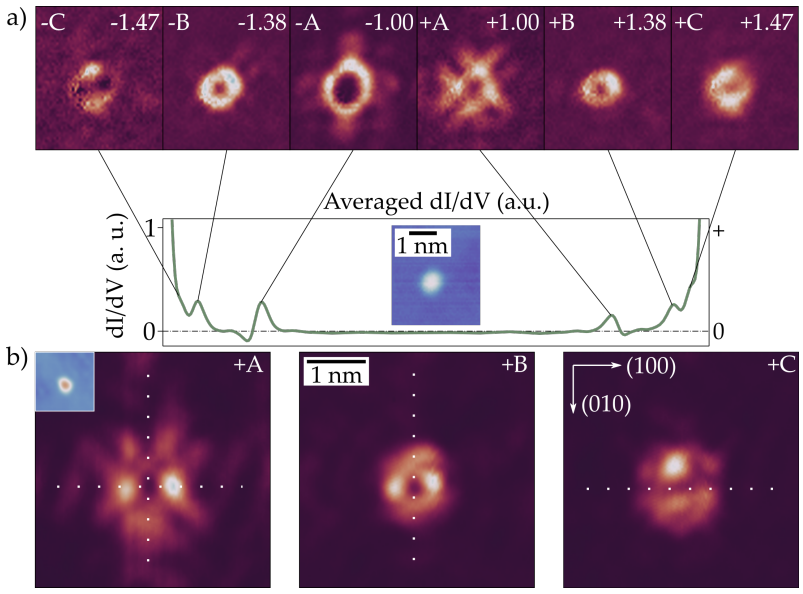

Figure 5.3: Spatial distribution of YSR states a) Conductance maps at the energies of each YSR excitation. Extracted from a 56x56 set of spectra measured in the 3x3-nm area in the blue image. **b)** Dual-pass dI/dV maps on a different atom with a different microscopic tip. Pointed lines indicate the symmetry axis in each map. (V_{bias}=-3 mV, I_t=300 pA V_{RMS}=50 μV).

Orbital Origin of YSR States

To understand the origin of the spatial distribution of peak intensities, we analyze the spatial distribution of each peak around the atom. Fig.5.3 a) shows constant-energy cuts extracted from a 56x56 set of spectra measured around a V adatom. We find a complex spatial distribution of quasiparticles around the atom, in contrast with the featureless topography of the atom. In view of this observation, we confirm the *d*-orbital origin of each peak.[14,15]

In Fig.5.3 b), we show dual-pass dI/dV maps acquired in a different isolated adatom and with a different tip, where nodal planes can be identified for each peak and states extending away from the atom appear in peak A. Following the procedure by Ruby *et al.*,[14] V adsorbed in the hollow site is in a square-pyramidal configuration (ML5 in [82]). In the ideal case, this ligand-field induces the splitting of the *d* sub-shell into three levels: the $d_{x^2-y^2}$ orbital , the d_{z^2} orbital, and a 3-fold degenerate energy state composed of the d_π and d_{xy} orbitals.[82] It is reasonable to assume that the multiplet with lower energy will ideally accommodate the three electrons of the *d* sub-shell. Slight distortions of this symmetry might be responsible for a further splittings of this multiplet into three levels, adjusting the orbital structure to the adsorption site. In order to clearly elucidate the particular orbitals, simulations of the adsorbed system would be needed.

5.3 Extended YSR States

The spatial distribution of YSR state A showed the map had a significant contribution away from the impurity atom. To elucidate its origin, we measure the set of spectra along the (100) direction shown in Fig.5.5 a). In the immediate vicinity of the adatom, at distances below 1 nm from the center, the intensity of the peaks is dominated by the shape of the orbitals from which they derive. Above that value, a modulated intensity extends over distances longer than half the coherence length of β-Bi_2Pd (ξ_{ab} = 23.2 nm)[51] and approximately equal to the mean-free-path of electrons in our samples (l = 15.3 nm).[50] The anomalously-large ratio between the coherence length and the YSR extension is only comparable to the one found for Fe dopants in bulk $NbSe_2$,[83] where the ratio was approximately one.[84] While in that case the effect was attributed to the 2D-character of the Fermi surface of $NbSe_2$, the 3D character of the Fermi surface of β-Bi_2Pd excludes this possibility. However, the presence of nesting vectors may result in an effective lower-dimensionality of the Fermi surface, thus enhancing the extension of the states.[14]

The modulated intensity of the YSR states shows two characteristic oscillation periods as shown in Fig.5.2 c), where a cut along the vertical axis of a) at the energies of the electron-like (+) and hole-like (-) components of peak A is plotted. Successive high-intensity peaks are separated by approximately 0.7 nm while subject to a second ∼3 nm-modulation. The presence of two modulations

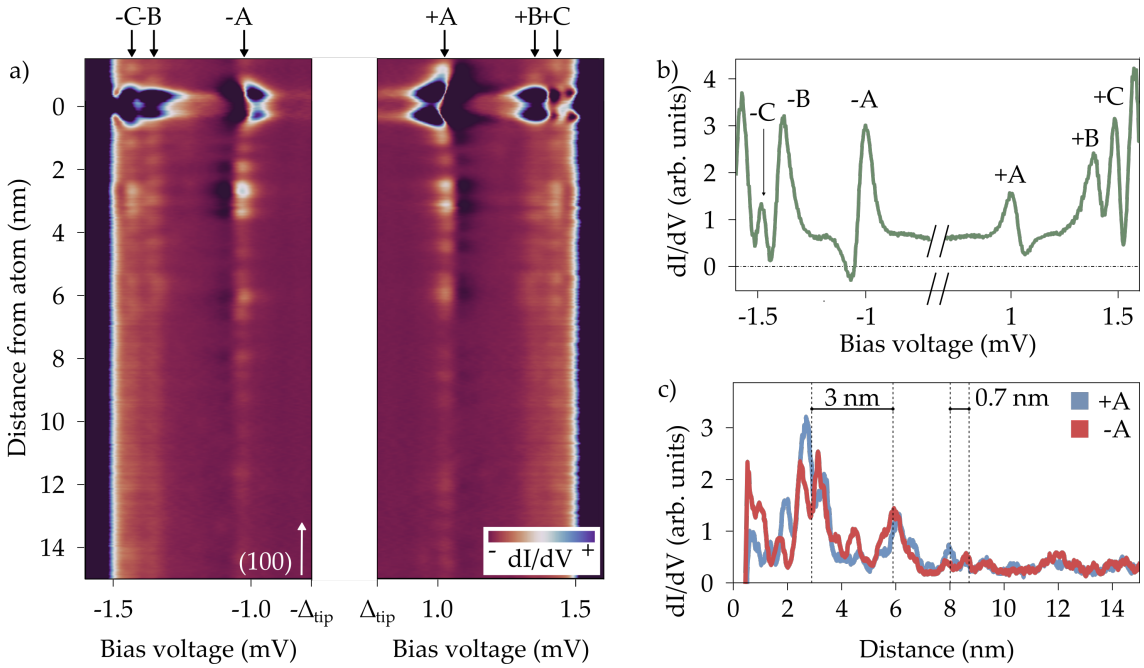

Figure 5.4: Extended YSR states. a) Series of stacked spectra measured along the (100) direction showing the spatial extent of the YSR wavefunctions associated to the different peaks. (V_o=-3 mV, I_o=300 pA, V_{RMS}=25 μV) **b)** A spectra from the set is shown for clarity. **c)** Constant-energy cuts of a) at the energy of peak ±A, showing the distance evolution of the modulations.

deviates from previous observations, where a single oscillation period was observed. A single-period modulated intensity of the electron and hole components of YSR states is well captured by the model described in section 1.3. Following the analogy with QPI in the metallic state, scattered Bogoliubov quasiparticles at the peak energy combine into new eigenstates with a wavevector defined by half the sum of the incoming and outgoing quasiparticles. In the case described by Rusinov, the superconductor consisted of a single electron band and thus the modulation is formed by (-$\mathbf{k}_F$, $\mathbf{k}_F$) pairs. β-Bi_2Pd presents a much richer band structure from which a more complex behavior arises.

To confirm our hypothesis on the band-structure origin of the peculiarities observed in V YSR states, we explore the spatial dependence of the states. Conductance maps measured at the energies of the tail found for each peak are shown in Fig.5.5, showing a cross-shaped distribution of LDOS originating from V impurity sites. The states extend along the crystallographic directions of the crystal, reflecting nesting vectors along $\overline{\Gamma M}$ in the Fermi surface. The strong anisotropic character of the Fermi surface is thus imprinted in the wavefunction, reinforcing our previous proposition of Fermi surface anisotropy as the origin of the anomalously extended states.

Modulations of the YSR wavefunction around the impurity site dominate the conductance maps at every energy. In the highest-energy states, both directionality and periodicity are lost within a few nm from V adatoms. We interpret this as a finite-temperature effect, by means of which phonon-assisted excitations can promote quasiparticles in YSR states close to the gap edge into the continuum and viceversa.[85] The higher energy difference between peak A and the gap edge (523 μeV) makes it less prone to phonon-assisted band-mixing with the continuum than peaks B and C (190 μeV and 100 μeV, respectively). We hence focus from now on the analysis of the wavefunction of YSR state A.

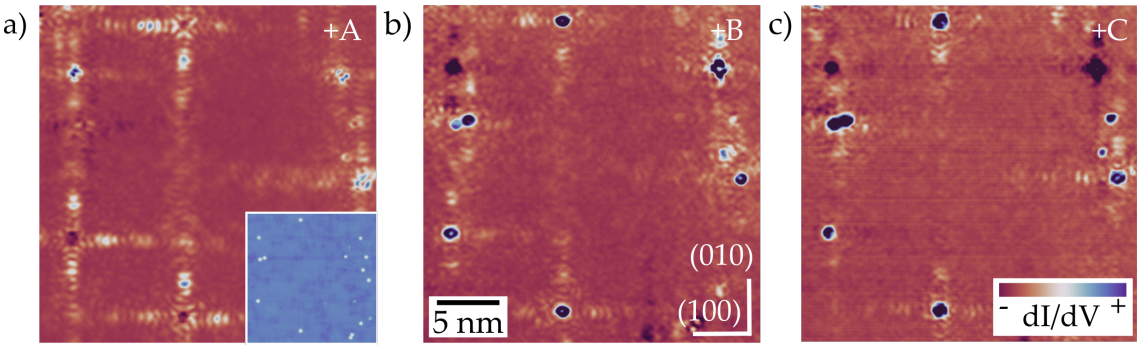

Figure 5.5: dI/dV at YSR peak energies. The maps show dual-pass maps acquired at the energies of the electron part of all YSR peaks found in V. The maps where acquired in the area show in the inset in a) over periods of approximately 4 hours per map. Note the scan direction is aligned with the crystallographic directions. (V_o=-3 mV, I_o=600 pA, V_{RMS}=50 μV)

5.4 Band Structure Effects in the YSR Wavefunction

The YSR wavefunction contains factors dependent on the Fermi surface both in the spatial decay of the state and in the Fermi wavevector of the bands of the superconductor.[7] However, in Rusinov's model the superconductor had a single band, in stark contrast with the 5 bands that cross the Fermi level in β-Bi_2Pd. In order to reconcile this picture with our measurement, we perform a similar analysis to the one used for conventional QPI to the Bogoliubov quasiparticle modulations that form the YSR state.

A freshly-cleaved sample is covered with a higher density of V adatoms and depleted of H in order to enhance the formation of QPI patterns. Fig.5.6 a) shows the resulting coverage in an 80x80 nm area. Fig.5.6 b) shows the simultaneously-acquired conductance map at the energy of peak +A, where extended YSR wavefunctions originate from V adatoms. The conductance map is Fourier-Transformed, generating the q-space map in Fig.5.6 c). Two concentric squares denoted q_A and q_B mark the wavevectors of Bogoliubov quasiparticles scattered by V adatoms. The accumulated intensity along $\overline{\Gamma M}$ is plotted in Fig.5.6 d), where the wavevectors appear as two peaks in an otherwise flat slope.

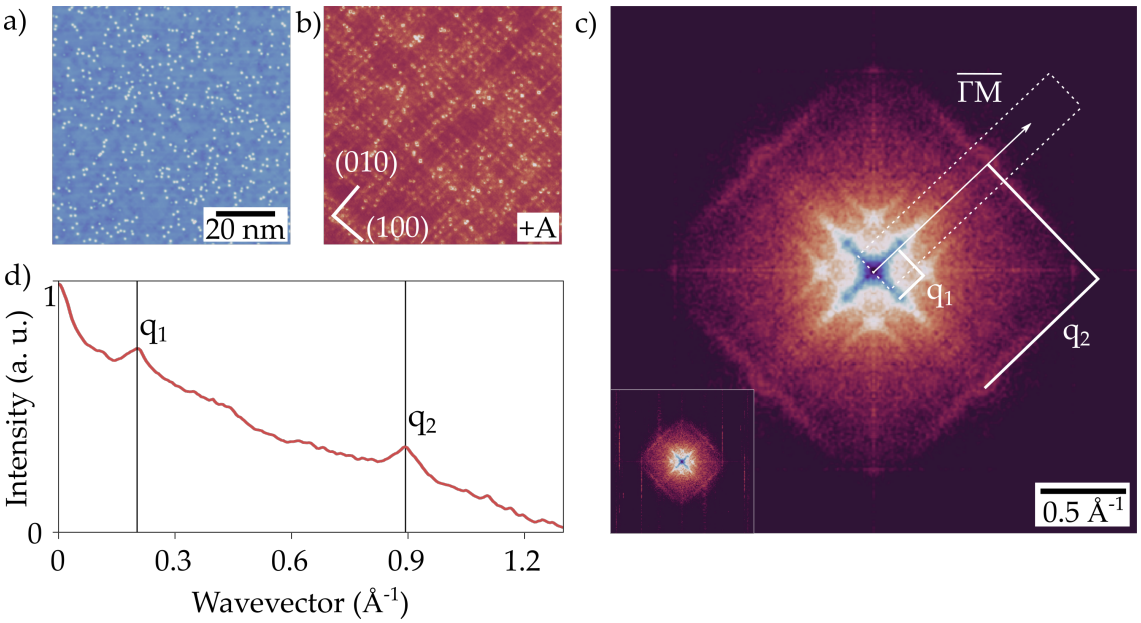

Figure 5.6: Scattering vectors identification. a) Topographic map of a densely-covered 80x80 nm area. (V_{bias}=-3 mV, I_t=300 pA) **b)** dI/dV map at the energy of peak A acquired in the area shown in a) using dual-pass. Approx. acquisition time: 6h. (V_o=-3 mV, I_o=300 pA, V_{RMS}=50 μV) **c)** 4-fold symmetrized 2D-Fast Fourier Transform of c). Each square corresponds to a different scattering vector. Inset shows the non-symmetrized FFT. **d)** Red: accumulated intensity in the area marked by a dotted square around the $\overline{\Gamma M}$ axis in c).

From the analysis of the FFT map, we confirm the modulations are caused by two distinct processes. The values of the scattering vectors are estimated from the curve in d) and found to be:

Vector	Wavevector [Å^{-1}]	Period [nm]
q_1	0.20±0.024	3.2
q_2	0.89±0.036	0.7

The oscillation period associated to the wavevectors is in great agreement with the periodicity estimated from the stacked spectra in Fig.5.2. However, given the complex band structure of β-Bi_2Pd, the presence of a single pair of well-defined scattering vectors is a strong indicator of a band-selectivity effect of the Bogoliubov quasiparticle scattering by magnetic impurities. To identify the origin of the modulations, we compare the wavevectors with the ones found in conventional QPI in the previous chapter:

Extracted scattering wavevectors from QPI patterns

Vector	Bands	Wavevector (Å^{-1})
q_A	S1 - α	0.117 ± 0.034
$\mathbf{q}_B$	S1 - S2	**0.196** ± 0.036
q_C	S2 - α	0.312 ± 0.030
q_D	α - β	0.503 ± 0.04
q_E	S1 - β	0.684 ± 0.025
$\mathbf{q}_F$	S2 - β	**0.895** ± 0.024

We find the two BQPI wavevectors q_1 and q_2 coincide with the vectors q_B and q_F found in QPI away from the superoconducting gap (+50 mV). Furthermore, we notice both q_B and q_F involve interband scattering processes, scattering between surface states S1 and S2, and scattering between surface state S2 and bulk band β. Several questions arise: i) why we dont observe intra band processes, as in previous results [14, 83], ii) why, instead, we see clear band mixing process in the YSR wavefunctions, and iii) why we observe only these two scattering wave vectors in a systems with many bands, while conventional QPI patterns reveal up to 6 of these inter band processes. To answer to these questions, we collaborated with Dr. Sebastian Bergeret and Dr. Julie Baumard, from the Materials Physics Center, in San Sebastian, and from Prof. Alfredo Levy-Yeyati and Miguel Alvarado, from the Institute of Condensed Matter Physics, at the Universidad Autónoma de Madrid, who performed theoretical simulations and modelling of BQPI patterns under several configurations of helical states. In the next section, we summarize the main findings and the interpretation of our results.

5.5 Spin-selective interference of Bogoliubov quasiparticles

The absence of intra-band processes is a consequence of the helical spin polarization of the bands in β-Bi_2Pd. The creation operator of Bogoliubov quasiparticles establishes a well-defined spin orientation for the electron and hole parts of the quasiparticles. In virtue of the well-defined spin numbers of these eigenstates, intra-band backscattering is forbidden for Bogoliubov quasiparticles in systems with helical bands. The effective models developed by Julie Baumard and Sebastian Bergeret confirm that, in a single-band superconductor with helical polarization, a bound state would still be generated by the magnetic impurity; nonetheless, Bogoliubov quasiparticles interacting with the impurity would not be able to constructively interfere and thus the state would be strictly localized in the magnetic potential. The absence of intra-band scattering in our measurements further confirms the absence of V-induced spin-flip events and the validity of the classical limit description of the magnetic interaction in YSR states.

In β-Bi_2Pd , the presence of several bands allows for the formation of an extended wavefunction even in the presence of a helical spin polarization. Although intra-band backscattering is forbidden, Bogoliubov quasiparticles can scatter between different bands as long as spin is preserved during the process. q_1 and q_2 reflect such processes taking place between quasiparticles derived from S1, S2 and β bands. These bands define three available scattering vectors among which only two contribute to the extended state (see Fig.5.7 a). The common denominator between the two scattering vectors is S2, hence coupling between V adatoms and β-$Bi_2Pd$is mediated by this surface state.

The long-range behavior of YSR modulations under these conditions can be simulated using the model by Rusinov under the assumption of a non-3D Fermi

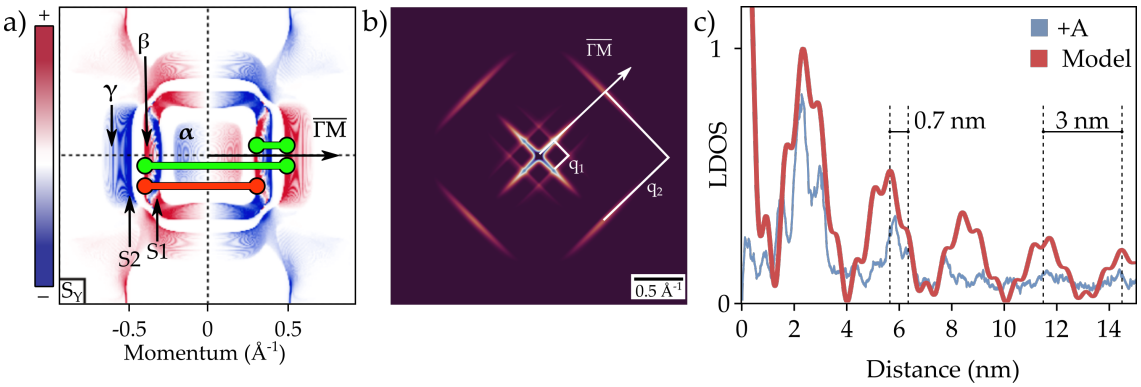

Figure 5.7: Inter-band scattering by YSR states. a) Calculated spin-polarization along the y axis of the bands at +30 mV. The different colors indicate the degree of polarization of the band at that energy. Green lines represent q_A (S1-S2) and q_B (S2-β). Red line represents S1-β scattering. Adapted from [58] .**b)** Calculated q-space intensity plot for S2-impurity coupling. White squares correspond to the experimentally-measured values in Fig5.6. **c)** YSR wavefunction modulation estimated from the scattering vectors in b) on top of experimental data.

surface.[83] Fig.5.7 shows the corresponding LDOS modulations in the electron component of the YSR state for an S2-coupled impurity with S2-S1 and S2-β scattering on top of the experimental results. The model captures the modulations found experimentally but fails to capture the decay rate. Ongoing tight-binding calculations by Miguel Alvarado and Alfredo Levi Yeyati are expected to capture this decay and effectively reproduce the 2D distribution of these states around the impurity.

5.6 Conclusions

We have studied the spectroscopic signatures of V adatoms on β-Bi_2Pd using superconducting β-Bi_2Pdtips, finding three YSR states caused by three half-occupied *d*-orbitals in V. In the region around the magnetic impurity, the YSR maps reproduced a set of nodal planes and symmetries that resemble the structure of *d*-orbitals. We speculated on the possible character of these orbitals from ligand theory arguments to conclude that each YSR subgap state corresponds to one orbital-mediated excitation channel.

From the analysis of the asymptotic behavior of the YSR wavefunction, we have been able to identify the band thorugh which V adatoms couple to β-Bi_2Pd. Furthermore, from this analysis we confirm that Bogoliubov quasiparticles have a well-defined spin and their scattering is spin-dependent. Our results corroborate the spin polarization of the surface bands of this material and, in particular, the presence of helical states. As previously pointed out by iwaya *et al.*[58], such unconventional spin texture of the surface bands is the basis for hosting mixed spin-singlet and triplet superconductivity, albeit, as hinted by the fully gapped superconductivity, probably singlet components from bulk bands dominate the superconducting behaviour of this material.

Results obtained in this section demonstrate that BQPI analysis can be used for the analysis of the superconducting state in materials with complex band structures. The band-selectivity found for V could be employed as a mechanism to probe individual bands in multiband superconductors and the absence of inter-band scattering from helical bands could be used as a signature of spin polarization, as it is nromally used for conventional QPI. Further experiments could be used to confirm the spin polarization of the extended wavefunction using spin-polarized tips.

Chapter Six

Magnetic Coupling and Chains of Magnetic Atoms

The interest in developing a system capable of producing Majorana-like states in a condensed matter experiment has motivated research on chains of magnetic atoms on top of superconductors during the last years. In order for these states to develop, the magnetic atoms need to be magnetically coupled, and thus precise control of atomic position and chemical identity are a must.

In this chapter, we study the YSR excitation spectrum of Mn adatoms on β-Bi_2Pd. We later use lateral manipulation to construct nanostructures and study the effects of coupling in Mn dimers as a first step towards the construction of atomic chains on β-Bi_2Pd. We find signatures of coupling in different configurations and study their feasibility as building blocks of Majorana chains. After the construction of dimers, we show two examples of magnetic chains in different configurations and analyze their excitation spectra.

The results obtained in the set of experiments described in this chapter emphasize the role of magnetic coupling in the formation of Majorana modes in chains of superconductors and can be used as a starting point for the evaluation of possible candidates to construct such systems.

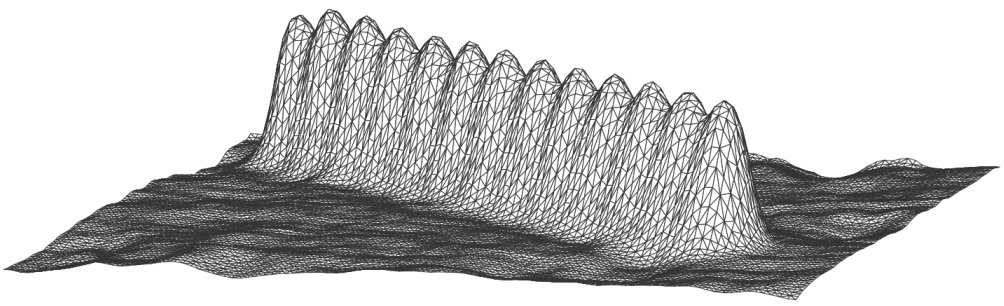

6.1 YSR Wavefunction Hybridization

YSR states are the result of the attractive interaction exerted by the impurity spin on the quasiparticles in the superconductor. This attractive interaction creates a bound state for quasiparticles that subsequently interfere and form the YSR wavefunction. The original formulation of the spatial extent of YSR states developed by Rusinov showed that the wavefunction of these states might extend over several atomic units.[7] One of the questions addressed by Rusinov was the effect of wavefunction overlapping on the excitation spectra of two nearby YSR states. He considered antiferromagnetic (AFM) and ferromagnetic (FM) alignment between the impurities. For the AFM case, the excitation spectra showed no substantial deviation from the single-impurity case. For FM alignment, he found YSR states split into two different states. In Fig.6.1 a) we depict a schematic representation of the two cases.

To understand the differences between the two cases, it is essential to remember that YSR states have a well-defined spin aligned parallel to the impurity spin. YSR states from two antiferromagnetically-aligned impurities have antiparallel spins. Their wavefunctions are then orthogonal, which prevents their hybridization. As a result, the states remain degenerate. YSR states from FM-aligned impurities, on the other hand, share the same spin state. In that case, overlapping of their wavefunctions gives rise to even an odd states with different energies, following:

$$|e^-,\uparrow\rangle_{e,o} = |e_1^-,\uparrow\rangle \pm |e_2^-,\uparrow\rangle \tag{6.1}$$

where $|e^-,\downarrow\rangle_{e,o}$ is the electron component of the even/odd wavefunction and $|e_i^-,\downarrow\rangle$ are the electron components of the YSR state of the non-interacting impurities.

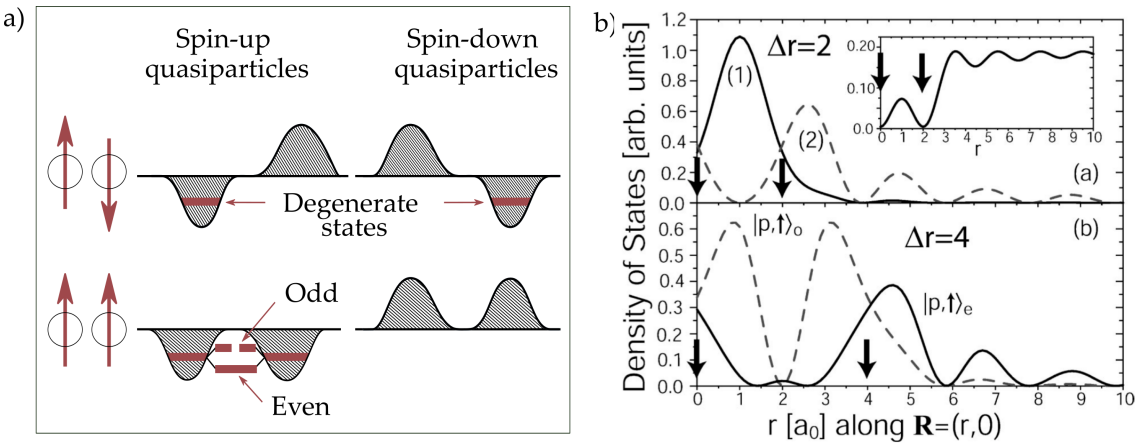

Figure 6.1: Formation of bound states in YSR dimers. a) Schematic representation of attractive and repulsive interaction in AFM (top) and FM (bottom) dimer. Adapted from [86] . **b)** Energy splitting in a FM-aligned dimer as a function of the distance between impurities. Reproduced from[87].

Splitting results from the overlapping of the YSR state in each impurity, and hence the distance between impurities plays an important role in the formation of even and odd states. Fig.6.1 b) shows the even an odd states for a pair of FM-aligned impurities at different impurity distances. In the first case, the superposition of waves results in the formation of bonding and anti-bonding-like states. In the second, even and odd states share a similar spatial distribution.

The energy difference between even an odd states, E_s, was directly obtained in Rusinov's formulation:

$$E_s = \epsilon_0 \left[1 + \frac{1}{4} \frac{sin(k_F R)}{k_F R} e^{-(R/\xi) sin(2\delta)} \right] \tag{6.2}$$

where ϵ_0 is the energy of the YSR state for isolated impurities, k_F is Fermi wavevector of the band to which the impurity couples, R is the distance between impurities, ξ the coherence length of the superconductor and δ is the scattering phase as defined in Eq.1.17. In Fig.6.2 a) we plot E_s as a function of the distance between impurities using approximate parameters for one of the bands in β-Bi_2Pd. For some distances, splitting is absent. For those cases in which E_s is not zero, splitting results in the spectroscopic signal shown in Fig.6.2 b).

From the previous examples, it is clear that the distance between impurities plays a vital role in the overall shape of the resulting states. This is not the only role of distance on the formation of the state, as the relative alignment between the two impurities is also dependent on how separated they are. FM or AFM coupling between not-adjacent impurities in metals follows from RKKY interaction. This kind of coupling strongly depends on the distance between impurities and k_F. In superconductors, a modified RKKY modulates AFM or FM behavior together with a YSR-mediated AFM interaction.[88] The latter dominates on long distances, so FM coupling usually requires close-by impurities.

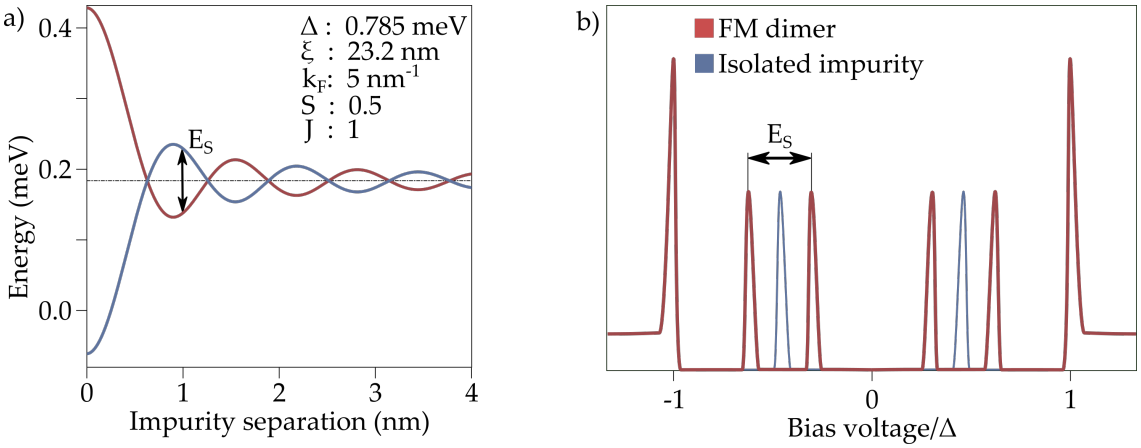

Figure 6.2: Energy splitting in FM dimers. a) Energy splitting as a function of the distance between impurities as calculated from Eq.6.2. The parameters are included in the figure. **b)** Schematic representation of peak splitting in a spectroscopic measurement.

6.2 YSR States from Mn

In preparation for the evaluation of Manganese as a potential candidate for the construction of chains, Mn adatoms were evaporated from a Mo crucible while the sample temperature was kept below 14 K to avoid thermally-activated diffusion. After deposition, Mn adatoms appear on the surface of β-Bi_2Pd as unevenly-distributed 140 pm protrusions, as shown in Fig.6.3 a), where they coexist with the intrinsic defects found in β-Bi_2Pd crystals. Mn and intrinsic Bi impurities can be directly distinguished by their different apparent height and the absence of spectroscopic features in the latter. Lateral manipulation showed that Mn atoms lie on the hollow site of the lattice, surrounded by four Bi atoms to which they are weakly coupled. This adsorption configuration is in agreement with the one found for similar atoms on the same material.[16] A detailed examination of topographic maps shows a single species forms after deposition, in contrast with the formation of hydrides found during deposition of Vanadium under similar conditions.

Spectroscopy using β-Bi_2Pd-coated tips reveals the presence of a single excitation inside the superconducting gap, appearing at different energies in different atoms (Fig.6.3 b). An extensive analysis performed over a set of 103 atoms using the same microscopic tip reveals a broad distribution of excitation energies in the range between ~1.15 and 1.38 mV. The energies of the peaks where obtained from a fit of the electron and hole components to a Lorentzian curve. In Fig.6.3 c) the energies of the excitation in the different adatoms are shown in a scatter plot, where the X and Y values of each point are given by the energy of the electron and hole components of the state, respectively. The vast majority of points lie within the energy-symmetric area defined by a dashed line, with some of the spectra showing slightly different energies for the electron and hole components.

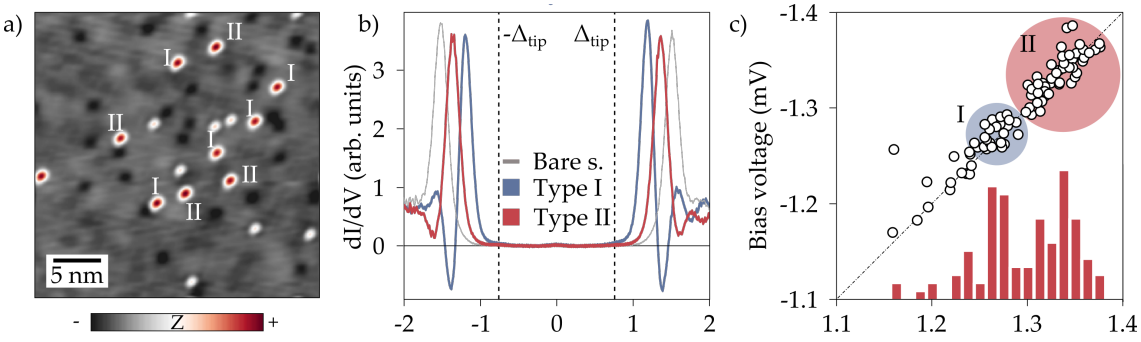

Figure 6.3: Excitation spectra of Mn on β-Bi_2Pd. **a)** Topography map showing Mn adatoms (red), Bi impurities (white) and vacancies (dark squares). I and II indicate the type of atom by their excitation spectra (V_{bias}=1V, I_t=10 pA) **b)** YSR excitations of Mn atoms from both groups, showing a YSR excitation as a peak at different energies (V_o=3 mV, I_o=300 pA, V_{RMS}=100 μV). **c)** Distribution of peak energies extracted from 103 spectra measured on a 80x80 nm area with the same microscopic tip. A dashed line indicates the energy-symmetric values. An histogram below shows the accumulated number of peaks in the positive side of the spectra in 0.125μV bins. Blue and red circles indicate the extent categories I and II.

An histogram in the bottom part of Fig.6.3 c) groups the observed energies in 0.125-mV bins, where the energies tend to accumulate into two groups around 1.27 mV and 1.34 mV (labeled I and II). A visual comparison of individual spectra shows that the excitations in atoms of the first group have a negative differential conductance(NDC) component (dips below zero conductance next to the peaks), absent in atoms of the second kind. NDC is a well-known artifact associated to the convolution of sharp delta-like features with the DOS of superconducting tips. Ruby and coworkers related the presence of NDC to the tunneling strength, showing that a transition from the linear to the sub-linear tunneling regime results in the disappearance of NDC.[85] In our case all the spectra were measured under the same conditions, what excludes the possibility of being caused by differing tunneling strengths. A possible explanation for the the presence of NDC in only one of the groups would be a different peak width. As we said before, NDC results from the convolution of sharp delta-like features with the DOS of the tip. As a consequence, an increased resonance width fades the negative conductance contribution from the tip derivative. In view of this, we tentatively attribute the NDC in type I atoms to a smaller excitation width.

Turning back to the number of excitations of Mn on β-Bi_2Pd, we note the presence of a single excitation is in stark contrast with the $[Ar]3d^54s^2$ electronic configuration of the transition metal, from which a S=5/2 in the free-gas state configuration derives. Paramagnetic impurities with more than one non-degenerate half-occupied *d*-orbital are known to induce a YSR state per half-occupied localized orbital.[14,15] As we showed in Chapter 5, each non-degenerate orbital acts as an independent quasiparticle scatterer, reflecting the symmetries of the orbital in the spatial distribution of the YSR wavefunction. This is not the case for Mn, where YSR states appear homogeneously distributed over the surface of the atom and peak intensity vanishes at the atom edges. Several effects could cause this behavior. First of all, Mn may lose its S=5/2 character when deposited on the surface. Still, assuming an S=1/2 configuration, the YSR wavefunction should show a characteristic spatial distribution associated to the remaining half-occupied *d*-orbital that is absent in our measurements. A second possibility would involve the presence of several degenerate YSR states at close energies. In this case, the integrated contribution from 5 degenerate *d*-orbitals sums up into a spherical shape,[89] in agreement with the spatial distribution of the observed YSR state.

Additional signatures of multiple degenerate *d*-orbitals come from the observation of extra peaks at different energies in a small subset of Mn atoms of the second kind measured with higher-resolution tips. In Fig.6.4 we show these additional excitations as measured in the adatoms indicated in b). In atom A, the additional excitation γ appears almost at the energy of the coherence peaks. However, the peaks show an asymmetry not shared by the main excitation β, thus indicating that it corresponds to a YSR excitation. In atom B the additional excitation α appears at energies below β. In c) we show the spatial distribution of peaks α and β , where they appear strictly localized inside the atom. Additional in-gap states may appear as a result of vibrational modes[90] or magnetic anisotropy[91]. Spectroscopy at higher bias values shows no signatures of vibra-

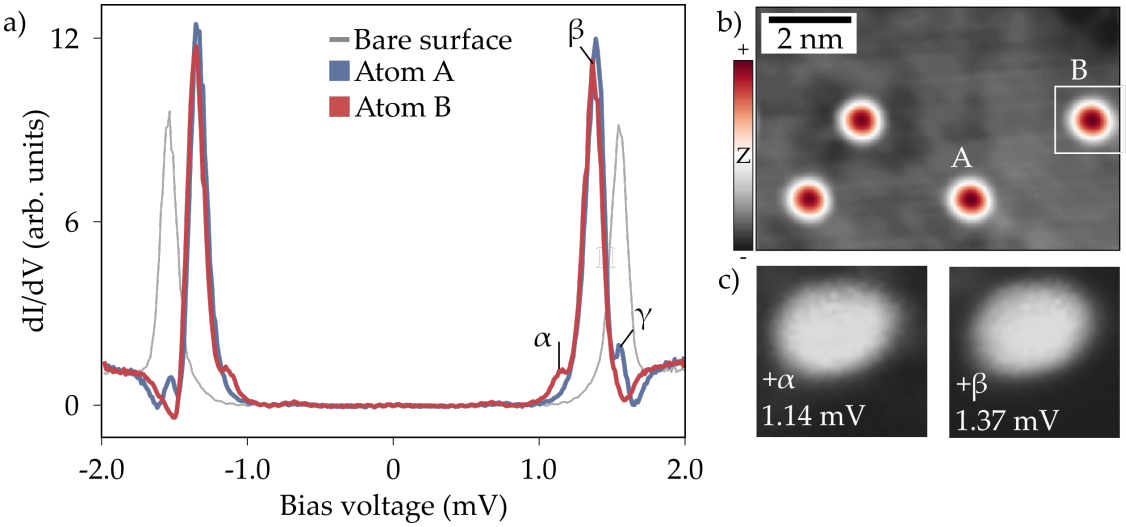

Figure 6.4: Detail of a second excitation. a) Comparison of the excitation spectra of two Mn adatoms showing the main YSR state (β) and an additional excitation at different energies (α, γ). (V_o=3 mV, I_o=300 pA, V_{RMS}=50 μV). **b)** Topographic map showing the area where the spectra were measured. A white square indicates the approximate measurement area in c) (V_{bias}=3 mV, I_t=35 pA). **c)** Spatial distribution of peaks α and β as extracted from a 32x32 pixel grid (V_o=3 mV, I_o=1 nA, V_{RMS}=100 μV).

tional or spin excitations, implying that half-occupied near-degenerate *d*-orbitals must cause the additional peaks.

We work on the assumption that Mn preserves its S=5/2 after deposition and that changes in the relative energies of the different states cause the broad distribution of peak energies. In Fig.6.5 we show a fit of the experimental spectra to a phenomenological 5-nearly-degenerate-orbitals model. We model YSR states as lorentzian peaks with varying intensities and the resulting model is convoluted with the tip DOS and thermally broadened using the Fermi-Dirac distribution. We calculate the DOS of the tip and the equivalent temperature of the measurement from fits to spectra measured on the bare surface (see d). (a) and (b) correspond to type II atoms measured with high-resolution tips and (c) to a type I Mn adatom. The model effectively captures the spectral linewidths and peak symmetries. Particularly, we find a single orbital model does not reproduce the NDC dips, providing indirect confirmation of the presence of several peaks. The model also captures the asymmetries found in the electron and hole components in some of the adatoms. Impurities and defects would cause changes in the relative intensities of the peaks on the crystal or slight variations in the adsoprtion configuration. Confirmation of the electronic configuration of Mn adatoms on β-Bi_2Pd and this hypothesis would require Density-Functional Theory calculations.

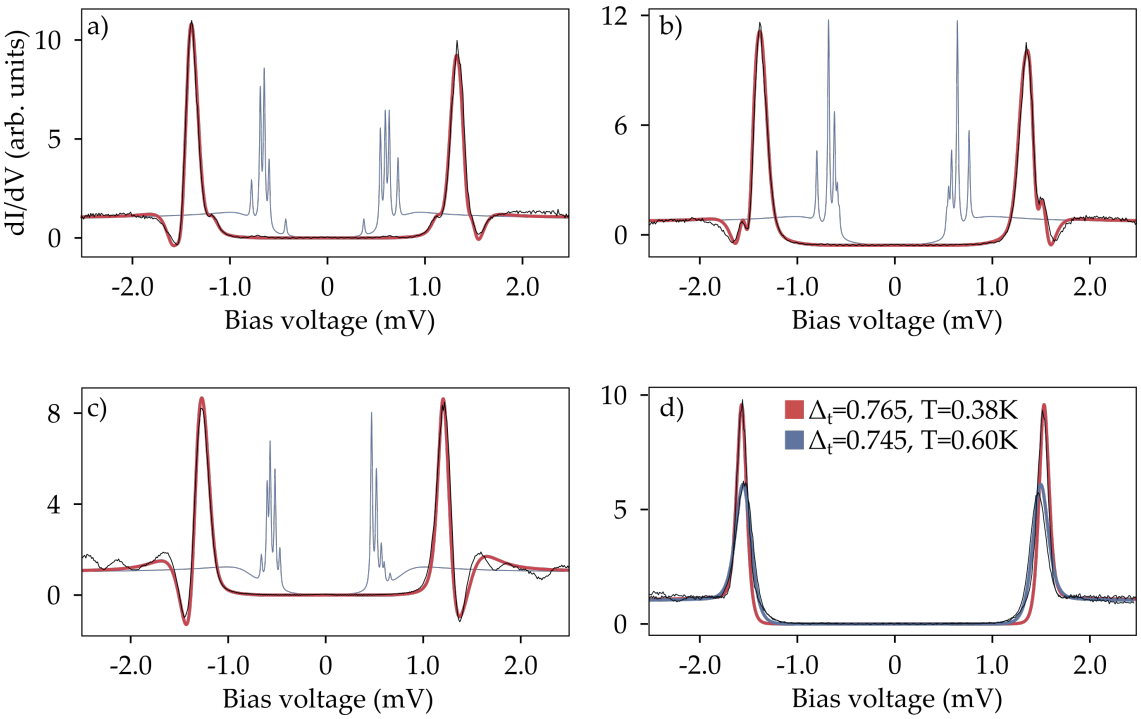

Figure 6.5: Phenomenological 5-orbital model. a) Fit of the excitation spectra of a type-II Mn adatom using the parameters of the red curve in d). **b)** Fit of the excitation spectra of a type-II Mn adatom using using the parameters of the red curve in d). **c)** Fit of the excitation spectra of a type-I Mn adatom using the parameters of the blue curve in d).**d)** Fit of spectra on the bare surface using the tips in a), b), and c). The parameters of the fit are shown on top.

6.3 *Magnetic Coupling in dimers*

As a previous step to the construction of chains, we used lateral manipulation to assemble Mn dimers in different configurations. The use of lateral manipulation results crucial at this stage, as it provides essential information about the stability of the dimer and confirms the chemical identity of the constituent atoms. In this section, we identify the characteristic excitations of the different configurations and find signatures of different degrees of magnetic coupling. At the end of this chapter, we present additional results on V and Fe dimers as examples of ferromagnetic coupling.

Lateral Manipulation of Mn Adatoms

Lateral manipulation of Mn adatoms was found to be completely reproducible using Mn-coated β-Bi_2Pd tips and junction resistances of $\sim$300 kΩ. In Fig.6.6 we show a typical manipulation curve. The tip is held at a constant current setpoint while moved laterally at 300 pm/s. When the tip approaches the atom, Mn is attracted to the tip and jumps into the next hollow site. Then the tip passes above the atom and Mn follows the trajectory of the tip until the desired position is reached. The curve corresponds to the pulling type of lateral manipulation.[92]

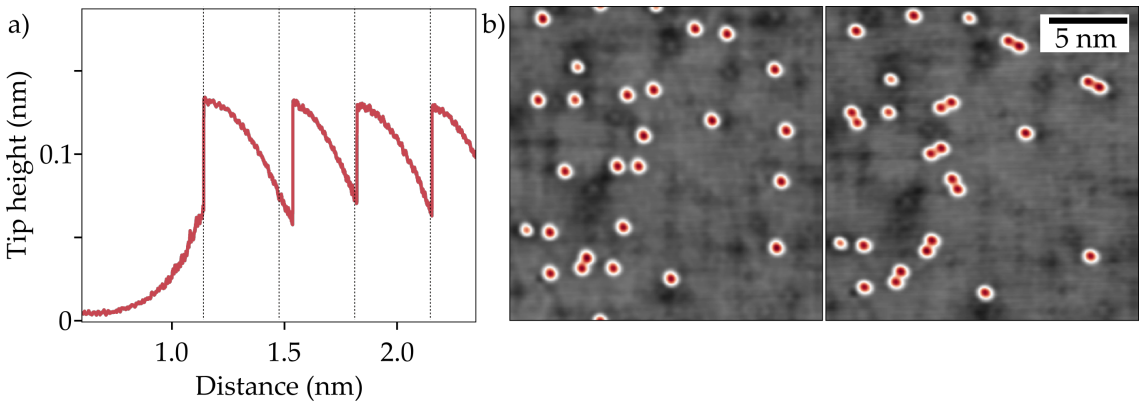

Figure 6.6: Lateral manipulation of Mn adatoms. a) Tip position recorded during lateral manipulation. Adatom displacements appear as abrupt changes in tip height. Dashed lines represent 0.336 Å steps. **b)** Controlled manipulation of Mn adatoms.

The chemical composition of the tip plays an important role in the manipulation of Mn adatoms. Bare β-Bi_2Pd tips were less reliable than Mn-coated ones, with manipulation attempts usually resulting in the adatom becoming attached to the tip apex. After several Mn adatoms are attached to the tip, stable manipulation is achieved. There is a downside of this coating procedure: superconducting tips that provide stable manipulation cannot be used for spectroscopic measurements because YSR states form in the tip apex[93] and thus the tip needs to be prepared again after manipulation. This prevents the use of superconducting tips for the analysis of the atom-by-atom evolution of YSR states in chains, limiting the energy resolution of such measurements.

AFM Coupling at 1 Atomic Distance

The minimum inter-impurity distance allowed by the square lattice of β-Bi_2Pd for atoms sitting in the hollow site corresponds to one atomic distance (1,0), where Mn adatoms are separated by 3.36 Å. Fig.6.7 a) shows a dimer constructed by placing two atoms in this configuration. The dimer, on the left, appears as an elongated structure where the constituent atoms cannot be individually resolved, a usual behavior in closed-packed dimers. A comparison with a nearby Mn adatom shows that the apparent height of Mn is preserved in the dimer. Spectroscopy on the dimer shows a peak at the approximate energy of the substrate coherence peaks (Fig.6.7 b) regardless of the tip position on the dimer. This behavior is interpreted as the result of AFM coupling. In this configuration the total magnetic moment of the dimer is zero, an expected configuration for Mn_2 molecules[94,95] that has also been observed in closed-packed Mn structures with even number of atoms on thin insulating layers.[96,97] A similar AFM behavior was observed for Cr dimers on β-Bi_2Pd in this configuration.[16] One would expect then the peak to completely submerge into the continuum, but the potential scattering term in non-paramagnetic impurities still induces YSR states very close to Δ,[98,99] what accounts for the slightly different spectrum found on the bare surface and the dimer.

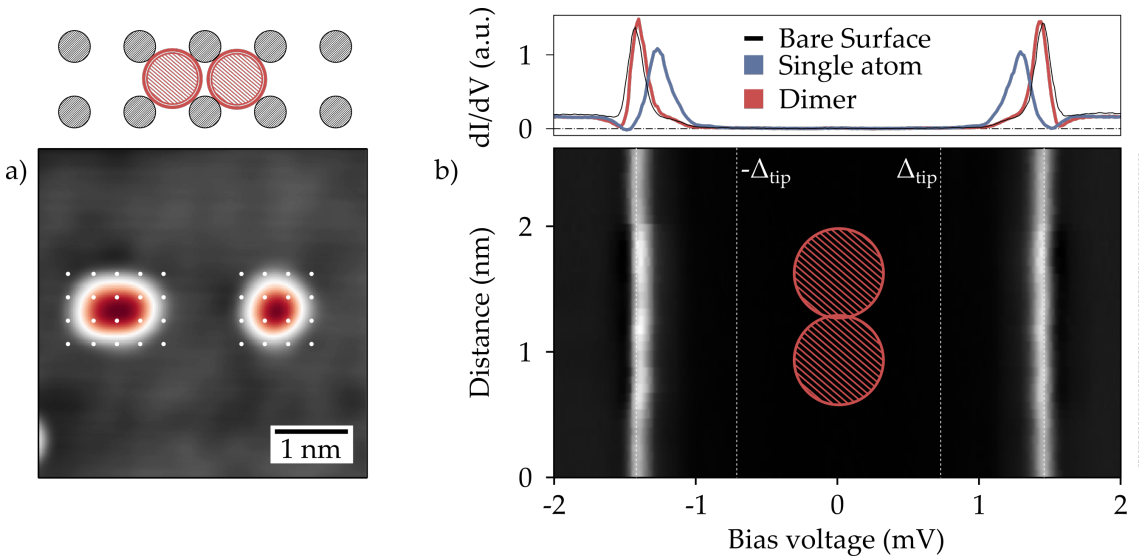

Figure 6.7: Antiferromagnetic coupling at 3.36 Å. a) Mn dimer in the (1,0) configuration appears as an elongated structure with the apparent height of isolated adatoms. A Mn adatom is shown on the right side for comparison. Dots indicate the approximate position of Bi atoms underneath. (V_{bias}=3 mV, I_t=300 pA). **b)** Top: Comparison of the excitation spectra of a dimer and an isolated Mn adatom. Bottom: Stacked set of spectra measured along a line centered in the dimer. The approximate position on the dimer is indicated in the center. (V_o=3 mV, I_o=300 pA, V_{RMS}=25 μV).

AFM chains are potential candidates for the formation of topological chains, although SOC and an external in-plane external Zeeman field are required in order for Majorana modes to develop in these systems.[100] Besides Majorana physics, this type of coupling presents interesting even-odd number effects[96,101] that could unveil new information about the effect of superconductivity on the intrinsic properties of magnetic structures. Unfortunately, we found Mn adatoms in this configuration are not the best candidates for the construction of such systems. Although the formation of a dimer probed to be reliable and easy to achieve, the resulting structures were extremely unstable against the addition of a third atom. In Fig.6.8 a) we show the formation of a triangular cluster upon the addition of a third atom. This observation seemed to contradict the apparent stability of the dimer.

In order to understand the origin of the instability, we compare our observation with the behavior of similar Cr dimers on β-Bi_2Pd.[16] In that case, adatoms separated by one atomic distance get attracted to each other, resulting in displacement from the hollow adsorption site and the displacement of Bi atoms below. We propose the same behavior takes place with Mn. In our case, when the third Mn adatom reaches the hollow site, it finds a perturbed lattice and is attracted to the nearby Mn, making the whole configuration unstable. Although this instability impedes the formation of uniform magnetic chains, enhanced lateral precision could potentially allow for the construction of Peierls-like dimerized chains.

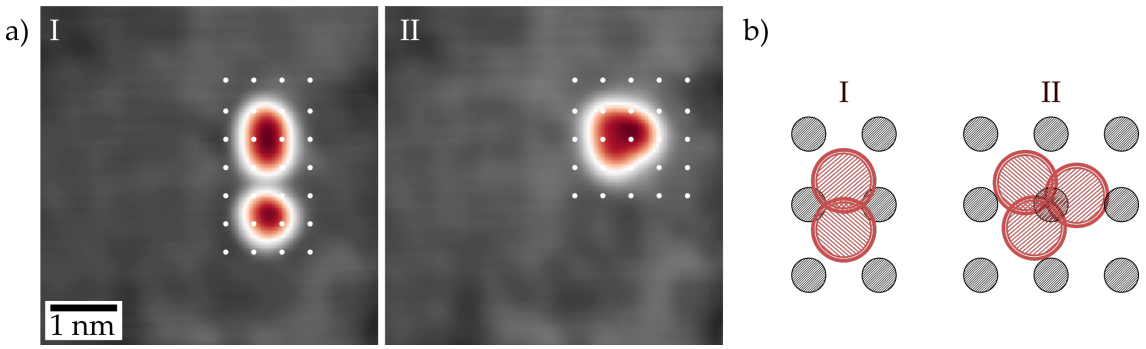

Figure 6.8: Formation of clusters upon addition of a third atom. a) Topographic maps showing the construction of a dimer and the system after attempting to add a third atom (V_{bias}=1 V, I_t=10 pA). **b)** Proposed model of atomic positions in a).

AFM Coupling in the $\sqrt{2}$ Configuration

Moving on to the next available inter-atomic distance, we construct Mn dimers in the (1,1) (or $\sqrt{2}$) configuration, where the adatoms are separated by 4.75 Å (Fig.6.9 a). This distance is within the range of different magnetic interactions (namely superexchange, RKKY, and YSR-mediated AFM coupling), making it a strong candidate for the construction of chains. Unfortunately, this type of dimer proved to be extremely unstable, requiring one of the constituent atoms to be placed next to an intrinsic Bi impurity in order to prevent the formation of a cluster during manipulation. In chapter 4, we discussed the origin and the position of Bi impurities in the lattice. As Bi impurities adhere to vacancy sites, the lattice underneath is in a perturbed configuration, which probably contributes to the stabilization of Mn adatoms in their vicinity.

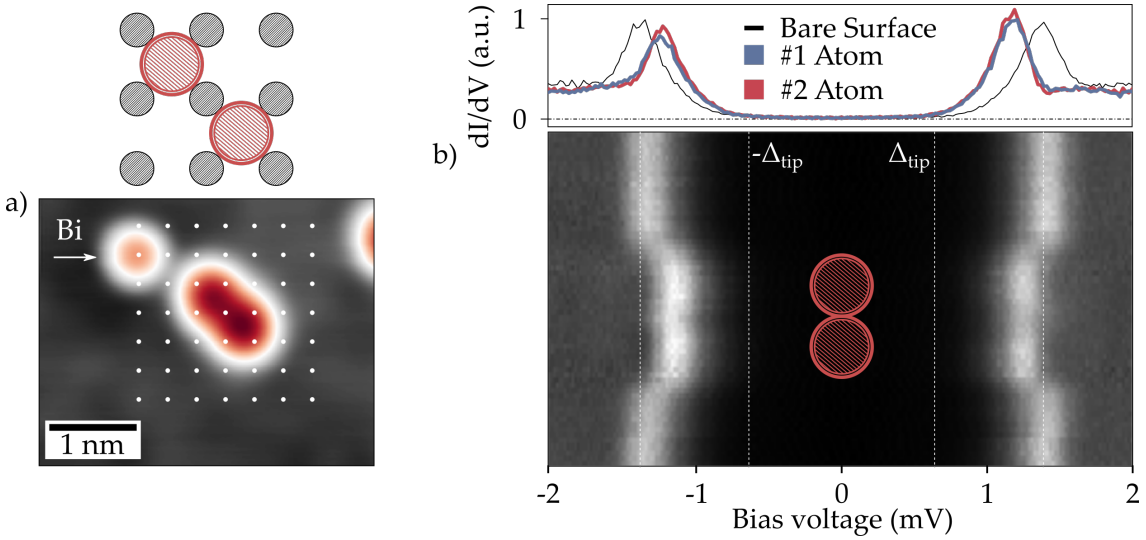

Figure 6.9: Spectroscopic characteristics of a constructed $\sqrt{2}$ dimer. a) Topographic map showing a dimer next to a substitutional impurity (V_{bias}=100 mV, I_t=10 pA). **b)** Top: excitation spectra of each one of the constituent atoms. Bottom: series of stacked spectra taken along the white line shown in a) (V_o=3 mV, I_o=300 pA, V_{RMS}=50 μV).

Spectroscopy on the dimer shows the presence of a single YSR excitation at similar energies in both atoms (Fig.6.9 b). A slight decrease of peak intensity in the middle point of the dimer shows that the excitation is localized in the atoms. The presence of a single excitation and the fact that the excitation appears at the energies usually found for isolated impurities allows us to discard ferromagnetic coupling, in contrast with the ferromagnetic ordering found for Cr atoms in this configuration[16]. There is still a remarkable coincidence of peak energies in both adatoms, which is interpreted as a signature of antiferromagnetic coupling. Antiferromagnetically-coupled magnetic impurities have YSR states with opposite spin alignment, which forbids the wavefunction hybridization that causes bonding and anti-bonding states. As a result, the states are strongly localized on top of the impurities. The total magnetic moment of the dimer must be non-zero, in contrast to the full vanishing of the magnetic moment found in the (1,0) case.

To confirm the non-significance of the Bi impurity, we analyze dimers in this configuration formed during evaporation. Fig.6.10 shows one of those dimers. Spectra measured at equivalent positions on each one of the atoms shows they both share the same YSR excitation energy and peak asymmetry, consistent with what we saw in the presence of the intrinsic Bi impurity. This measurement was performed with a higher-resolution tip than the assembled dimer and confirmed no peak splitting is observed in this configuration. The mere existence of $\sqrt{2}$ dimers among the as-deposited adatoms proves there may be a way to construct dimers in this configuration using lateral manipulation. Still, while measuring a set of spectra on top of the atoms, the dimer collapsed, showing this dimer may have been in a metastable equilibrium position. Construction of longer chains requires complete control of atom positioning and stability of the constituents, a property not found in this case.

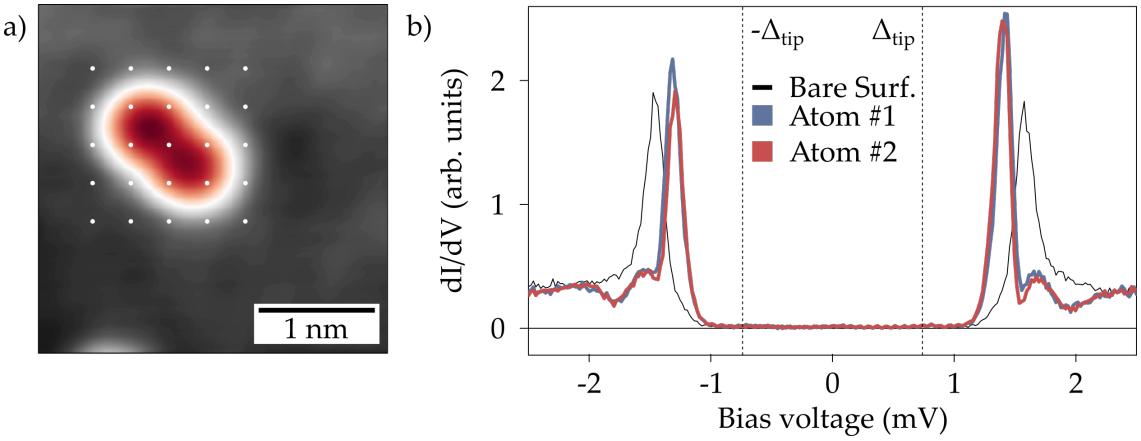

Figure 6.10: Spectroscopic characteristics on an as-deposited $\sqrt{2}$ dimer. a) Topographic map showing the dimer formed during deposition (V_{bias}=3 mV, I_t=300 pA). **b)** Excitation spectra of each one of the constituent atoms, showing both share the same excitation energy. (V_o=3 mV, I_o=300 pA, V_{RMS}=25 μV).

FM Coupling in the $\sqrt{5}$ Configuration

The last example of magnetic coupling found in Mn dimers corresponds to the (1,2) (or $\sqrt{5}$) configuration, with Mn adatoms separated by 7.51 Å. This type of dimer can be easily constructed due to the relatively large distance between the constituent atoms, which makes it a suitable option for the construction of chains. Fig.6.11 a) shows the construction of a dimer in this configuration by lateral manipulation of adatom 2 (1 is left unperturbed). The excitations of the constituent atoms before manipulation and of atom 1 after the dimer is formed are shown in b), where a significant change in the energy of the YSR states can be observed. Focusing first on atom 1, we see the energy of the state shift towards lower values, with the hole component shifting from -1.33 mV to 1.08. The adatom was not displaced from its original position during manipulation, suggesting the energy shift is due to an interaction with atom 2. The second atom shows different behavior. Before manipulation, the electron and hole components of the YSR excitation appeared at different energies, a behavior attributed to the presence of several almost-degenerate *d*-orbitals with different spectral weights on their electron and hole components. However, when the atom is brought to the proximity of atom 1 the excitation appears at symmetric energies, indicating that now most of the spectral weight has moved to a particular orbital in both the electron and hole components.

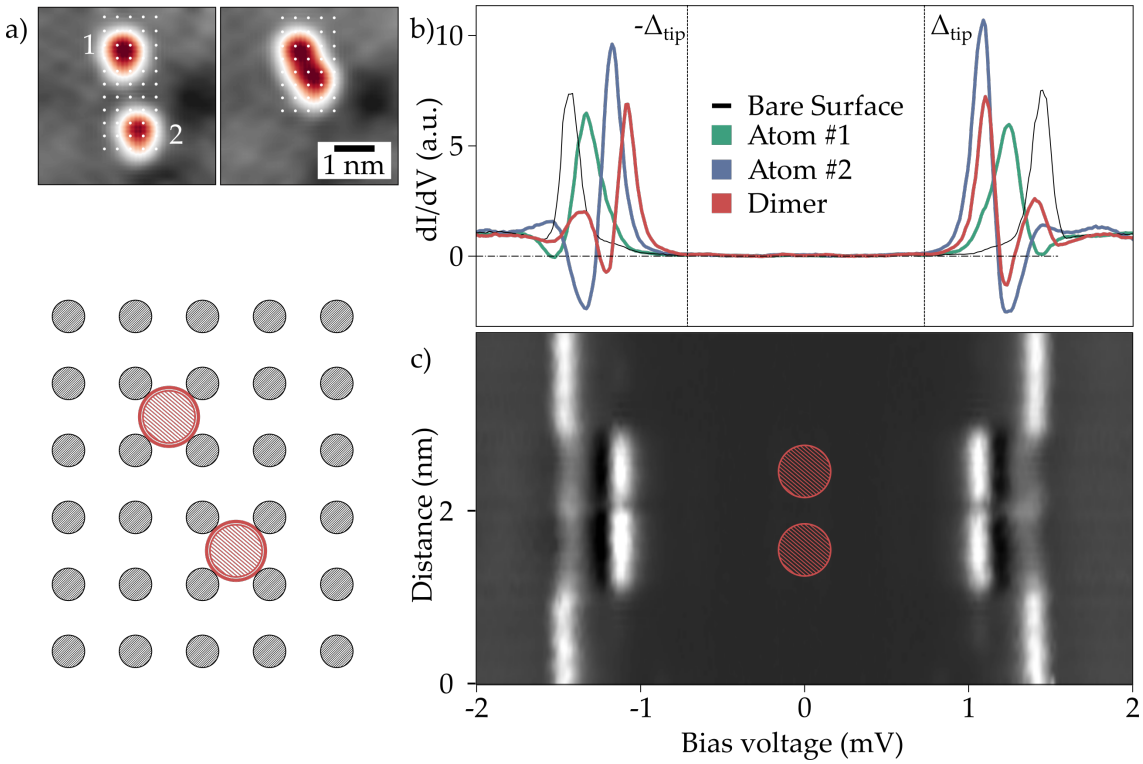

Figure 6.11: Ferromagnetic coupling at 7.51 Å. a) Mn dimer in the $\sqrt{5}$ configuration from the constituent (left) to the final product (right) (V_{bias}=1 V, I_t=10 pA). **b)** Excitation spectra of each one of the constituent atoms and the dimer. (V_o=3 mV, I_o=300 pA, V_{RMS}=50 μV). **c)** Stacked set of spectra measured on top of the dimer along the (1,2) direction.

In view of the apparent shift of the YSR states to lower energies and the symmetric energies of the electron and hole components, we tentatively attribute this effect to ferromagnetic coupling. In this case, the interaction between the adatoms would align the spin of both impurities in the same direction, leaving them in the same magnetic configuration and shifting their YSR energies to the same value. Peak splitting, absent in this dimer, is usually regarded as one of the signatures of FM coupling in magnetic dimers on superconductors. However, peak splitting results from the formation of even and odd states of overlapping YSR wavefunctions. In Mn, the YSRs wavefunction is strongly localized in the atom site, which prevents the formation of hybridized states at the actual inter-impurity distance. Additionally, the absence of extended YSR states allows us to discard YSR-mediated AFM coupling, and thus impurities must be coupled through RKKY interaction. Knowledge of whether RKKY results in FM or AFM at this distance, which would provide experimental verification of this hypothesis, cannot be directly inferred from our measurements. This leaves the confirmation of the FM sign of the interaction in these dimers as an open question for future experiments using either Spin-polarized STM at lower temperatures[102] or Radio-Frequency STM.[103]

6.4 Mn chains

In the last section, we showed the possible dimer configurations in which signatures of magnetic coupling could be observed. We have found that two atomic arrangements cannot be used for the construction of chains because they are unstable against the addition of a third adatom or because they correspond to unstable configurations. In this section, we construct chains in the remaining coupled configuration and evaluate a configuration that showed no clear sign of coupling in dimers: the (2,0) configuration.

Mn_9 Chain along the (100) Direction

The construction of a manganese chain along the crystallographic direction was motivated by the observation of the strong anisotropy of the Fermi surface of β-Bi_2Pd along $\overline{\Gamma M}$. Although no coupling was observed in dimers, we elucidated that, because of this anisotropy, RKKY interaction may extend more along the crystallographic directions[104–106] and, despite the absence of coupling in dimers, show effects at larger spacings. Furthermore, the complicated band structure of β-Bi_2Pd and the presence of intra and inter-band components make predictions about the long-range evolution of RKKY interaction complicated,[107] providing additional motivation for the evaluation of this configuration.

The assembled chain and the area around it are shown in Fig.6.12 a), with the approximate position of the atoms with respect to the Bi lattice marked on top. Mn adatoms in this configuration are separated by 6.72 Å. A pair of embedded Mn impurities can be seen on the left and bottom-left sides of the image and, above the chain, a Mn adatom separated by approximately 3.5 nm.

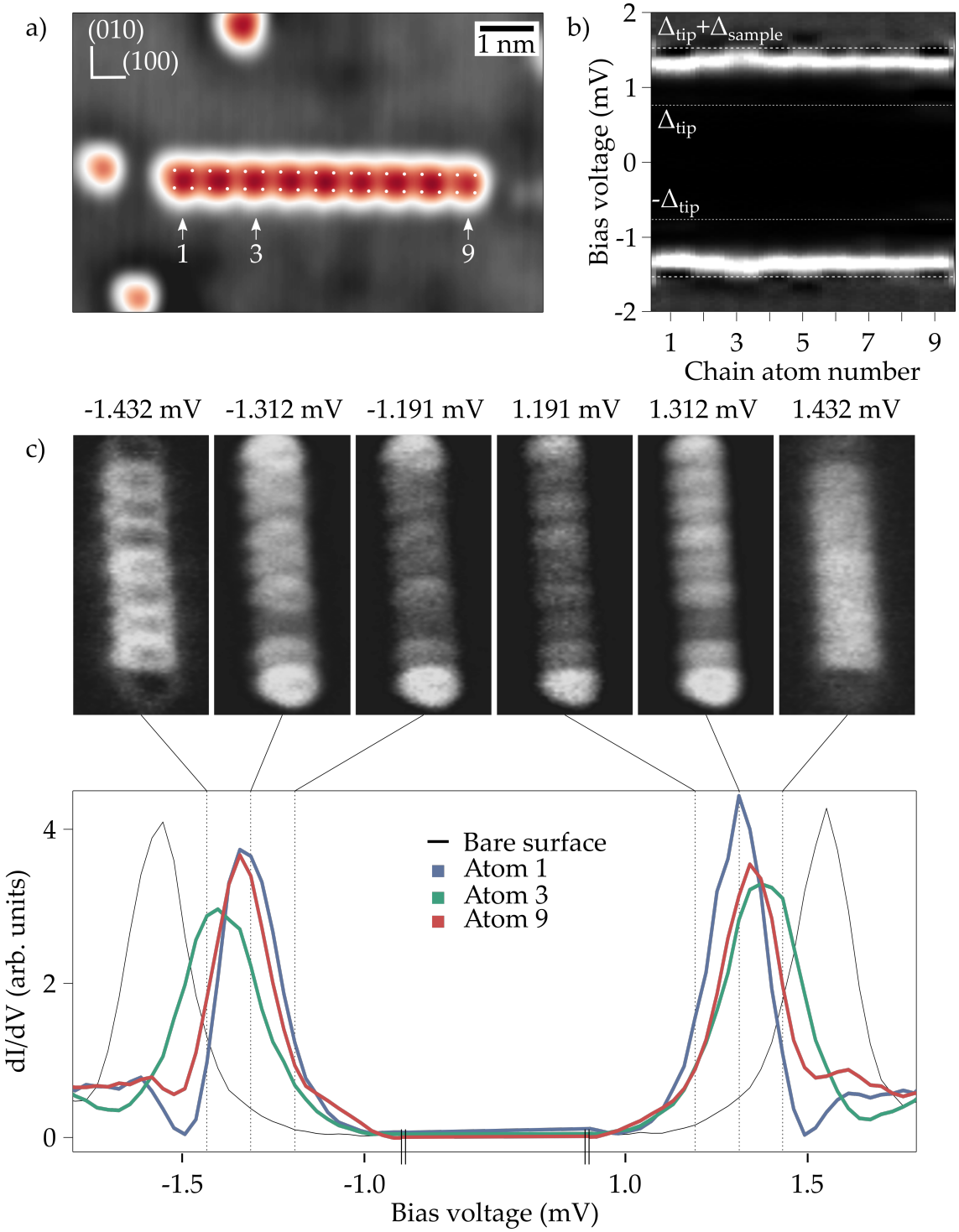

Figure 6.12: Chain of 9 Mn atoms assembled along the (100) direction. a) Topographic map of the chain showing the approximate positions of the underlying Bi atoms. (V_{bias}=3 mV, I_t=45 pA). **b)** Stacked set of spectra showing the YSR states corresponding to each atom in the chain. (V_o=3 mV, I_o=1 nA, V_{RMS}=50 μV). **c)** Top: dI/dV maps extracted from a 40x10 set of spectra measured in a 3.3x6.8 nm area. Bottom: Spectra measured in atoms 1, 3 and 9 indicating the energies of the maps above. (V_o=3 mV, I_o=1 nA, V_{RMS}=50 μV)

In order to characterize the YSR excitations, a superconducting β-Bi_2Pd was prepared after the chain was assembled. In Fig.6.12 b), we show a set of stacked spectra measured with a superconducting along the atoms in the chain. The X-axis corresponds to the atom position in the chain, as defined in the topographic map. The minimum YSR energy appears at the edges of the chain and progressively shifts towards the quasiparticle continuum inside the chain. Starting from the left side of the plot, we appreciate a fast energy shift towards the quasiparticle continuum in the first 3 atoms. After the abrupt change, the energies of subsequent atoms progressively approach the energy of the atom at the edge. Changes between adatoms lie in the 50 μ range, with the minimum energy found in atoms 1 and 9 (1.33 mV and 1.34 mV, respectively) and the maximum in atom 3 (1.40 mV). Disregarding atom 3, the average YSR excitation energy for atoms inside the chain is 1.37 mV, and all the energies are above the ones of edge atoms. To understand the possible origin of the different energies, we compare the YSR excitations in the chain with the statistics shown before. Different tips are used for each measurement so, in order to compare the energies, we calculate the difference between $\Delta_{tip} + \Delta_{sample}$ as measured on the bare surface in each set. We find during the chain measurement this value is 30 μV higher, so that value needs to be subtracted from YSR excitations in the chain for the comparison to be effective. Doing so, we find all the atoms fall into the type-II category, with edge atoms in the lower limit and atom 3 falling slightly above of the statistical limit.

The spatial distribution of the YSR states at different energies is shown in Fig.6.12 c), where the energy cuts are chosen at the slopes of the peaks ($\pm$1.191 and $\pm$1.432 mV) and on top of the edge atoms peak ($\pm$1.312 mV) in order to maximize the contrast between atoms at the edge and inside the chain. The different behavior of atom 3 becomes evident from the maps at $\pm$1.312, where this atom can be distinguished by its lower conductance. Otherwise, adatoms inside the chain show a homogeneous behavior that is only perturbed at the edges of the chain. This could be an indicator of the development of a weak AFM interaction, responsible for the similar excitation energies found along the inner atoms. This hypothesis is strengthened by conductance maps, where we observe wavefunction overlapping without the associated peak splitting. The negligible effect of the perturbation in atom 3 on atoms 2 and 4 would imply that this AFM interaction does not take place between immediate neighbors, in agreement with the absence of coupling in dimers. Although it is tempting to assume that edge atoms show a different excitation because they are subject to this interaction only from one of their sides, as the interaction does not happen between first neighbors this effect would also apply for atoms 2 and 8, an effect not observed in the experiment. Furthermore, confinment effects cannot be discarded as a possible source of edge states at the end of chain.[108] To clarify this question and complete the chain picture, we propose additional measurements in shorter and longer chains, focusing in the energies of edge states and the analysis of the inner atoms with higher-resolution superconducting tips.

In conclusion, the excitation spectra of chains along the (100) showed this configuration could hold potential as a candidate for an AFM chain. However,

the different behavior found in one of the atoms still needs to be clarified. Additionally, we have proposed confinement effects as a plausible origin of the energy shift at the edges of the chain, a question that still requires confirmation from additional measurements.

Evolution of YSR Excitations in a Mn_{13} Chain

The observation of signatures of ferromagnetic ordering in Mn dimers in the $\sqrt{5}$ configuration motivated the construction of the 13-atom Mn chain in Fig.6.13. The shape of the constituent atoms can be distinguished due to the relatively large distance between atoms (7.51 Å). The atoms are labeled from left to right by their position in the chain.

In Fig.6.13 b) we show the excitations in atoms 3 and 11 and a spectrum on the bare surface as measured with a metallic tip. At the working temperature of 1.3 K, the thermal-broadened DOS of the tip shows the YSR excitations overlapping with the quasiparticle continuum instead of as individual peaks, resembling a smaller superconducting gap. The innermost part of this apparent gap corresponds to the slope of the peaks. Comparing the spectra in atoms 3 and 11, we can identify a lower-energy excitation in the former and assymetry between the electron and hole components. Fig.6.13 c), a set of spectra measured along the chain shows the evolution of YSR states along the chain, where a non-standard colormap has been used to enhance the position of the YSR states slope. The edges of the image correspond to the bare surface. Following the yellow line, the position of the slopes of YSR states gives an approximate idea of the energy difference between the excitations in each atom. We distinguish variations in YSR energies along the chain, in accordance with the statistical distribution of energies found in isolated atoms.

To discern between statistical variations, confinement, and coupling effects in the energy of YSR excitations, we compare the energies of the peaks at different stages of the chain asembly. We focus on three intermediate cases (5, 8 and 11 atoms) and the final 13-atom chain. Fig.6.14 a) shows the same chain at the different stages considered, where atoms are indexed by their position in the final chain in order to track their evolution.

Given the low energy resolution of metallic tips at our working temperature, we evaluate the energies of YSR states from the position of the midpoint of the slope. The width of a YSR peak is determined by the lifetime of the state and the thermal distribution of electrons around the Fermi level of the tip.[85] At 1.3K the latter is significantly larger, thus allowing us to consider the peak width is mainly given by thermal broadening, which is the same for every atom. Assuming the height of YSR peaks is constant along the chain, a change in the energy of the peak will cause the same change in the energy of the middle point of a peak slope. Using this procedure, we extract the approximate energy of the excitation from a fit of the slope to a third degree polynomial, as depicted in Fig.6.14 b). Although the procedure is mostly limited to the approximation of energy changes in YSR

energies, using this procedure to calculate $\Delta_{\beta\text{-}Bi_2Pd}$ we obtain 0.748 mV, a good approximation to the experimental value.

The distribution of peak energies at each stage as extracted using the aforementioned procedure is plotted in Fig.6.14 c). The evolution of peak energies along the chains shows a marked oscillatory behavior, which is preserved upon positioning of additional adatoms. The oscillation period is approximately 2 Å, as estimated from the maxima and minima in curves III and IV. Such a periodicity is compatible with an asymmetric exchange interaction.[109–111] In the limit of close-by impurities, and particularly in nested Fermi surfaces, spin susceptibility is not significantly modified by the superconducting transition[112], so we expect these interactions to still apply to our system. Furthermore, even FM-ordered chains in 3D superconductors may develop spiral spin textures in the presence of superconducting correlations,[113] so we expect magnetic order in the chain to be non-parallel.

An intriguing property of the chains is the preservation of the oscillatory behavior upon addition of extra atoms. Particularly, we observe that, not taking into account edges atoms, the phase of the modulation does not change when the length is increased. We do not know exactly know which could be the mechanism responsible for this. Confinement effects can be disregarded because changes in length would have an associated period change. Although surface inhomogeneities cannot be discarded, we observe that, as the length of the chain increases, the energy difference between maximum and minimum energies in the

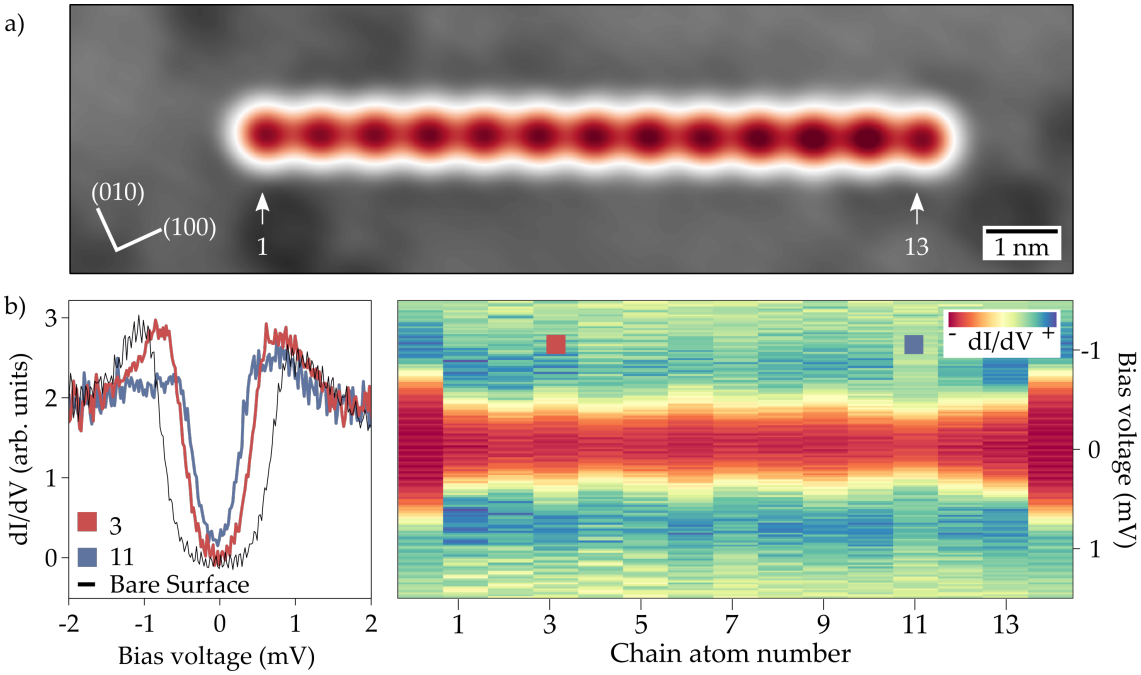

Figure 6.13: Chain of 13 Mn atoms constructed along the (120) direction. a) Topographic map of the chain. (V_{bias}=200 mV, I_t=100 pA). **b)** YSR excitations in atoms 3 and 11, as measured with a metallic tip. (V_o=3 mV, I_o=300 pA, V_{RMS}=50 μV). **c)** Set of stacked spectra measured along the chain. Same parameters as b).

oscillation increases accordingly. This implies that some emerging phenomenon is enhancing this difference. This question is left open, but we propose the observed length-dependence may be motivated by the stabilization of the order inside the chain.

The excitation energy of states at the end of the chain show termination ef-

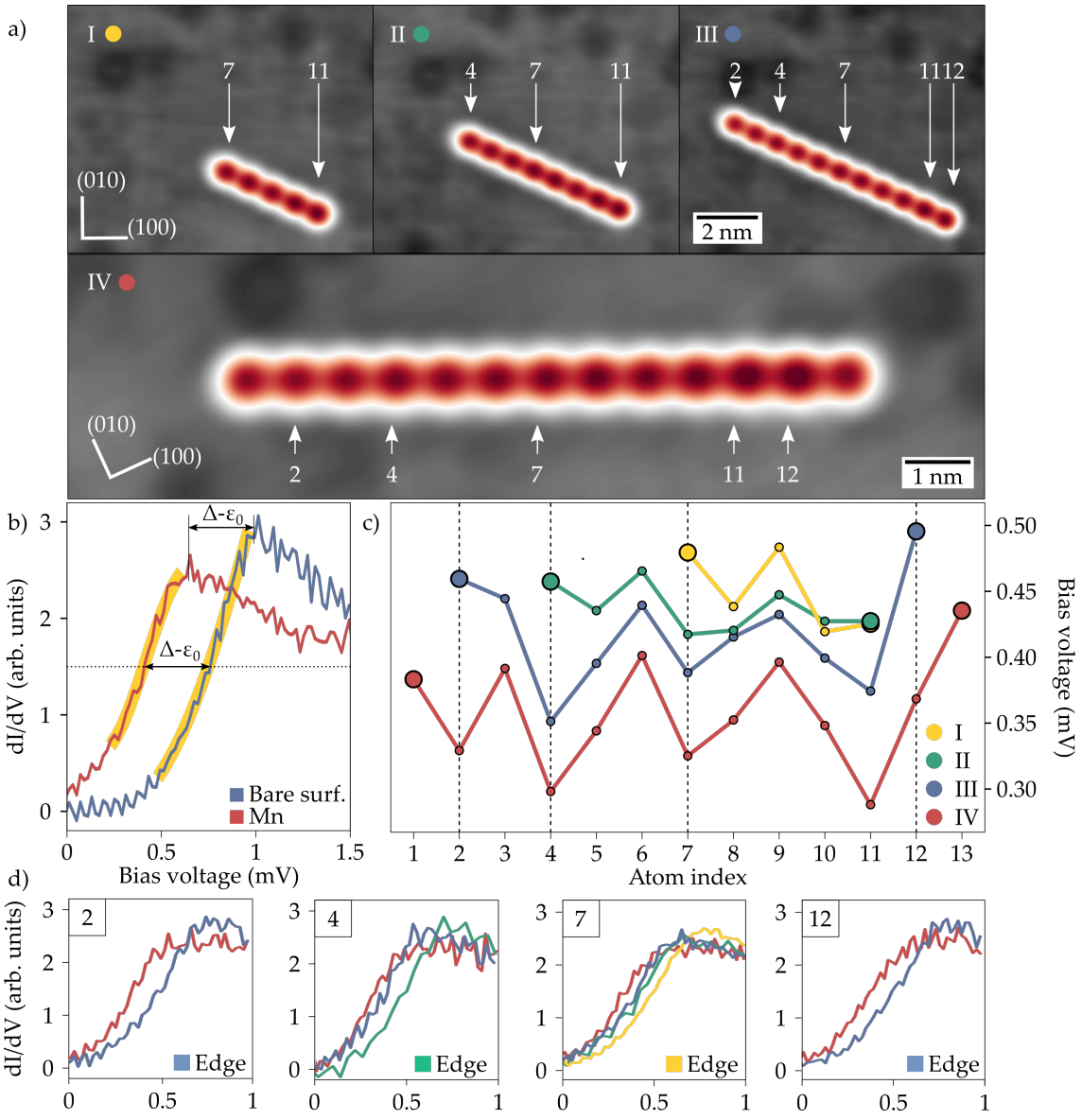

Figure 6.14: YSR excitations for different chain lengths. a) Topographic maps at the Mn chain at the different stages. The different maps correspond to the Mn_5, Mn_8, Mn_{11} and Mn_{13} stages and edge atoms are labeled at each step by their position in the 13-atom case (V_{bias}=200 mV, I_t=100 pA). **b)** Fitting procedure used for extracting the change in YSR excitation energy Δ-ϵ_0. **c)** Energy of YSR states at the different stages of construction. Colors indicate the stage (see a). Dashed lines indicate edge atoms at each stage. **d)** Evolution of YSR states in atoms 2, 4, 7 and 12. The different colors indicate the stage of the chain (see a and c) Labeled plots indicate the atom was one of the edges of the chain in that stage.

fects at every step of the chain construction. In Fig.6.14 d) we show the excitation spectra of edge atoms at the different stages of the chain. We observe edge atoms always have higher energies when they are at the edge than when they are among the inner atoms. Additionally, we see that energy modulations tend to breakdown at the edges, but when additional atoms are added the periodicity of the modulations in those atoms is recovered. This effect could be attributed to a confinement effect, where states at the edge may influence the energy of YSR states. We would expect those effects to have an associated signature inside the chain not observed in the experiment, but this picture cannot be discarded without further measurements. Another possible cause for this termination-effect would be the stabilization of a magnetic order in the chain edges, but this is a question that would also needs further examination.

The overall energy of the chain shifts towards ϵ_F as the length is increased. We observe this shift is more noticeable when the chain length increases from 11 to 13 atoms. Focusing on atom 10, an inner atom during the whole construction, we see its energy shifts very little during the first stages, but when the chain goes from 11 to 13, it shifts approximately 0.1 meV. Although this may not seem like a great variation, it implies that addition of two atoms to the chain results in a shift of approximately $13\%\Delta_{\beta\text{-}Bi_2Pd}$, a remarkable energy decrease. If the trend is preserved, chains of $\sim$20 atoms would already start showing Fermi-level crossings, from which quantum phase transitions and many other interesting effects may derive.

Summarizing, we have approximated the energies of YSR states in a Mn_{13} along the (120) direction and found an oscillatory behavior of YSR modulations and a overall shift to lower energies with increasing chain length. Although is it is difficult to elucidate the exact mechanism causing these effects, we anticipate that increasing the chain length Fermi-level crossings may take place.

6.5 Ferromagnetic Coupling in Other Transition Metals

FM Coupling in Fe Dimers

Fe appears as the paradigmatic example of ferromagnetism in many single-atom experiments.[18,114,115] Its $[Ar]3d^64s^2$ electron configuration confers the element a strong magnetic character and a S=2 free-atom spin. As-deposited Fe atoms appear on the surface of β-Bi_2Pd as 150 pm protrusions (Fig.6.15 a), accompanied by some dimers formed during evaporation (recognizable as the elongated structures indicated by arrows in the image). A close-up examination of topographic images reveals that the lattice underneath Fe adatoms is slightly perturbed (cross-shaped dark areas along the crystallographic directions), as found for intrinsic Bi impurities. Evaporation below 13 K makes the diffusion of Fe to vacancy sites very unlikely, which may indicate that Fe distorts the lattice below.

Despite their S=2 free-atom spin, Fe adatoms show no YSR excitations within the limited energetic range provided by the β-Bi_2Pd tips used during the experi-

ment. Strong hybridization with the substrate may reduce the magnetic moment of the impurity, making it lose its magnetic character.[116] Contrarily to isolated adatoms, the Fe dimers formed during evaporation show a YSR excitation close to 0 energy (Δ_{tip} in our experiments). This unexpected behavior must be caused by ferromagnetic coupling between the impurities, inducing an orbital rearrangement and a non-zero magnetic moment. The low energy of the excitation indicates a strong coupling between the superconductor and the dimer, a desired property for Majorana chains. Unluckily, during the time of this work, we were not able to find a reproducible procedure for the controlled manipulation of Fe atoms. Given the strong coupling observed in dimers, Fe may be more strongly bound to the substrate than Mn, which may prevent the lateral manipulation of the adatoms. Other manipulation procedures could be used in the future to solve this issue, making Fe a strong candidate for the construction of topological chains.

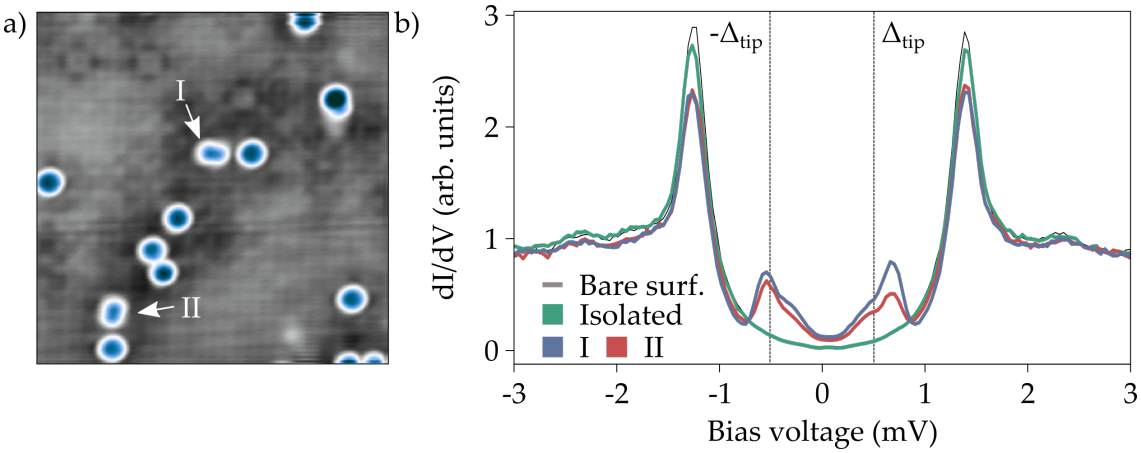

Figure 6.15: Spectroscopic characteristics of Fe on β-Bi_2Pd. a) Topographic map showing the different species found after deposition (V_{bias}=5 mV, I_t=1 nA). **b)** Excitation spectra of the different species. I and II correspond to the dimer-like species and were measured on the adatoms indicated in the topography map (V_o=5 mV, I_o=500 pA, V_{RMS}=75 μV).

FM COUPLING IN V DIMERS

The spectroscopic characteristics of isolated V adatoms on β-Bi_2Pd were extensively discussed in chapter 5. One of the fascinating properties of these adatoms is the large extension of their YSR wavefunction, which makes it an interesting candidate for the formation of YSR bands. To investigate this possibility, we construct the (2,0) dimer in Fig.6.16 a), with V adatoms separated by 6.72 Å. The position of the underlying Bi atoms is indicated on top of the dimer.

We obtain the excitation spectrum of this configuration from an averaged set of 30x60 spectra measured on the area in a). In Fig.6.16 b) we show the resulting in-gap states on top of the spectrum of an isolated atom averaged using the same procedure. Instead of the three peaks found in isolated V atoms, in the (2,0) dimer we identify four peaks (labeled α, β, γ and δ from lower to higher energy). α and

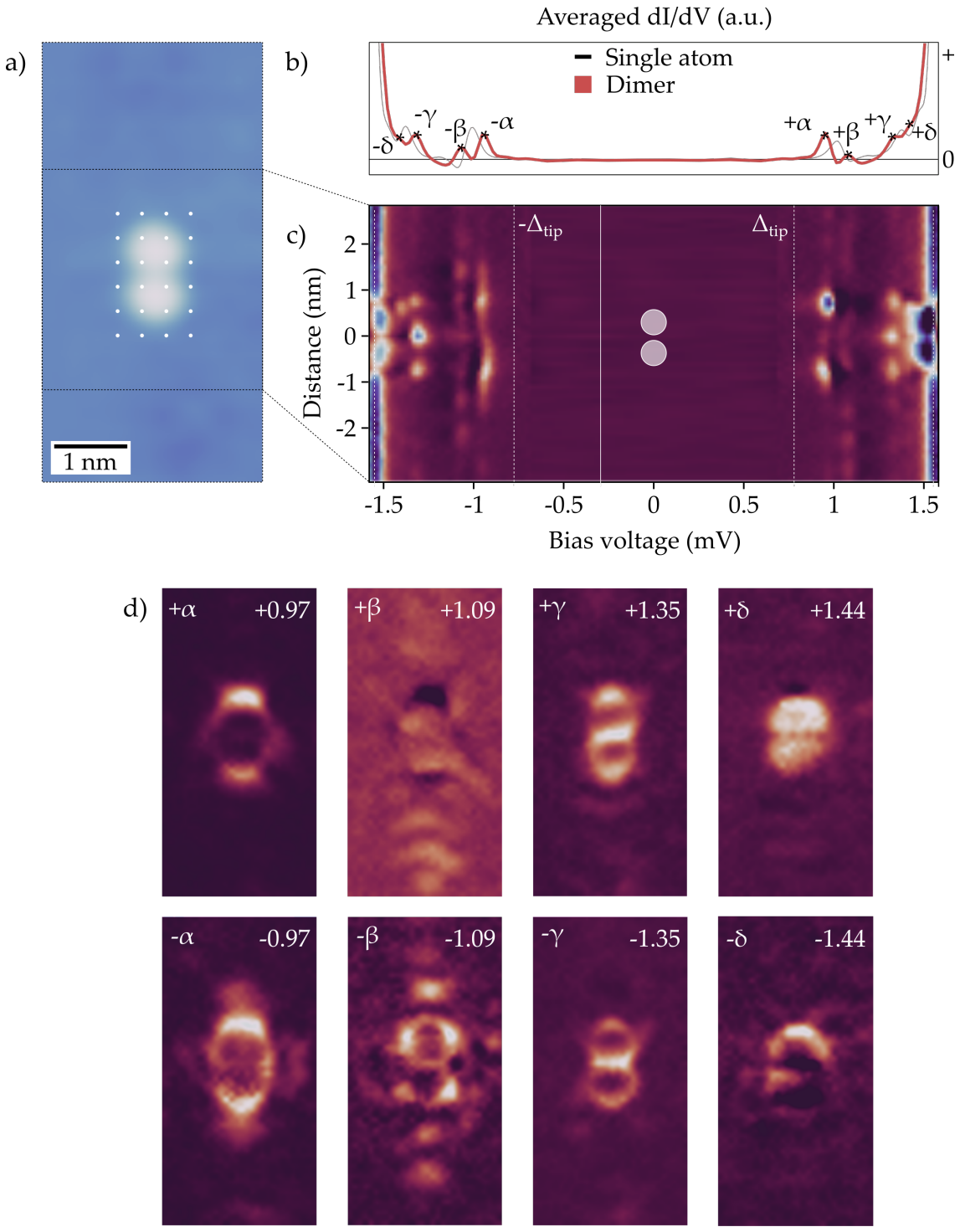

Figure 6.16: YSR excitation spectra of a 2 u.c. V dimer. a) STM topography of the 2 u.c. V dimer (V_{bias}=-3 mV, I_t=300 pA). **b)** Series of stacked spectra along the black line in a) (V_o=-3 mV, I_o=300 pA, V_{RMS}=25 μV). **c)** Conductance maps extracted as energy cuts of a grid of spectra at A_1 (0.94 mV) and A_2 (1.05 mV) (V_o=-3 mV, I_o=300 pA, V_{RMS}=50 μV).

β appear in the vicinity of the first peak found in isolated atoms, and γ and δ in the vicinity of the second.

A set of spectra in Fig.6.16 c) shows the spatial distribution of the states along the dimer.The three lowest-energy peaks, α, β and γ, show an extended state over the impurities with either minima or maxima at the center. The electron component of peak γ is mostly hindered by the coherence peaks and its hole component shows a small peak centered in the top atom. The counterpart of γ in the second atom appears to have shifted to higher energies, merging with the coherence peaks.

To confirm that the low energy states are distributed along the dimer, we extract constant-energy dI/dV maps from the set of 30x60 spectra used to calculate the averaged density of states. In Fig.6.16 d) we show the maps at the energies of the peaks. The complicated structure of the maps prevents the identification of even an odd components at the different energies. However, they demonstrate the hybridization of extended states in V dimers and, from the emergence of an additional state, we conclude that at least two states correspond to the even an odd components of a FM-coupled pair.

6.6 Conclusions

In this chapter we have analyzed the excitation spectra of Mn adatoms in different configurations. From the analysis of the excitations in isolated atoms, we have identified a broad range of YSR energies. Combining the strong localization of YSR states in atoms and their spherical shape we have proposed the presence of multiple degenerate *d*-orbitals as the origin of the broad range of energies. Furthermore, we have shown signatures of additional peaks in a small subset of Mn adatoms, in agreement with the proposed model.

Using lateral manipulation, we have constructed dimers in different configurations, finding signatures of AFM coupling in atoms separated by 3.4 Å and 4.8 Å, and a possible FM order in atoms separated by 7.5 Å. We have proposed additional experiments to confirm these findings. Moreover, during the construction of the dimers we have found that (1,0) dimers cannot be used to construct longer chains and that $\sqrt{2}$ dimers are in a metastable configuration.

We have then moved to longer structures, were we have shown indicators of a weak AFM coupling in a 9-atom chain along the (100) direction and of a possible emerging magnetic ordering along the (210) direction. Particularly, the evolution of YSR states in a Mn_{13} in the (210) shows the system could be driven through a quantum phase transition if more atoms were added to it.

Finally, from the excitation spectra of as-assembled Fe dimers and constructed V dimers, we have shown Fe and V are promising transition metals for the topological chains in β-Bi_2Pd.

Chapter Seven

Lifting the Degeneracy of Vibrational Modes in Vanadium Hydrides

Vibrational spectroscopy provides a powerful mechanism to distinguish different chemical species at the atomic scale. When combined with superconducting tips and substrates, minute spectroscopic features can be distinguished in the vibrational spectra.

In this chapter, we use Inelastic Electron Tunneling Spectroscopy (IETS) to characterize the vibrational modes of Vanadium hydrides on the surface of β-Bi_2Pd. With the help of isotopic substitution we distinguish between internal and external vibrational modes of the molecules. The enhanced resolution obtained with superconducting tips allows us to identify a lifted degeneracy in the vibron spectra of the molecule. Combination of this observation with the topographic characteristics of the molecules allow us to identify the vibrational modes and propose a candidate symmetry-breaking mechanism. In the last section, we study the effect of hydrogenation on the YSR excitation spectra of V adatoms and find H induces substantial changes beyond the expected change in d-orbital occupation.

7.1 Vanadium Hydrides on β-Bi_2Pd

Deposition of Vanadium on the surface of β-Bi_2Pdpresented the two different V-related adsorption species shown in Fig.7.1 a), b). Only an approximate 12% of the adsorbates correspond to pristine V (bottom), recognizable as 140 pm protrusions with the properties discussed in chapter 5. The most significant fraction of the evaporation corresponds to Vanadium hydrides, recognizable as 80-pm-high ring-shaped items in the image. Most of these hydrides are geometrically uniform (top), but a small percentage (<10%) shows varying degrees of asymmetry (middle), resembling a rotated or tilted version of the former. Hydrides form during cryogenic evaporation of transition metals (TM) in UHV environments[115,117,118], mainly as a result of the excellent performance of 3d-series elements as catalysts for H_2 dissociation at low temperatures[119]. Upon dissociation, highly-reactive H combines with V to form hydrides.

Irreversible transformation of Vanadium hydrides to pristine V can be induced by the electrostatic potential between the tip and the sample[120,121]. H is removed from the molecules when a V_{bias} threshold is reached during a constant-current bias sweep (Fig.7.1 c). The tip position registers dehydrogenation as an abrupt 60-pm height change after which pristine V is obtained. Additionally, large areas can be H-depleted scanning at V_{bias}=+1 V I_t=100 pA. This methodology can be applied to selectively remove H from individual hydrides provided that V_{bias} does not reach much higher values than the threshold voltage (Fig.7.1 d). If high-V_{bias} pulses ($\sim$2 V) are applied, areas of approximately 10 to 20 nm^2 around the pulse position are depleted of H.

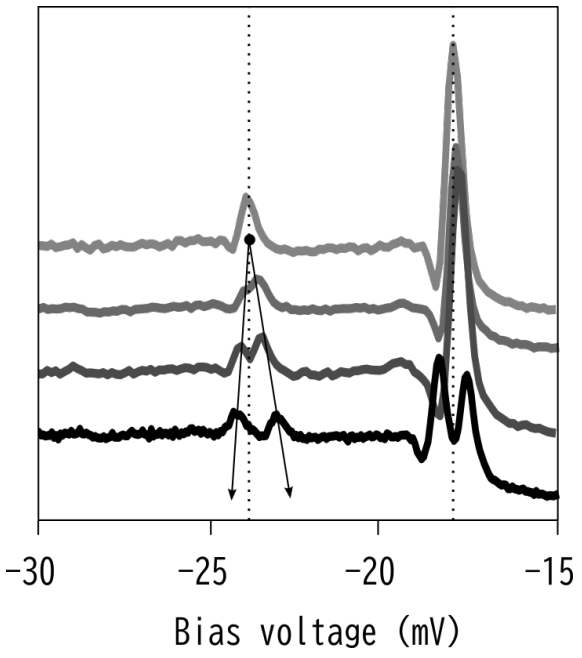

7.2 Spectroscopy of Hydrides

STS measurements on flat V hydrides show two pairs of energy-symmetric peaks associated to the onset of inelastic tunneling at energies $\pm\epsilon_1$ and $\pm\epsilon_2$ (Fig.7.2 a). Inelastic steps appear as peaks as a result of the convolution of the step with the DOS of the superconducting β-Bi_2Pdtip. As both tip and sample are super-

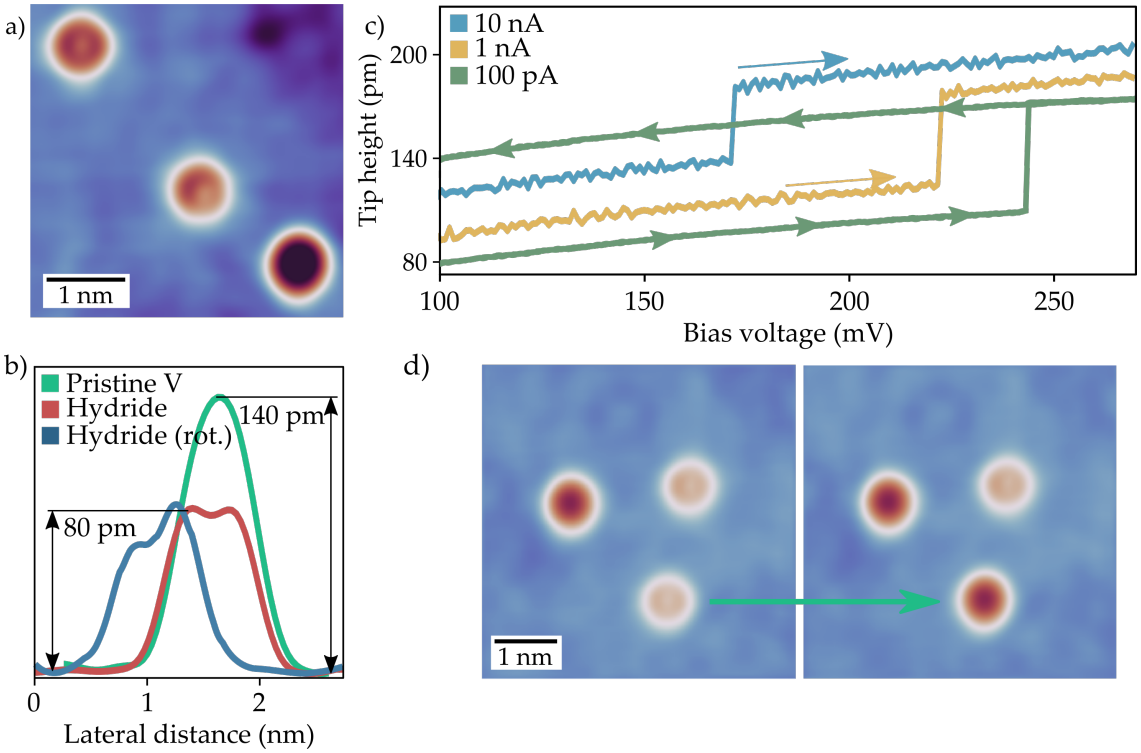

Figure 7.1: Vanadium Hydrides. a) Different species found upon V evaporation. Top: Hydride, Middle: Asymmetric Hydride, Bottom: Pristine V. (V_{bias}=-3 mV, I_t=900 pA) **b)** Profiles along the species in a). **c)** Irreversible dehydrogenation during constant-current bias sweeps at different setpoint currents. **d)** Selective dehydrogenation.

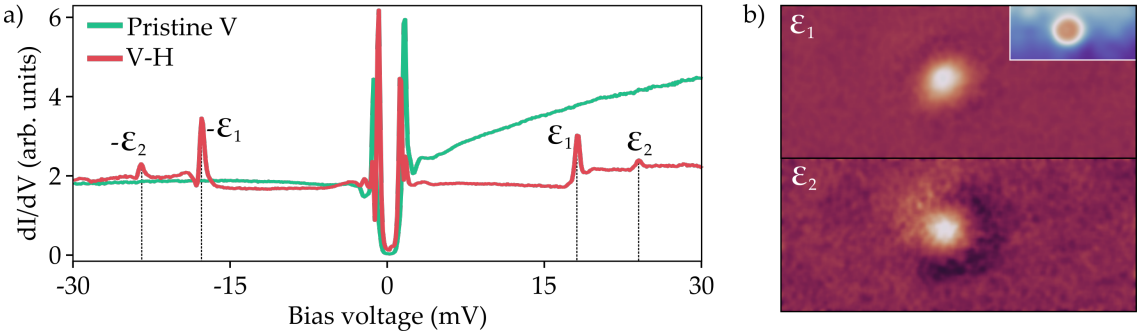

Figure 7.2: Inelastic excitations in V Hydrides.a) Inelastic excitations at energies ϵ_1=17.9 meV and ϵ_2=23.9 meV measured with a β-Bi_2Pdtip in a non-tilted V hydride (red). A spectra on pristine V is shown for comparison (green). (V_{bias}=-30 mV, I_t=300 pA, V_{rms}=125 μV). **b)** Conductance maps at the energies of ϵ_1 and ϵ_2, showing the spatial distribution of the excitations along the hydride. Inset shows the topography of the area. (I_t=500 pA, V_{rms}=250 μV)

conducting, the absolute values of the inelastic excitations are calculated as $E_{exc} = \epsilon - (\Delta_{tip}+\Delta_{sample})$[122]. The corrected energies of the excitations are E_{1H}=16.3 meV and $E=_{2H}$=22.3 meV. Both excitations are localized at the center of the molecule (Fig.7.2 b). The energies of ϵ_1 and ϵ_2 are compatible with low-frequency vibrational modes and well above typical values found for spin excitations on metallic substrates (<10 meV)[123–125]. This points towards a vibrational origin of the excitations.

To confirm the vibrational origin of inelastic excitations, we substitute Hydrogen by Deuterium by exposing pristine V adatoms to 39 Langmuir D_2. The different mass of the isotope changes the energies of vibrational modes and can be used to confirm the vibrational nature of the excitations[44]. Exposure to molecular D forms a small number of molecules with topographic characteristics similar to V hydrides (Fig.7.3 a). These molecules show a pair of energy-symmetric excitations at corrected energies E_{1D}=11.9 meV and $E=_{2D}$=21.9 meV7.3, lower than the values found for hydrides and thus acknowledging a vibrational origin.

The energy shift of vibrational modes caused by isotopic substitution allows us to discern between internal and external (frustrated) vibrational modes of the molecule. Molecular vibrations can be modeled as an harmonic oscillator, where the energy of the n-th level of the vibrational mode will be given by[126]:

$$E_n = h\left(n + \frac{1}{2}\right)\frac{1}{2\pi}\sqrt{\frac{k}{m}} \tag{7.1}$$

where h is Planck's constant, k is the spring constant and m the mass of the system.

The mass of the oscillator m depends on whether the oscillation involves the movement of an individual atom (internal modes) or the molecule as a whole

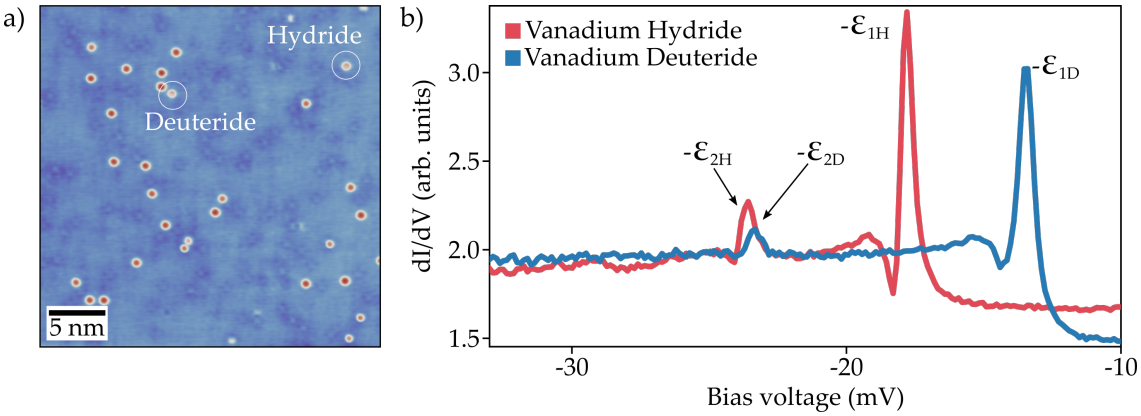

Figure 7.3: Isotope substitution. a) Deuteride formed after exposure to D_2. (V_{bias}=-3 mV, I_t=100 pA) **b)** Inelastic excitations at energies $-\epsilon_{1D}$=-13.4 meV and $-\epsilon_{2D}$=-23.4 meV measured in a V deuteride. Equivalent measurement on a V hydride is shown for comparison. (V_{bias}=-30 mV, I_t=300 pA, V_{rms}=125 μV)

(external modes). As a result, assuming the molecules contain a single H or D, the ratio between the energies of the internal vibrations of the hydrogenated and deuterated species will follow:

$$\frac{E_{HV}^{int}}{E_{DV}^{int}} = \sqrt{\frac{m_D}{m_H}} = \sqrt{\frac{2.01}{1.01}} = 1.410 \tag{7.2}$$

Accordingly, for external modes:

$$\frac{E_{HV}^{ext}}{E_{DV}^{ext}} = \sqrt{\frac{m_V + m_D}{m_V + m_H}} = \sqrt{\frac{52.95}{51.95}} = 1.01 \tag{7.3}$$

The ratio between the energies of the hydrogenated and deuterated species is by means of the previous equations an indicator of the type of vibrational mode. The experimental values and the calculated ratios between hydrogenated and deuterated species are summarized in Table 7.2. Comparison with the calculated ratios allow us to identify ϵ_1 as an internal vibrational mode of the molecule and ϵ_2 as an external one, showing excellent agreement with the calculated values.

Vibrational mode	E_H	E_H	Ratio
ϵ_1	16.3	11.9	1.369
ϵ_2	22.3	21.9	1.018

Linear diatomic molecules have 9 possible rotational modes when adsorbed on tetrgonal crystal surfaces: 3 internal modes (stretching along the Z axis and a two fold-degenerate rotation) and 6 external modes (In-phase and anti-phase stretching along the Z axis, two-fold-degenerate in-phase rotations and two-fold-degenerate anti-phase rotations). The identity of the different vibrational modes cannot be directly inferred from their peak energies in the absence of DFT calculations or measurements using different techniques besides STM. In the following section we will show that broken degeneracies allow us to identify the internal mode and reduce by two the possible external modes.

7.3 Degeneracy Lifting in Tilted Molecules

Tilted V hydrides show a higher number of vibrational modes. Fig.7.4 a) compares the spectra of a flat hydride (top) and 3 tilted hydrides, where ϵ_2 splits into ϵ_{2A} and ϵ_{2B}. The biggest splitting of ϵ_2 is accompanied by a similar splitting of ϵ_1. This splitting occurs evenly along the molecules (Fig.7.4 b), confirming it is an intrinsic property of tilted molecules on β-$Bi_2Pd$and not a site-dependent effect.

The vibron spectrum of a molecule presents degenerate modes induced by symmetry constraints. As a consequence, if that symmetry is broken to some

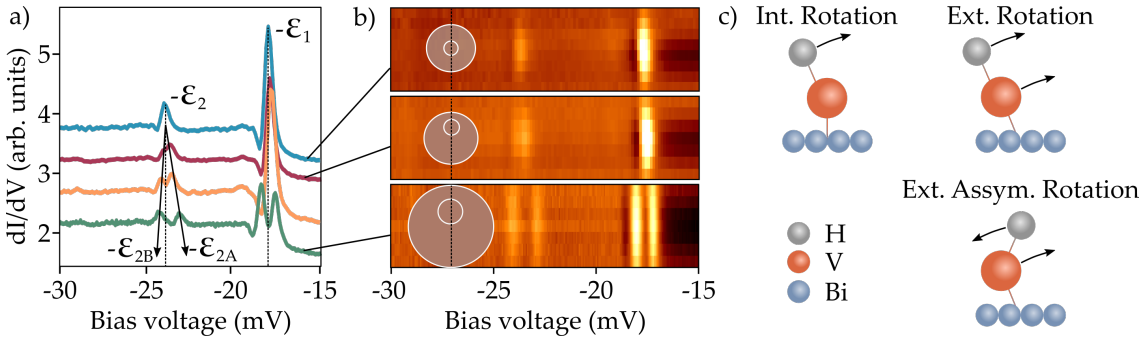

Figure 7.4: Inelastic excitations in tilted hydrides. a) Splitting of inelastic excitations in tilted hydrides. From top to bottom, spectra on 4 different hydrides are ordered by the degree of splitting of ϵ_2. Top spectra corresponds to a non-tilted hydride for reference. (V_{bias}=-30 mV, I_t=300 pA, V_{rms}=125 μV) **b)** Spectra measured along hydrides showing splitting is uniform along the molecule. The position of the spectra along the molecule is indicated on the left. (V_{bias}=-30 mV, I_t=300 pA, V_{rms}=125 μV) **c)** .

extent, the modes may split into multiplets. Not all the vibrational modes are degenerate, and hence peak splitting provides a hint into the possible vibrational modes from which ϵ_1 and ϵ_2 originate. Fig.7.4 c) shows the degenerate vibrational modes of a linear diatomic molecule.

Assuming V hydrides are linear and contain a single H on top, the only degenerate internal modes found in this configuration corresponds to rotations. In this modes, H vibrates in X or Y and degeneracy can be lifted by defining inequivalent energetic landscapes in these directions, as it is the case for molecules showing an apparent rotation. We conclude then that ϵ_1 corresponds to an internal rotation and its splitted states to displacements of the top H or D atom in X or Y. Among the 6 possible external modes of the molecule, again peak splitting allows us to discrd the two that correspond to displacements along the Z axis. The remaining modes share similar symmetry constraints and thus impede the identification of the precise vibrational mode. We can, however, identify ϵ_2 as a rotational mode leaving open the possibility of being the in-phase or anti-phase mode.

The broken degeneracies show that the apparent rotation reflects a non-balanced distribution of the hydride among the surrounding Bi atoms. This distribution results in hydrides experiencing a non-uniform crystal field that lifts the degeneracy of the vibrational modes and translates into the apparent rotation of the molecules found in topographic scans. The rotation can be caused either by a non-homogeneous surface (see section 4.2) or by the uneven distribution of V adatoms among the 4 Bi atoms forming the hollow site. The apparent rotation would hence be an indicator of the degree of assymetry experienced by the molecules along the X and Y axes. In this picture the degree of assymetry is not limited by any constraints and energy splitting must show a continuous distribution of values.

To evaluate the feasibility of the aformenetioned symmetry breaking picture,

we compare the vibrational modes in a set of 19 rotated hydrides ordered by the value of ϵ_{2A} (Fig.7.5). Peak energy is estimated as the bias voltage at the highest point of the peak in the spectrum and, when two peaks are not clearly resolved (see red spectra in Fig.7.4 a), peak energy is given by the energy at the highest point independently of peak symmetry. Energies appear in a non-discrete set of values, indicative of a continuous variation of the symmetry-breaking parameter compatible with the different degrees of rotation found in molecules.

ϵ_2 appears to be more sensitive to the degeneracy-lifting mechanism and hence we consider the value of ϵ_{2A} as indicative of the symmetry-breaking strength. Splitting of ϵ_1 seems to require a higher *strength* in order to show splitting. Being an internal mode in which the atom on top vibrates, it is reasonable to believe that this mode is less sensitive to variations in the potential landscape felt by the atom at the bottom. ϵ_2, on the other hand, involves also the movement of the V adatom sitting on top of Bi adatoms and is thus more sensitive to changes in V-Bi distances. Subsequently, the higher *strength* required for the internal mode ϵ_1 to show splitting is in agreement with the model of atomic vibrations developed in the previous paragraphs, confirming the feasibility of the proposed model.

Summaryzing, the apparent rotation of V hydrides reflects assymetries in the crystal environment of the molecule. These assymetries lift the two-fold degeneracy of internal and external rotational vibrational modes, which are differently affected by this broken symmetry because modes involving the V atom below are more sensitive to changes in the crystal-field. First-principle calculations to confirm the proposed model are being performed by Shreya Sinha and Peter Saalfrank in the University of Postdam.

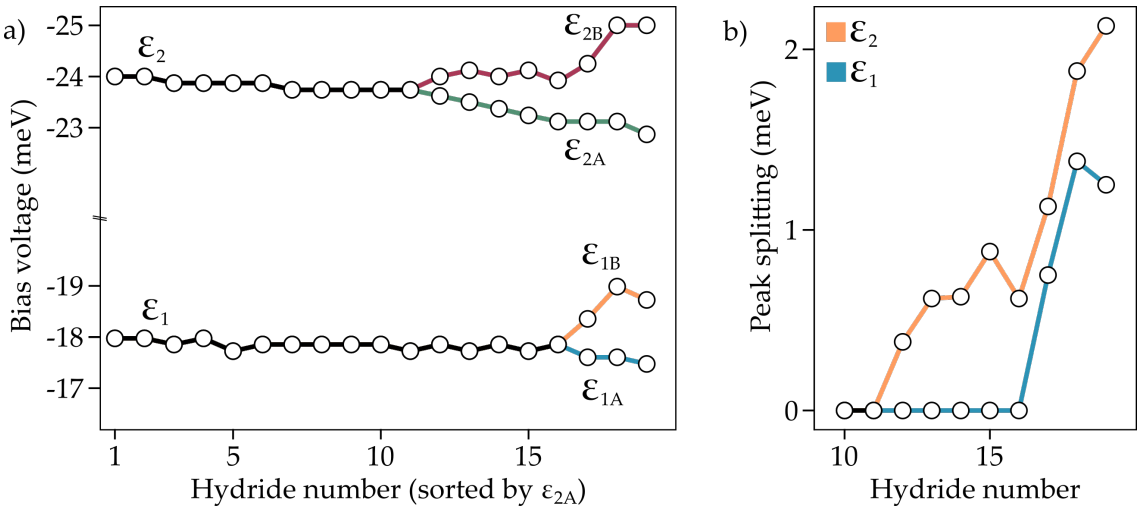

Figure 7.5: Progressive splitting of vibrational modes. a) Peak energies extracted from a set of 19 tilted V hydrides. Peaks are arranged by the value of ϵ_2 and X axis just indicates a hydride identification number. (V_{bias}=-30 mV, I_t=300 pA, V_{rms}=250 μV) **b)** Peak splitting calculated as the energy difference between peaks A and B of ϵ_1 and ϵ_2.

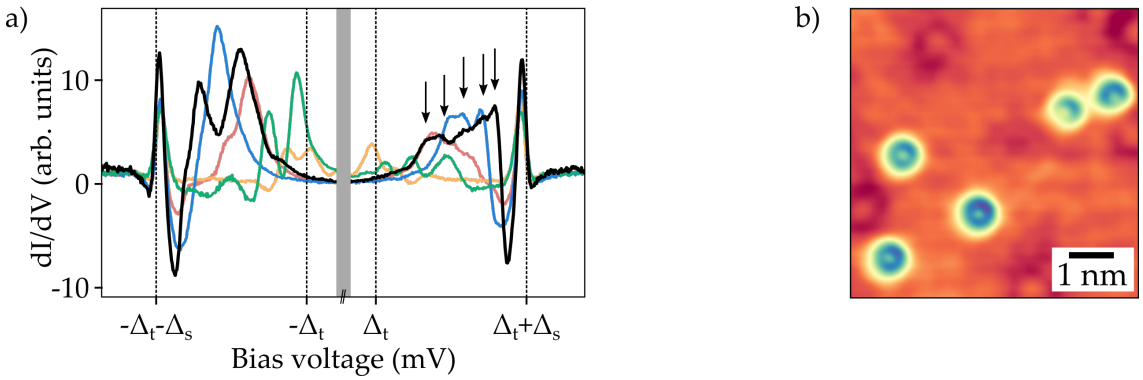

Figure 7.6: In-gap states in vanadium hydrides. textbfa) In-gap states measured at equivalent positions of 5 flat V hydrides. Black arrows indicate peaks in the corresponding spectrum. (V_{bias}=-3 mV, I_t=300 pA, V_{rms}=25 μV) **b)** Topography of a different set of Vanadium hydrides showing slight rotations in flat hydrides.

7.4 *Effect of Hydrogenation on in-gap states*

The possibility of controlling the spin configuration of V adatoms by selective hydrogenation opens the possibility of using H as a mechanism to tune the energies of YSR states. Spectroscopic measurements of the low-energy excitations of flat Vanadium hydrides, however, reveal a great disparity between different molecules, a phenomenon not observed in pristine V adatoms. Fig.7.2 a) illustrates the in-gap states of 5 flat V hydrides as measured with a superconducting β-Bi_2Pdtip. The energies of the excitations and their number change between molecules, finding up to 5 overlapping excitations in some of the molecules. The randomness of these excitations extends beyond the examples shown in the figure, showing different sets of excitations for virtually every molecule.

In the preceding sections we have proposed breaking of crystal symmetries as a degeneracy-lifting mechanism for the vibrational modes of V hydrides on β-Bi_2Pd. For YSR states, degeneracy follows from degeneracy of half-occupied *d*-orbitals[14]. The energy of these orbitals shares with vibrational modes a strong dependence on the crystal environment around the molecule and hence the same mechanism may be responsible for the disparity in peak energies found in YSR staes. It is noteworthy to say that pristine V, despite originating from the same hydrides and thus experiencing the same variations of the crystal environment, does not show this complex behavior. H must hence significantly modify the orbital structure of V in order to be accountable for the YSR excitation spectra of hydrides. This would explain the disparity in peak energies provided that hydrides show more variability than the one simplified rotated/non-rotated picture. To confirm this hypothesis, we show a topographic map in a high-contrast color scale of a 6.5x6.5 nm area with different hydrides. The hydrides on the top-right part of the image belong to the class identified as rotated hydrides and show a clear tilting of the molecule axis. The remaining hydrides belong to the class of flat hydrides. This high-contrast map shows that even in those hydrides the top part is not perfectly flat, what could be the underlying reason for the disparity

found in the YSR excitation spectra of V hydrides.

The explanation of the YSR excitation spectra in terms of these slight rotations of the molecules indicates that upon H adsorption the resulting molecule becomes extremely sensitive to inhomogenities in the crystal field of Bi atoms below. Characterization of this effect would require an extensive examination of a big number of V hydrides and thus can only by proposed as a plausible explanation of the observed effect. Additional contributions to the in-gap excitation spectrum could come from low-energy vibrational modes, that could add Andreev modes depending on the energies of the mode[90]. These vibrations must have energies in the order of the superconducting gap and are in principle not observed in the vibrational spectrum. They could, however, lie at energies very close to the superconducting gap. Additional measurements would also be required to confirm this hypothesis.

7.5 Conclusions

In this chapter, we have used inelastic spectroscopy to study Vanadium Hydrides formed upon depositon of V on the surface of β-Bi_2Pd. Comparing the excitation spectra obtained with different H isotopes, we have been able to confirm the vibronic origin of inelastic excitations in the hydrides excitations and discern between internal and external modes.

Combining the shape of the hydrides in topographic images with high-resolution spectroscopy using superconducting tips, we have been identified a lifted degeneracy of the vibrational modes from an energy splitting in the order of the thermally-broadened energy resolution of the system. Furthermore, we have proposed a degeneracy-lifting mechanism that still needs to be confirmed by calculations.

A change in the YSR excitation spectra of V atoms upon hydrogenated has been observed, but the complex behavior of in-gap excitations has prevented us from finding a full explanation of the effect. We anticipate a relation between the signatures found in vibrational spectroscopy and the in-gap excitations.

Conclusions and Outlook

In this work, we have studied the physics of YSR states in systems that differ from the original picture devised by Yu, Shiba, and Rusinov. Through the analysis of the number excitations and their spatial distributions, we have been able to identify: properties of the bands in the superconducting substrate, signatures of coupling in dimers and chains, and detect variations in the adsorption configuration of vanadium hydrides.

This thesis has started with the characterization of β-Bi_2Pd samples and tips. Both of them play an essential role in our experiments, but finding the proper methodology for the fabrication of superconducting tips has allowed us to achieve energetic resolutions far beyond the temperature of our microscope. The possibility of preparing these tip in-situ using the procedure above sets β-Bi_2Pd apart from most superconductors, with reports on similar resolutions only found for Pb.

The spin-polarized bands of β-Bi_2Pd have also been one of the fundamental ingredients in this work. We have characterized them using QPI at energies far above the superconducting gap, confirming the spin polarization of all the bands in this material. Furthermore, we have characterized the sources of scattering in β-Bi_2Pd, providing an essential piece of information for our subsequent lateral manipulation experiments and, maybe, for a future understanding of the different types of superconductivity found between bulk and MBE-grown samples.

Combining our QPI experiments with the analysis of the spatial distribution of YSR states, we have identified the band to which vanadium couples in β-Bi_2Pd, and derived the properties of that band. Not only that, our results establish an equivalence between conventional QPI and scattering of Bogoliubov quasiparticles in the energy range in which they have a strongly-mixed electron and hole character. Notably, we have seen for the first time the effect of band polarization in the YSR wavefunction, corroborating through YSR states that Bogoliubov quasiparticles have a well-defined spin and that the usual spin-selection rules in QPI apply to in-gap states. This finding establishes a mechanism to study the properties of the bands of superconductors with multiple bands using a band-selective approach by choosing impurities that selectively couple to the band that wants to be studied.

Using lateral manipulation, we have been able to study the spectroscopic properties of dimers and chains of Mn atoms on the surface of β-Bi_2Pd. The results obtained in that chapter put in relief the role of magnetic coupling in the formation of YSR states in systems composed of more than one atom. We have identified two systems in which magnetic ordering may emerge from the combined interactions of several atoms, setting the foundation for future experiments of this type in β-Bi_2Pd. One of the chains constructed in this works shows excellent potential as a candidate for the study of magnetic-impurity-induced quantum phase transitions in chains of atoms. As a final example, we have shown the signature of ferromagnetic coupling in other transition metals, which can set the starting point for other experiments of this type.

In the last part of this thesis, we have used superconducting tips to identify a broken degeneracy in the vibrational modes of vanadium hydrides formed on the surface of β-Bi_2Pd during the evaporation of V atoms. We have first used the isotope effect to distinguish internal and external rotational modes of the molecule. Using the enhanced resolution provided by superconducting tips, we have identified a peak splitting in molecules with an apparent rotation and related it to the rotation vibrational modes of the molecules. From the combined analysis of topographic images and high-resolution spectroscopy, we have proposed a model that accounts for the observed effect. Using this model, we can explain the complex behavior of YSR states in these molecules. We anticipate that variations in the adsorption configuration of small molecules may result in similar in-gap excitations as the one observed for these hydrides.

In conclusion, this thesis gives a broader idea of the physics of YSR states, of their relationship with Bogoliubov quasiparticles and the scattering picture of the YSR wavefunction. The experiments on chains of atoms provide a deepers understanding of magnetic coupling in superconductors and the ingredients for the development of new states in these systems. We hope future works expand the ideas formulated in this work and that our findings help other researchers in the development of the proposed topological quantum computing platforms using magnetic impurities in superconductors.

Bibliography

(1) Meissner, W.; Ochsenfeld, R. *Die Naturwissenschaften* **1933**, *21*, 787–788.

(2) London, F.; London, H. *Proceedings of the Royal Society of London. Series A - Mathematical and Physical Sciences* **1935**, *149*, 71–88.

(3) Bardeen, J.; Cooper, L. N.; Schrieffer, J. R. *Physical Review* **1957**, *108*, 1175–1204.

(4) Yu, Luh *Acta Physica Sinica* **1965**, *21*, 75–91.

(5) Soda, T.; Matsuura, T.; Nagaoka, Y. *Progress of Theoretical Physics* **1967**, *38*, 551–567.

(6) Shiba, H. *Progress of Theoretical Physics* **1968**, *40*, 435–451.

(7) Rusinov, A. I. *Soviet PHYSICS JETP* **1969**, *9*, 85–87.

(8) Yazdani, A. *Science* **1997**, *275*, 1767–1770.

(9) Ji, S.-H.; Zhang, T.; Fu, Y.-S.; Chen, X.; Ma, X.-C.; Li, J.; Duan, W.-H.; Jia, J.-F.; Xue, Q.-K. *Physical Review Letters* **2008**, *100*, DOI: 10/cswdt5.

(10) Freedman, M. H.; Kitaev, A.; Larsen, M. J.; Wang, Z. *arXiv:quant-ph/0101025* **2002**.

(11) Kitaev, A. Y. *Physics-Uspekhi* **2001**, *44*, 131–136.

(12) Pientka, F.; Peng, Y.; Glazman, L.; Oppen, F. v. *Physica Scripta* **2015**, *T164*, 014008.

(13) Nayak, C.; Simon, S. H.; Stern, A.; Freedman, M.; Das Sarma, S. *Reviews of Modern Physics* **2008**, *80*, 1083–1159.

(14) Ruby, M.; Peng, Y.; von Oppen, F.; Heinrich, B. W.; Franke, K. J. *Physical Review Letters* **2016**, *117*, DOI: 10/gf5cs8.

(15) Choi, D.-J.; Rubio-Verdú, C.; de Bruijckere, J.; Ugeda, M. M.; Lorente, N.; Pascual, J. I. *Nature Communications* **2017**, *8*, DOI: 10/f97mtn.

(16) Choi, D.-J.; Fernández, C. G.; Herrera, E.; Rubio-Verdú, C.; Ugeda, M. M.; Guillamón, I.; Suderow, H.; Pascual, J. I.; Lorente, N. *Physical Review Letters* **2018**, *120*, DOI: 10/gdb9x8.

(17) Ruby, M.; Heinrich, B. W.; Peng, Y.; von Oppen, F.; Franke, K. J. *Physical Review Letters* **2018**, *120*, DOI: 10/gdb9xr.

(18) Nadj-Perge, S.; Drozdov, I. K.; Li, J.; Chen, H.; Jeon, S.; Seo, J.; MacDonald, A. H.; Bernevig, B. A.; Yazdani, A. *Science* **2014**, *346*, 602–607.

(19) Kim, H.; Palacio-Morales, A.; Posske, T.; Rózsa, L.; Palotás, K.; Szunyogh, L.; Thorwart, M.; Wiesendanger, R. *Science Advances* **2018**, *4*, eaar5251.

(20) *Superconductivity: in two volumes. 1: ...* Parks, R. D., Ed., OCLC: 833613165; Dekker: New York, 1969, 664 pp.

(21) Gennes, P.-G. d., *Superconductivity of metals and alloys*; Advanced book classics; Advanced Book Program, Perseus Books: Reading, Mass, 1999; 274 pp.

(22) Kittel, C.; Fong, C. Y., *Quantum theory of solids*, 2nd rev. print; Wiley: New York, 1987; 425 pp.

(23) Timm, C. Theory of Superconductivity, Lecture Notes, Lecture Notes, Technische Universität Dresden, 2011.

(24) Lancaster, T.; Blundell, S., *Quantum field theory for the gifted amateur*, First Edition, OCLC: ocn859651399; Oxford University Press: Oxford, 2014; 485 pp.

(25) Zagoskin, A., *Quantum theory of many-body systems*; Springer: New York, 2014.

(26) Arovas, D.; Wu, C. Lecture Notes on Superconductivity, Lecture notes, Lecture notes, University of California, San Diego, 2019.

(27) Cooper, L. N. *Physical Review* **1956**, *104*, 1189–1190.

(28) Fröhlich, H. *Physical Review* **1950**, *79*, 845–856.

(29) Bogoljubov, N. N. *Il Nuovo Cimento* **1958**, *7*, 794–805.

(30) Valatin, J. G.; Butler, D. *Il Nuovo Cimento* **1958**, *10*, 37–54.

(31) Andreev, A. V. *JETP* **1964**, *19*, 1228.

(32) Suhl, H.; Matthias, B. T.; Walker, L. R. *Physical Review Letters* **1959**, *3*, 552–554.

(33) Daghero, D.; Gonnelli, R. S. *Superconductor Science and Technology* **2010**, *23*, 043001.

(34) Komendová, L.; Balatsky, A. V.; Black-Schaffer, A. M. *Physical Review B* **2015**, *92*, DOI: 10/f3m9mb.

(35) Matthias, B.; Wood, E.; Corenzwit, E.; Bala, V. *Journal of Physics and Chemistry of Solids* **1956**, *1*, 188–190.

(36) Lynton, E.; Serin, B.; Zucker, M. *Journal of Physics and Chemistry of Solids* **1957**, *3*, 165–174.

(37) Anderson, P. *Journal of Physics and Chemistry of Solids* **1959**, *11*, 26–30.

(38) Flatté, M. E.; Reynolds, D. E. *Physical Review B* **2000**, *61*, 14810–14814.

(39) Kaladzhyan, V.; Bena, C.; Simon, P. *Physical Review B* **2016**, *93*, DOI: 10/ggd82v.

(40) Kaladzhyan, V.; Simon, P.; Bena, C. *Physical Review B* **2016**, *94*, DOI: 10/gf64mw.

(41) Hoffman, J. E. A Search for Alternative Electronic Order in the High Temperature Superconductor Bi2Sr2CaCu2O8+δ by Scanning Tunneling Microscopy, Ph.D. Thesis, University of California, Berkeley, 2003, 171 pp.

(42) Wiesendanger, R., *Scanning probe microscopy and spectroscopy: methods and applications*; Cambridge University Press: Cambridge [England] ; New York, 1994; 637 pp.

(43) Jaklevic, R. C.; Lambe, J. *Physical Review Letters* **1966**, *17*, 1139–1140.

(44) Stipe, B. C. *Science* **1998**, *280*, 1732–1735.

(45) Heinrich, A. J. *Science* **2004**, *306*, 466–469.

(46) Eigler, D. M.; Schweizer, E. K. *Nature* **1990**, *344*, 524–526.

(47) Okamoto, H. *Journal of Phase Equilibria* **1994**, *15*, 191–194.

(48) Imai, Y.; Nabeshima, F.; Yoshinaka, T.; Miyatani, K.; Kondo, R.; Komiya, S.; Tsukada, I.; Maeda, A. *Journal of the Physical Society of Japan* **2012**, *81*, 113708.

(49) Zhurvalev, N. N. *JETP* **1957**, *5*, 1305–1312.

(50) Herrera, E.; Guillamón, I.; Galvis, J. A.; Correa, A.; Fente, A.; Luccas, R. F.; Mompean, F. J.; García-Hernández, M.; Vieira, S.; Brison, J. P.; Suderow, H. *Physical Review B* **2015**, *92*, DOI: 10/gf4zhx.

(51) Kačmarčík, J.; Pribulová, Z.; Samuely, T.; Szabó, P.; Cambel, V.; Šoltýs, J.; Herrera, E.; Suderow, H.; Correa-Orellana, A.; Prabhakaran, D.; Samuely, P. *Physical Review B* **2016**, *93*, DOI: 10/gf4zpf.

(52) Biswas, P. K.; Mazzone, D. G.; Sibille, R.; Pomjakushina, E.; Conder, K.; Luetkens, H.; Baines, C.; Gavilano, J. L.; Kenzelmann, M.; Amato, A.; Morenzoni, E. *Physical Review B* **2016**, *93*, DOI: 10/gf4zpj.

(53) Che, L.; Le, T.; Xu, C. Q.; Xing, X. Z.; Shi, Z.; Xu, X.; Lu, X. *Physical Review B* **2016**, *94*, DOI: 10/gf4zph.

(54) Zheng, J.-J.; Margine, E. R. *Physical Review B* **2017**, *95*, DOI: 10/gf4zpk.

(55) Matsuzaki, H.; Nagai, K.; Kase, N.; Nakano, T.; Takeda, N. *Journal of Physics: Conference Series* **2017**, *871*, 012004.

(56) Sakano, M.; Okawa, K.; Kanou, M.; Sanjo, H.; Okuda, T.; Sasagawa, T.; Ishizaka, K. *Nature Communications* **2015**, *6*, DOI: 10/gf4zhw.

(57) Gor'kov, L. P.; Rashba, E. I. *Physical Review Letters* **2001**, *87*, DOI: 10/d27rmk.

(58) Iwaya, K.; Kohsaka, Y.; Okawa, K.; Machida, T.; Bahramy, M. S.; Hanaguri, T.; Sasagawa, T. *Nature Communications* **2017**, *8*, DOI: 10/gf4zpg.

(59) Xu, T.; Wang, B. T.; Wang, M.; Jiang, Q.; Shen, X. P.; Gao, B.; Ye, M.; Qiao, S. *Physical Review B* **2019**, *100*, DOI: 10/ggd6c6.

(60) Lv, Y.-F.; Wang, W.-L.; Zhang, Y.-M.; Ding, H.; Li, W.; Wang, L.; He, K.; Song, C.-L.; Ma, X.-C.; Xue, Q.-K. *Science Bulletin* **2017**, *62*, 852–856.

(61) Li, Y.; Xu, X.; Lee, M.-H.; Chu, M.-W.; Chien, C. L. *Science* **2019**, *366*, 238–241.

(62) Kolapo, A.; Li, T.; Hosur, P.; Miller, J. H. *Scientific Reports* **2019**, *9*, DOI: 10/ggd6c5.

(63) Guan, J.-Y.; Kong, L.-Y.; Zhou, L.-Q.; Zhong, Y.-G.; Li, H.; Liu, H.-J.; Tang, C.-Y.; Yan, D.-Y.; Yang, F.-Z.; Huang, Y.-B.; Shi, Y.-G.; Qian, T.; Weng, H.-M.; Sun, Y.-J.; Ding, H. *arXiv:1904.11638 [cond-mat]* **2019**.

(64) Llorens, J. B. et al. *arXiv:1904.10999 [cond-mat]* **2019**.

(65) Shein, I. R.; Ivanovskii, A. L. *Journal of Superconductivity and Novel Magnetism* **2013**, *26*, 1–4.

(66) Poza, M.; Bascones, E.; Rodrigo, J. G.; Agraït, N.; Vieira, S.; Guinea, F. *Physical Review B* **1998**, *58*, 11173–11176.

(67) Pan, S. H.; Hudson, E. W.; Davis, J. C. *Applied Physics Letters* **1998**, *73*, 2992–2994.

(68) Uehara, Y.; Fujita, T.; Iwami, M.; Ushioda, S. *Review of Scientific Instruments* **2001**, *72*, 2097–2099.

(69) Noat, Y.; Cren, T.; Debontridder, F.; Roditchev, D.; Sacks, W.; Toulemonde, P.; San Miguel, A. *Physical Review B* **2010**, *82*, DOI: 10/d4gdgk.

(70) Gusman, G. *Journal of Physics and Chemistry of Solids* **1967**, *28*, 2327–2333.

(71) Ugeda, M. M.; Fernández-Torre, D.; Brihuega, I.; Pou, P.; Martínez-Galera, A. J.; Pérez, R.; Gómez-Rodríguez, J. M. *Physical Review Letters* **2011**, *107*, DOI: 10/fvz6bf.

(72) Friedel, J. *Il Nuovo Cimento* **1958**, *7*, 287–311.

(73) Simon, L.; Bena, C.; Vonau, F.; Cranney, M.; Aubel, D. *Journal of Physics D: Applied Physics* **2011**, *44*, 464010.

(74) Nozières, P.; Pines, D., *The theory of quantum liquids*; Advanced book classics; Perseus Books: Cambridge, Mass, 1999; 180 pp.

(75) Lindhard, J. *Mat. Fys. Medd. K. Dan. Vidensk. Selsk.* **1954**, *28*.

(76) Crommie, M. F.; Lutz, C. P.; Eigler, D. M. *Nature* **1993**, *363*, 524–527.

(77) Hasegawa, Y.; Avouris, P. *Physical Review Letters* **1993**, *71*, 1071–1074.

(78) Sprunger, P. T. *Science* **1997**, *275*, 1764–1767.

(79) Weismann, A.; Wenderoth, M.; Lounis, S.; Zahn, P.; Quaas, N.; Ulbrich, R. G.; Dederichs, P. H.; Blugel, S. *Science* **2009**, *323*, 1190–1193.

(80) Pascual, J. I.; Bihlmayer, G.; Koroteev, Y. M.; Rust, H.-P.; Ceballos, G.; Hansmann, M.; Horn, K.; Chulkov, E. V.; Blügel, S.; Echenique, P. M.; Hofmann, P. *Physical Review Letters* **2004**, *93*, DOI: 10/fn8dxm.

(81) Brihuega, I.; Mallet, P.; Bena, C.; Bose, S.; Michaelis, C.; Vitali, L.; Varchon, F.; Magaud, L.; Kern, K.; Veuillen, J. Y. *Physical Review Letters* **2008**, *101*, DOI: 10/dtgftv.

(82) Jean, Y., *Molecular orbitals of transition metal complexes*, OCLC: ocm60319207; Oxford University Press: Oxford ; New York, 2005; 275 pp.

(83) Ménard, G. C.; Guissart, S.; Brun, C.; Pons, S.; Stolyarov, V. S.; Debontridder, F.; Leclerc, M. V.; Janod, E.; Cario, L.; Roditchev, D.; Simon, P.; Cren, T. *Nature Physics* **2015**, *11*, 1013–1016.

(84) Banerjee, S.; Patil, N.; Ghosh, K.; Saha, S.; Menon, G.; Ramakrishnan, S.; Grover, A.; Mishra, P.; Rao, T.; Ravikumar, G.; Sahni, V.; Tomy, C.; Balakrishnan, G.; Paul, D.; Bhattacharya, S. *Physica B: Condensed Matter* **1997**, *237-238*, 315–317.

(85) Ruby, M.; Pientka, F.; Peng, Y.; von Oppen, F.; Heinrich, B. W.; Franke, K. J. *Physical Review Letters* **2015**, *115*, DOI: 10/gf64ws.

(86) Flatté, M. E.; Reynolds, D. E. *Physical Review B* **2000**, *61*, 14810–14814.

(87) Morr, D. K.; Stavropoulos, N. A. *Physical Review B* **2003**, *67*, DOI: 10/ch2vpf.

(88) Yao, N. Y.; Glazman, L. I.; Demler, E. A.; Lukin, M. D.; Sau, J. D. *Physical Review Letters* **2014**, *113*, DOI: 10/ggbm2s.

(89) Johnson, R. C.; Rettew, R. R. *Journal of Chemical Education* **1965**, *42*, 145.

(90) Golež, D.; Bonča, J.; Žitko, R. *Physical Review B* **2012**, *86*, DOI: 10/ggd6dd.

(91) žitko, R.; Bodensiek, O.; Pruschke, T. *Physical Review B* **2011**, *83*, DOI: 10/dg892h.

(92) Bartels, L.; Meyer, G.; Rieder, K.-H. *Physical Review Letters* **1997**, *79*, 697–700.

(93) Ternes, M.; Heinrich, A. J.; Schneider, W.-D. *Journal of Physics: Condensed Matter* **2009**, *21*, 053001.

(94) Nesbet, R. K. *Physical Review* **1964**, *135*, A460–A465.

(95) Haslett, T.; Moskovits, M.; Weitzman, A. *Journal of Molecular Spectroscopy* **1989**, *135*, 259–269.

(96) Hirjibehedin, C. F. *Science* **2006**, *312*, 1021–1024.

(97) Choi, D.-J.; Robles, R.; Gauyacq, J.-P.; Rubio-Verdú, C.; Lorente, N.; Ignacio Pascual, J. *Journal of Physics: Condensed Matter* **2016**, *28*, 23LT01.

(98) Shiba, H. *Progress of Theoretical Physics* **1973**, *50*, 50–73.

(99) Balatsky, A. V.; Vekhter, I.; Zhu, J.-X. *Reviews of Modern Physics* **2006**, *78*, 373–433.

(100) Heimes, A.; Kotetes, P.; Schön, G. *Physical Review B* **2014**, *90*, DOI: 10/ggff7s.

(101) Khajetoorians, A. A.; Wiebe, J.; Chilian, B.; Lounis, S.; Blügel, S.; Wiesendanger, R. *Nature Physics* **2012**, *8*, 497–503.

(102) Cornils, L.; Kamlapure, A.; Zhou, L.; Pradhan, S.; Khajetoorians, A. A.; Fransson, J.; Wiebe, J.; Wiesendanger, R. *Physical Review Letters* **2017**, *119*, DOI: 10/gcpc5s.

(103) Akkaravarawong, K.; Väyrynen, J. I.; Sau, J. D.; Demler, E. A.; Glazman, L. I.; Yao, N. Y. *Physical Review Research* **2019**, *1*, DOI: 10/ggff2q.

(104) Roth, L. M.; Zeiger, H. J.; Kaplan, T. A. *Physical Review* **1966**, *149*, 519–525.

(105) Aristov, D. N.; Maleyev, S. V. *Physical Review B* **1997**, *56*, 8841–8848.

(106) Zhou, L.; Wiebe, J.; Lounis, S.; Vedmedenko, E.; Meier, F.; Blügel, S.; Dederichs, P. H.; Wiesendanger, R. *Nature Physics* **2010**, *6*, 187–191.

(107) Akbari, A.; Thalmeier, P.; Eremin, I. *New Journal of Physics* **2013**, *15*, 033034.

(108) Fölsch, S.; Hyldgaard, P.; Koch, R.; Ploog, K. H. *Physical Review Letters* **2004**, *92*, DOI: 10/dzxw98.

(109) Khajetoorians, A. A.; Steinbrecher, M.; Ternes, M.; Bouhassoune, M.; dos Santos Dias, M.; Lounis, S.; Wiebe, J.; Wiesendanger, R. *Nature Communications* **2016**, *7*, DOI: 10/f8cfjv.

(110) Bouaziz, J.; Dias, M. d. S.; Ziane, A.; Benakki, M.; Blügel, S.; Lounis, S. *New Journal of Physics* **2017**, *19*, 023010.

(111) Steinbrecher, M.; Rausch, R.; That, K. T.; Hermenau, J.; Khajetoorians, A. A.; Potthoff, M.; Wiesendanger, R.; Wiebe, J. *Nature Communications* **2018**, *9*, DOI: 10/gdvjx9.

(112) Roshen, W. A.; Ruvalds, J. *Physical Review B* **1983**, *28*, 1329–1331.

(113) Schecter, M.; Flensberg, K.; Christensen, M. H.; Andersen, B. M.; Paaske, J. *Physical Review B* **2016**, *93*, DOI: 10/ggfh97.

(114) Hirjibehedin, C. F.; Lin, C.-Y.; Otte, A. F.; Ternes, M.; Lutz, C. P.; Jones, B. A.; Heinrich, A. J. *Science* **2007**, *317*, 1199–1203.

(115) Khajetoorians, A. A.; Valentyuk, M.; Steinbrecher, M.; Schlenk, T.; Shick, A.; Kolorenc, J.; Lichtenstein, A. I.; Wehling, T. O.; Wiesendanger, R.; Wiebe, J. *Nature Nanotechnology* **2015**, *10*, 958–964.

(116) Gambardella, P. *Science* **2003**, *300*, 1130–1133.

(117) Pivetta, M.; Ternes, M.; Patthey, F.; Schneider, W.-D. *Physical Review Letters* **2007**, *99*, DOI: 10/b5chrc.

(118) Donati, F.; Dubout, Q.; Autès, G.; Patthey, F.; Calleja, F.; Gambardella, P.; Yazyev, O. V.; Brune, H. *Physical Review Letters* **2013**, *111*, DOI: 10/gf5tws.

(119) Serrate, D.; Moro-Lagares, M.; Piantek, M.; Pascual, J. I.; Ibarra, M. R. *The Journal of Physical Chemistry C* **2014**, *118*, 5827–5832.

(120) Lauhon, L. J.; Ho, W. *Physical Review Letters* **2000**, *84*, 1527–1530.

(121) Zhao, A. *Science* **2005**, *309*, 1542–1544.

(122) Heinrich, B. W.; Braun, L.; Pascual, J. I.; Franke, K. J. *Nature Physics* **2013**, *9*, 765–768.

(123) Tsukahara, N.; Noto, K.-i.; Ohara, M.; Shiraki, S.; Takagi, N.; Takata, Y.; Miyawaki, J.; Taguchi, M.; Chainani, A.; Shin, S.; Kawai, M. *Physical Review Letters* **2009**, *102*, DOI: 10/dgjv6q.

(124) Ormaza, M.; Bachellier, N.; Faraggi, M. N.; Verlhac, B.; Abufager, P.; Ohresser, P.; Joly, L.; Romeo, M.; Scheurer, F.; Bocquet, M.-L.; Lorente, N.; Limot, L. *Nano Letters* **2017**, *17*, 1877–1882.

(125) Rubio-Verdú, C.; Sarasola, A.; Choi, D.-J.; Majzik, Z.; Ebeling, R.; Calvo, M. R.; Ugeda, M. M.; Garcia-Lekue, A.; Sánchez-Portal, D.; Pascual, J. I. *Communications Physics* **2018**, *1*, DOI: 10/ggd6ps.

(126) Hollas, J. M., *Modern spectroscopy*, 4th ed; J. Wiley: Chichester ; Hoboken, NJ, 2004; 452 pp.

Resumen Extendido

En esta Tesis se estudia la interacción de impurezas magnéticas con materiales superconductores a escala atómica por medio de la Microscopía de Efecto Túnel. Para evaluar los diferentes factores que influyen en esta interacción, se evaporan átomos de diferentes metales de transición en la superficie de cristales de β-Bi_2Pd, una aleación de Bismuto y Paladio que presenta superconductividad por debajo de 5.4 K. Las muestras estudiadas se preparan en condiciones de ultra alto vacío y se estudian a 1.3 Kelvin.

El carácter antagónico de la superconductividad y el magnetismo da lugar a fenómenos únicos. En el límite atómico, la combinación de átomos magnéticos con superconductores da lugar a nuevos estados que no existen en el resto de materiales: los estados de Yu-Shiba-Rusinov (YSR). Estos estados nacen del delicado equilibrio entre las correlaciones superconductoras y los minúsculos campos magnéticos producidos por átomos de metales de transición. Sus propiedades les imprimen un carácter ligeramente diferente al de los electrones, lo que en los últimos años ha suscitado interés en utilizarlos como componentes para desarrollar plataformas en las que realizar operaciones de computación cuántica.

Las propiedades fundamentales de los estados YSR se describieron teóricamente por primera vez en los años 60, pero la tecnología no permitió observarlos experimentalmente hasta la invención del STM. Desde entonces, el nivel de comprensión sobre los mecanismos que gobiernan la formación de éstos estos ha aumentado de manera exponencial. A través de los años se ha descubierto que muchas de las propiedades de los átomos y del material supercondcutor se manifiestan en la función de onda de los estados YSR. La motivación principal de esta Tesis es utilizar esta transferencia de propiedades para entender mejor los superconductores y los mecanismos de acople entre átomos magnéticos. Para ello, se utilizan técnicas de manipulación atómica y espectroscopía de muy alta resolución con puntas de STM superconductoras.

En la primera parte de esta tesis, se hace un recorrido histórico de los descubrimientos relacionados con la interación de los campos magnéticos con superconductores, pasando luego a la descripción de los primeros modelos de interacción de impurezas magnéticas con superconductores y a las predicciones recientes que relacion los estados de YSR con la computación cuántica.

Después de la introducción histórica, la teoría BCS es derivada de manera informal como motivación para la introducción de las cuasipartículas de Bogoliubov. Estas cuasipartículas describen las excitaciones de los superconductores y son la base fundamental sobre la que se sustenta la teoría de los estados YSR. Una vez descritas las propiedades fundamentales de las cuasipartículas de Bogoliubov, se sigue con la formulación básica de los estados YSR y su función para comprender qué es lo que los hace distintos de otros estados de la materia. De las propiedades descritas en esta sección surgen todos los efectos observados a lo largo de este trabajo.

En la siguiente parte, se describe el principio de funcionamiento del STM, con la descripción de la espectroscopía con puntas superconductoras. Esta técnica permite mejorar la resolución energética del STM y es usada a lo largo de este trabajo en la mayoría de las medidas experimentales. En este capítulo se describen las razones por las que se logra esa mejora. Seguidamente se decriben los principios básicos de la manipulación atómica, así como el funcionamiento del equipo utilizado en esta tesis.

En el cuarto capítulo se explican los métodos de preparación de muestras de β-Bi_2Pd. La elección de este material para este trabajo viene motivada por la compleja estructura de bandas de este material, caracterizada por varias bandas polarizadas en espín. En este capítulo se describen estas bandas en profundidad y se revisan los últimos descubrimientos relacionados con el β-Bi_2Pd. Además, se explica el procedimiento utilizado para fabricar puntas superconductoras de β-Bi_2Pd, enseñando ejemplos de la mejora en resolución. En la última parte se estudia el gap superconductor del β-Bi_2Pd usando puntas de este mismo material, y se compara con medidas recientes en films de este mismo material, mostrando las diferencias espectroscópicas entre estos últimos y las muestras usadas en esta Tesis.

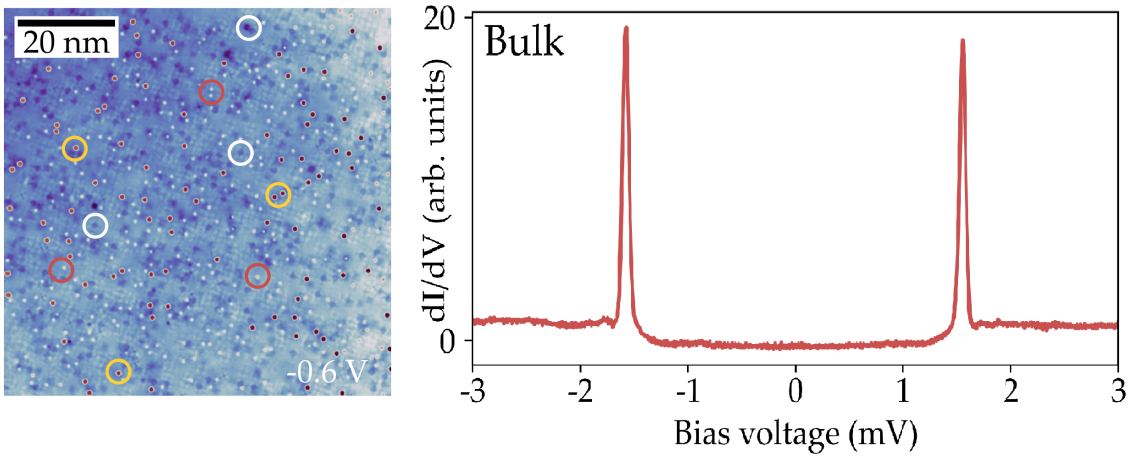

Figure 1: Características de los cristales de β-Bi_2Pd. **a)** Superficie de β-Bi_2Pd medida utilizando el STM. Diferentes tipos de defectos aparecen en la superficie. **b)**Medida espectroscópica del gap superconductor del β-Bi_2Pd utilizando puntas del mismo material.

En el quinto capítulo se caracterizan las propiedades de las bandas polarizadas en espín del β-Bi_2Pd usando la interferencia de cuasipartículas. En primer lugar, se explica la relación entre la estructura de bandas y la interferencia de cuasipartículas, describiendo con un modelo simple cómo la forma de las bandas y su dimensionalidad definen las propiedades de los patrones de interferencia de cuasipartículas alrededor de impurezas. Seguidamente, se identifican las impurezas no magnéticas intrínsecas de las muestras de β-Bi_2Pd, causantes de la interferencia de cuasipartículas en este material. Los patrones de interferencia de cuasipartículas medidos experimentalmente son analizados utilizando transformadas de Fourier para identificar los procesos de scattering entre las bandas del β-Bi_2Pd. Comparando medidas de la estructura de bandas con nuestros resultados de procesos de scattering, econtramos que la polarización de espín helical de las bandas impide los procesos de scattering dentro de la propia banda. Sin embargo, los procesos entre distintas bandas que conservan el espín sí aparecen en nuestras medidas, demostrando la polarización de las bandas en nuestros cristales de β-Bi_2Pd.

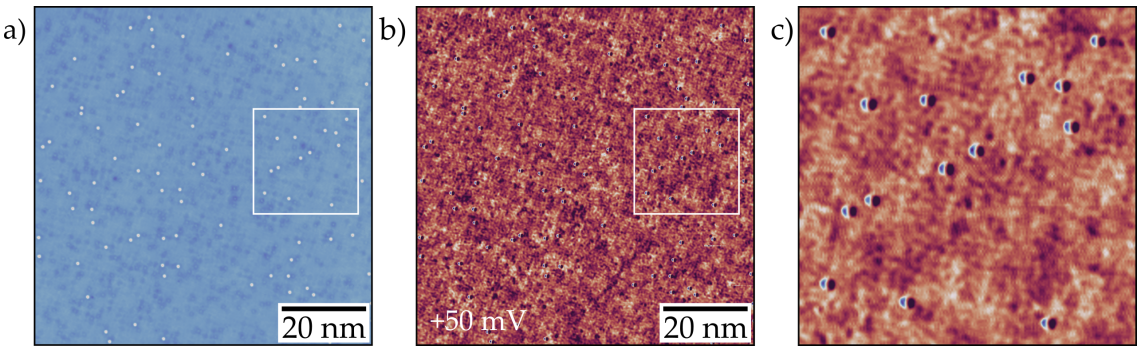

Figure 2: Interferencia de cuasipartículas en β-Bi_2Pd. a) Superficie de β-Bi_2Pd medida utilizando el STM. **b)** Mapa de las variacón de la densidad de estados en la misma zona. **c)** Ampliacion de la imágen b), mostrando los patrones de interferencia de cuasipartículas como modulaciones alrededor de las impurezas.

En el siguiente capítulo, se estudia la distribución espacial de la función de onda de los estados YSR. Para ello, se evaporan átomos de vanadio sobre la superficie de β-Bi_2Pd. Este metal de transición induce tres estados YSR que se extienden varios nanómetros alrededor de la impureza, un fenómeno poco común. Examinando la forma de esta función de onda, descubrimos que el vanadio se acopla solamente con una de las bandas del β-Bi_2Pd. Esto se consigue comparando las medidas de interferencia de cuasipartículas del capítulo anterior con medidas de alta resolución de los estados YSR. Los procesos de scattering de la banda aparecen en la función de onda del estado YSR, lo que nos permite establecer una relación entre la interferencia de cuasipartículas y los estados YSR. Además, el estudio de la función de onda sólo nos muestra las propiedades de la banda a la que se acopla el V, lo que nos permite proponer este tipo de medida como un mecanismo para estudiar de manera aislada las bandas de materiales superconductores con múltiples bandas.

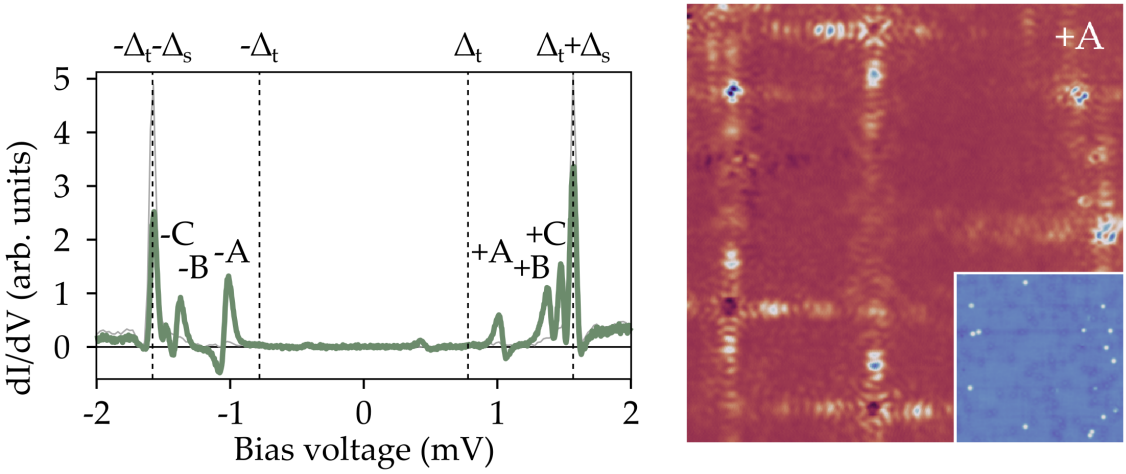

Figure 3: Estados de YSR inducidos por el vanadio en la superficie de β-Bi_2Pd. a) Señal espectrscópica de los estados YSR. Cada uno de los picos ±A, ±B y ±C representan la presencia de un estado YSR. **b)** Función de onda de los estados YSR. Midiendo la distribución de la densidad de estados a la energía de los picos asociados a los YSR, podemos medir la función de onda del estado YSR. En la imagen principal, los estados YSR aparecen como cruces alrededor de las impurezas. En la imagen pequeña se muestra la topografía de la zona. Los puntos blancos son átomos de vanadio.

El séptimo capítulo de esta Tesis se centra en las interacciones magnéticas entre átomos de manganeso y en cómo estas interacciones modifican la función de onda de los estados YSR. En primer lugar, se evaporan átomos de Mn en la superficie de β-Bi_2Pd. Utilizando puntas superconductoras, se caracterizan los estados YSR en estos átomos, encontrando una gran variabilidad de valores que es atribuida a la presencia de varios orbitales paramagnéticos degenerados. Una vez se han caracterizado los átomos aislados, se utiliza la punta del STM para desplazar los átomos y formar dímeros en diferentes configuraciones. Analizando los estados YSR en estos dímeros, se identifican las señales características de acople ferromagnético y antiferromagnético entre los átomos que los constituyen. Comparando los diferentes casos, se establece una relación entre la distancia que separa los átomos en el dímero y el tipo de acople que presenta. La segunda parte de este capítulo se centra en estructuras más complejas, construyendo dos cadenas de átomos en distintas configuraciones para estudiar la evolución de los estados YSR en estos sistemas. Se observan dos comportamientos diferentes dependiendo de la distancia entre átomos en la cadena. En una de ellas los estados YSR indican la formación de orden antiferromagnético dentro de la cadena y un comportamiento ligeramente diferente en los extremos. En el segundo caso se estudia la evolución de los estados YSR cuando la cadena está formada por 5, 8, 11 y 13 átomos. Los estados YSR de esta cadena evolucionan mostrando una modulación de sus energías que se hace más fuerte conforme aumenta la longitud de la cadena, además de efectos diferentes en los bordes.

El octavo y último capítulo experimental de este trabajo estudia las excitaciones vibracionales de hidruros de vanadio utilizando puntas superconductoras. Estos hidruros se forman en la superficie de β-Bi_2Pd durante la evaporación de

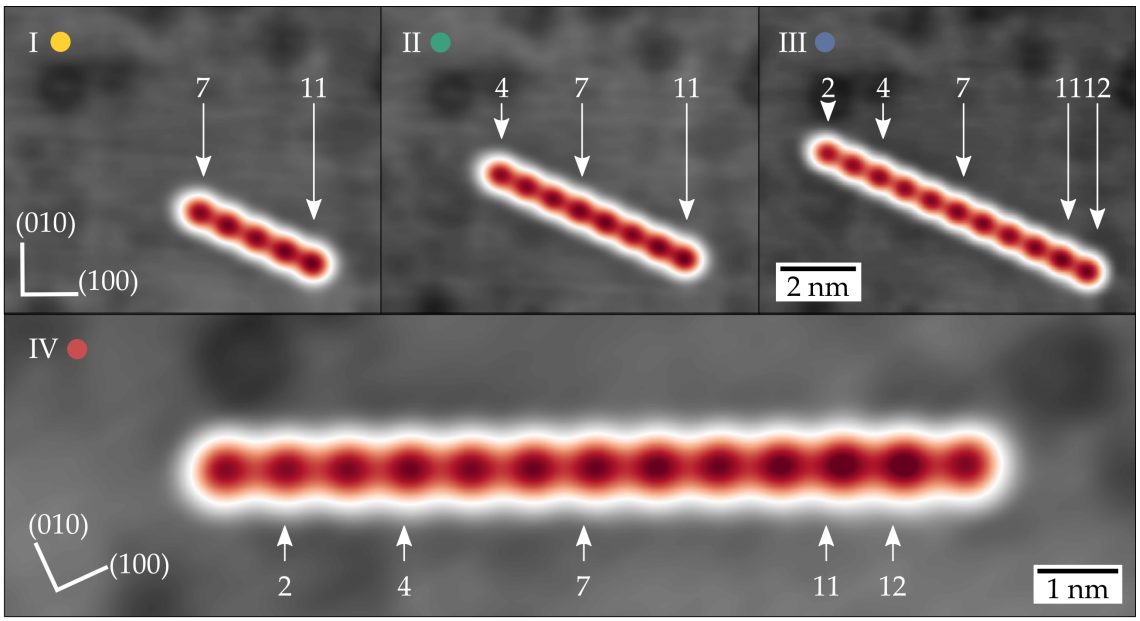

Figure 4: Construcción de una cadena de átomos de Mn en β-Bi_2Pd. De izquierda a derecha y de arriba abajo, se muestran las distintas etapas de la construcción de una cadena de átomos. Los átomos se van añadiendo a los extremos utilizando la punta del STM. Los números de los átomos representan su posición en la cadena final.

vanadio. Los átomos actúan como catalizadores de la discociación de hidrógeno molecular presente en la cámara de medida, quedando el hidrógeno atómico adherido a los átomos de V. Utilizando el efecto isotópico, comparamos las vibraciones de los hidruros con las de la especie deuterada para distinguir los modos internos y externos de vibración de la molécula. La alta resolución obtenida con puntas superconductoras nos permite detectar la rotura de una degeneración en moléculas que parecen rotadas, lo que nos ayuda a identificar los distintos modos rotacionales. En la última sección se analiza la espectroscopía de los estados YSR en estas moléculas, encontrando un comportamiento muy diferente al de los átomos de V no hidrogenados.

Como idea principal de la Tesis, se extrae la conclusión de que los estados YSR son una buena herramienta para caracterizar las propiedades de los superconductores y de las impurezas magnéticas. Con los resultados obtenidos en esta Tesis se espera avanzar en el conocimiento de los estados YSR, y en particular, los resultados obtenidos en los capítulos seis y siete establecen una metodología con la que estudiar superconductores e impurezas magnéticas, respectivamente. De los experimentos realizados en este trabajo surgen propuestas para futuros trabajos en los que se utilizará el concocimiento generado durante esta Tesis para avanzar hacia el modelo de computación cuántica predicho para los estado YSR.